Thermodynamics and transport of defects in Sc-doped $CaSnO_3$ and $CaZrO_3$

Andreas Løken

Master Thesis in Chemistry

UNIVERSITY OF OSLO
DEPARTMENT OF CHEMISTRY

May 2011

Preface

This thesis fulfils the requirements for the Master of Science degree in Chemistry at the Department of Chemistry, University of Oslo. The experimental work was conducted at the Centre for Materials Science and Nanotechnology (SMN) in the time period from August 2009 to May 2011.

I would first of all like to thank my supervisors, associate professor Reidar Haugsrud and professor Truls E. Norby, who have been inspirational, helpful and supportive throughout the entire period.

While I am thankful to the entire research group for solid-state electrochemistry, I am especially grateful to Tor Svendsen Bjørheim for all his invaluable help during the last few months. Furthermore, I would like to thank Christian Kjølseth for laying the foundation for TG-DSC as a technique and interesting thermodynamic discussions. I would also like to acknowledge Harald Fjeld for his help in proofreading.

For providing a pleasant office environment, I would like to thank my fellow “football freak”, Kingsley Odinaka Iwu.

Lastly, I want to thank Daghild for her love, patience and support.

University of Oslo, May 2011

Andreas Løken

Abstract

Correlations aimed at linking the hydration thermodynamics to materials parameters can be of vital importance for further development of proton conducting oxides. However, the currently proposed correlations are to a large degree troubled by scattering limiting their predictive power. As such, the present contribution has investigated Sc-doped $CaSnO_3$ and $CaZrO_3$ in an attempt to further elucidate the thermodynamic trends of hydration in perovskites.

The defect structure and conductivity of polycrystalline samples of $CaSn_{0.95}Sc_{0.05}O_{3-\delta}$ and $CaSn_{0.9}Sc_{0.1}O_{3-\delta}$ has been studied by AC impedance measurements in the temperature range 150-1100 °C. The majority defects were characterised by measuring the conductivity as a function of p_{H_2O} and p_{O_2}. These indicated that both samples are predominantly oxygen ion conducting with a protonic contribution under wet conditions at 300-400 °C for $CaSn_{0.9}Sc_{0.1}O_{3-\delta}$. Under oxidising conditions at elevated temperatures of 1000 °C and above, the conductivity is dominated by electron holes. The p_{H_2O} dependencies at temperatures of 300-500 °C for $CaSn_{0.9}Sc_{0.1}O_{3-\delta}$ were modelled based on a simplified defect structure resulting in an extracted hydration enthalpy and entropy of -41 ± 5 kJ mol^{-1} and -107 ± 7 J K^{-1} mol^{-1}, respectively.

Impedance spectroscopy was conducted in the temperature range 150-700 °C in order to study the hydration processes in the grain boundaries of Sc-doped $CaSnO_3$. It was demonstrated that the grain boundary conductivity exhibited a larger contribution from protons than the bulk at temperatures below 400 °C. These differences were suggested to be due to the presence of inherent space charge layers depleting the oxygen vacancies. The depletion of oxygen vacancies was more severe for $CaSn_{0.95}Sc_{0.05}O_{3-\delta}$ than $CaSn_{0.9}Sc_{0.1}O_{3-\delta}$, which is consistent with a smaller segregation of acceptors compensating the positively charged grain boundary core.

Simultaneous thermogravimetry (TG) and differential scanning calorimetry (DSC), TG-DSC, was applied to measure the standard molar hydration enthalpies and entropies of $CaSn_{1-x}Sc_xO_{3-\delta}$ and $CaZr_{1-x}Sc_xO_{3-\delta}$ as a function of the concentration of Sc. It was demonstrated that both the hydration enthalpy and entropy become increasingly negative with increasing Sc substitution. The thermodynamic parameters were in agreement with the values from literature and the results from conductivity measurements and TG. The values were also demonstrated to be consistent with respect to temperature (500-900 °C) and p_{H_2O} (0.1-1 atm). This suggests that TG-DSC can be used for the evaluation of hydration thermodynamics in oxides.

The obtained thermodynamic parameters of hydration from TG-DSC were compared with available literature values of other perovskites in an attempt to correlate the values to materials properties. While the hydration enthalpy was found to be in good agreement with the basicity of the oxide, the hydration entropy exhibited a dependence to the vibrational wavenumber of the OH stretching mode (ν_{OH}). As the two are interrelated properties, it suggests a correlation between the thermodynamic parameters of hydration, as was demonstrated in both materials studied.

Table of contents

1. Introduction

1.1. Motivation and background

The world has become very dependent on readily available energy ever since the first industrial revolution of the 18th century. In 2010, the Energy Information Administration (EIA) stated that from 1990 to 2007, the annual worldwide energy consumption had increased by 39 % to a value of 5.2×10^{20} J. The use of fossil fuels had accounted for 84 % of the consumption during this period. Considering the current rate of consumption, world fossil fuel reserves will run out in 150 years. However, it is forecasted that energy demand will increase annually by at least 1.4 % between 2007 and 2035, thereby making 150 years an optimistic estimation [1]. Clearly, efforts have to be made to diversify the energy mix, as fossil fuels are likely to play an important role in energy production in decades to come.

Not only are fossil fuels running out, but fossil fuel combustion is responsible for the majority of the increase in CO_2-emissions, being the most abundant anthropogenic greenhouse gas. It has also been established that such emissions have resulted in an increase in the global surface temperature of 0.6 °C over the past century. However, this increase has been more severe over the last 25 years, giving rise to a projected average temperature increase of almost 1.8 °C by 2030. CO_2 emissions are also expected to increase to 54 % above the 1990 levels by 2015, which is predicted to increase the temperature by 1.7 - 4.9 °C from 1990 to 2100 as shown in Figure 1.1 [2]. In order to stabilise the current atmospheric CO_2 concentration under 450 ppm while maintaining world economic growth, approximately 30 TW of power per annum will have to be generated by carbon clean sources by 2050 [3].

With the depletion of fossil fuels and their adverse effects on the climate, renewable energy sources are clearly the only key to a sustainable future. Consequently, a total of 66 countries have called for renewable energy targets of 20 % by 2020 in line with the EU regulations [4].

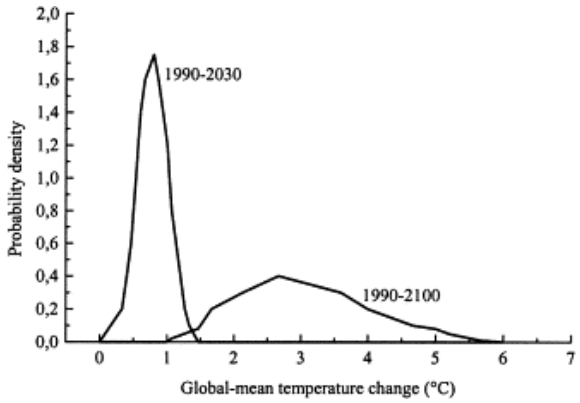

Figure 1.1: The average global surface temperature change over the period of 1990–2100 and 1990–2030 based on increasing levels of CO_2. Taken from Stambouli and Traversa [2].

A possible way to fulfill these targets is to employ fuel cells, which may convert hydrogen gas or other fuels into clean water vapour with energy efficiencies of almost 60 %. Solid oxide fuel cells (SOFCs) are preferable as they are both more rigid and sturdy while also being far more corrosion resistant compared to using aqueous electrolytes. In the traditional SOFC, oxygen is reduced at the cathode and transported through an oxygen ion conducting electrolyte e.g. yttria stabilised zirconia (YSZ). This will react with the hydrogen gas on the anode side to form water. Alternatively, a proton conducting electrolyte may be used, where the hydrogen is oxidised to form protons, which are transported across the electrolyte to form water at the cathode side (Figure 1.2). The main advantage of using a proton conducting electrolyte is that the water is formed on cathode side and thus does not dilute the fuel as is the case for the oxide ion conducting electrolyte.

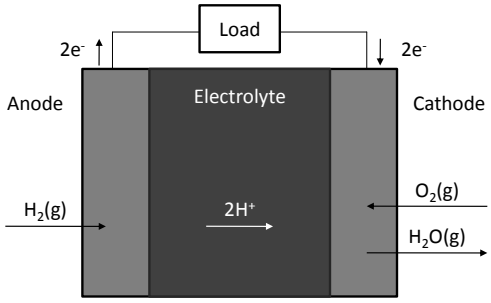

Figure 1.2: Proton conducting fuel cell using hydrogen gas as fuel.

While proton conducting fuel cells (PCFCs) exhibit some of the most promising properties of the available fuel cells due to their high conductivities and improved stability, there are still some issues in the way before they can become fully commercialised as alternatives to fossil fuels. In order to exploit the high mobility of protons, the fuel cells need to be run at

temperatures around 600-700 °C. However, as of yet, stability and materials properties still need to be improved at these high temperatures.

1.2. Proton conducting perovskites

Ever since the discovery of proton conduction in acceptor doped $SrCeO_3$ by Iwahara and his co-workers in the 1980s, ABO_3 perovskites have maintained their lead as one of the superior classes of proton conducting materials [5]. Perovskites consist of a corner-shared octahedral framework of BO_6 with the A-site cation positioned in the centre. It has often been dubbed an inorganic chameleon due to its rich diversity of chemical compositions and properties. As such, it is capable of hosting various substitutions, interstitials, vacancies and other defects without having to compensate for a loss in structure.

Perovskites are normally extrinsically doped with lower valent cations substituting a proportion of either the A- or B-site cation to introduce oxygen vacancies. These may in contact with water form protons incorporated into the structure through the hydration reaction:

$$H_2O(g) + v_O^{\bullet\bullet} + O_O^X = 2OH_O^{\bullet} \qquad \textbf{Equation 1.1}$$

The thermodynamics of this reaction lie at the heart of all proton conductors. As such, empirical correlations have been sought in attempts to tie the hydration thermodynamics to materials properties of perovskites. One of which gives an apparent relationship between the electronegativity difference between the B- and A-site cation and the hydration enthalpy in which the enthalpy becomes increasingly negative as the electronegativity difference becomes smaller [6]. However, the current correlations are all troubled with scattering reducing their predictive power. Furthermore, it questions the experimental results and the use of the established defect models which may be too simplistic.

With the recent progress of the use of simultaneous thermogravimetry and differential scanning calorimetry (TG-DSC) in acceptor doped $Ba(Ce,Zr)_{0.9}Y_{0.1}O_{3-\delta}$, the hydration enthalpy may be evaluated directly and as such may elucidate the validity of the suggested correlations [7, 8].

1.3. Protons in $CaSnO_3$ and $CaZrO_3$

Most of the techniques used to evaluate the hydration thermodynamics are indirect methods such as conductivity measurements and thermogravimetry. With the arrival of TG-DSC as a technique, further verification of other perovskites is still needed. The main goal of this thesis is to elucidate the hydration thermodynamics of two calcium based perovskites; $CaSnO_3$ and $CaZrO_3$. $CaSnO_3$ has of yet not been studied for hydration, and should empirically not incorporate protons based on the electronegativity correlation as $\Delta\chi_{B-A}$ is 0.68. Such a high electronegativity difference suggests that it should be purely oxygen ion conducting over a wide temperature range. However, recent progress has indicated that materials may exhibit different dependencies on the partial pressure of gases in the bulk and grain boundaries. For instance, acceptor doped $Er_2Ti_2O_7$ is known to be an oxide ion conductor i.e. the material exhibits no p_{H_2O} dependency. However, impedance spectroscopy results indicated that its grain boundaries were dominated by protons at lower temperatures. This was suggested to occur due to presence of inherent space charge layers in the grain boundaries depleting the oxygen vacancies [9, 10]. As such, AC impedance spectroscopy, conductivity and TG-DSC measurements will be conducted to study the incorporation of protons in the bulk and grain boundaries in acceptor doped $CaSnO_3$ to gain a further understanding of the space charge layers in grain boundaries.

Furthermore, TG-DSC will be used to elucidate the hydration enthalpy in $CaSnO_3$ and $CaZrO_3$ as a function of acceptor concentration. The latter is already a well established proton conductor and the directly evaluated values should therefore be compared to literature values. In order to verify TG-DSC as a technique, hydration enthalpies will be evaluated as a function of temperature and p_{H_2O} for acceptor doped $CaZrO_3$.

The evaluated values from conductivity measurements and TG-DSC will then be discussed in relation to the hydration thermodynamics of other perovskites available in the literature. This may help to understand the links between thermodynamics and other materials properties of perovskites.

2. Theory

This chapter covers the underlying theory behind the processes, concepts and experiments involved in the work done in this thesis. It will mainly be concerned with defect chemistry and impedance spectroscopy while also touching upon space charge layer theory. The majority of the contents is taken from parts of Defects and Transport in Crystalline Solids by Per Kofstad and Truls Norby [11], Electrical Measurements by Truls Norby [12] and Electrical properties of the grain boundaries of oxygen ion conductors: Acceptor-doped zirconia and ceria by Xin Guo and Rainer Waser [13] if not else stated.

2.1. Defect chemistry

In all crystalline materials, atoms or ions are arranged in an orderly repeating fashion extending in all three spatial dimensions. Although first believed to be perfect entities, Wagner and Schottky using statistical thermodynamics showed that all crystals above 0 K contained defects. Up to a certain defect concentration, the crystal will always be thermodynamically stable and a lot of properties are to a large extent dependent on the type and concentration of the defects in the crystal. There are several types of defects: If the imperfection is limited to a specific lattice site and its immediate vicinity, it is a zero-dimensional point defect. These point defects may among other things comprise vacancies of structural sites and foreign atoms occupying the interstitial space between the atoms (Figure 2.1).

Crystals can also contain one-dimensional defects consisting of dislocations, two-dimensional defects such as grain boundaries, stacking faults, internal interfaces and external surfaces and three-dimensional defects such as precipitations that extend in all directions. In addition to these structural defects, a crystal may contain electronic defects; electrons and holes. Only point defects, electronic defects and grain boundaries are relevant for the work done in this thesis.

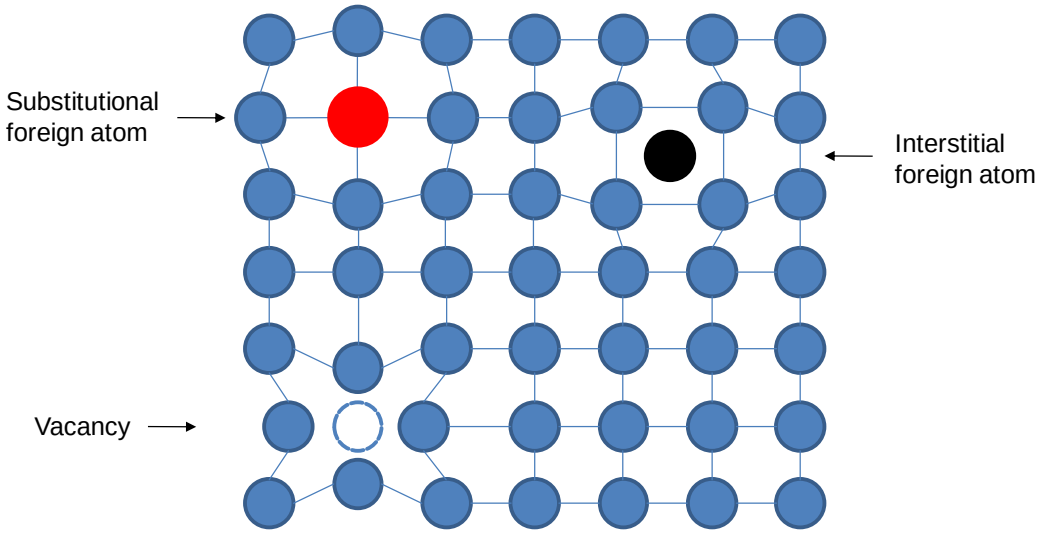

Figure 2.1: Crystals may comprise of different point defects, which are limited to single structural sites and their immediate vicinity. This crystal is chosen to be monoatomic for simplicity.

2.1.1. Kröger-Vink notation for point defects

As a lot of properties of crystals rely on point defects, it is necessary to describe the concentrations of these defects at given conditions. This requires a system of notation for point defects. For this study, the system of notation developed by F.A. Kröger and H.J. Vink [14] will be used. This notation describes point defects and structural units as A_s^c, where A is the chemical symbol for the species, s indicates the lattice site the species occupies and c is its effective charge. An empty lattice site that is normally occupied by a constituent species is a vacancy and is denoted with a v. Similarly, a species occupying the interstitial space between the lattice atoms or ions is an interstitial and its site is denoted with an i. In order to distinguish real and effective charges, a positive, negative and neutral effective charge are denoted with $^{\bullet}$, $^{/}$ and ^{X} respectively. Table 2.1 listed below shows the notation used for some chosen defects that are relevant for this thesis.

Table 2.1: Kröger-Vink notation for some chosen defects relevant for the work done in this thesis.

Defect	Notation
Electron	e'
Hole	$h^{\bullet}$
Oxygen vacancy	$v_O^{\bullet\bullet}$
Tin vacancy	$v_{Sn}^{////}$
Substitutional Sc	Sc_{Sn}'

Accompanying the notation for point defects are rules that apply for defect equilibria. These are analogous to the rules found for aqueous solutions and can be summarised as follows:

1. Conservation of mass – The defect reaction must be balanced in terms of mass. Number and type of atoms involved have to be equal on each side of the equilibrium.
2. Conservation of charge – The total effective charge has to be the same on each side of the equilibrium.
3. Conservation of the ratio of structure sites – The ratios of the number of cation and anion structure sites has to remain the same on each side of the equilibrium. This can for instance mean that in an oxide ABO_3, the ratio A:B:O has to remain 1:1:3 regardless of actual composition. Thus, if three oxygen sites were to be created in a defect reaction, an A-site and B-site must simultaneously be created, although these may be vacant or filled. This latter rule is unique to defect chemistry and thus requires special attention.

With these rules in place, any reaction involving the creation or annihilation of defects may be described.

2.1.2. Defects in $CaSn_{1-x}Sc_xO_{3-\delta}$

Oxides may often experience cation and anion vacancies in the lattice. For instance, cation metal vacancies can often occur for compounds containing tetravalent tin such as $CaSnO_3$. This is mainly due to the evaporative decomposition of SnO_2 [15, 16] and can be described by the following defect equilibria:

$$Sn_{Sn}^{X} + 2O_O^{X} = v_{Sn}^{////} + SnO(g) + \frac{1}{2}O_2(g) + 2v_O^{\bullet\bullet} \qquad \textbf{Equation 2.1}$$

or

$$Sn_{Sn}^{X} = v_{Sn}^{////} + Sn(g) + 4h^{\bullet} \qquad \textbf{Equation 2.2}$$

Thus, an understoichiometry of Sn in the perovskite $CaSnO_3$ will depend on the activity of SnO/Sn (g) but is reported to generally occur at temperatures above 1200 °C [17, 18]. However, most ceramic samples of $CaSnO_3$ are calcined or at least sintered at or above 1200 °C, meaning that tin vacancies may often be encountered.

An interaction with gaseous oxygen in the atmosphere may result in intrinsic oxygen vacancies:

$$O_O^X = v_O^{\bullet\bullet} + 2e^/ + \frac{1}{2}O_2(g) \qquad \textbf{Equation 2.3}$$

Equation 2.3 shows in accordance with Le Châtelier's principle that the concentration of both oxygen vacancies and electrons ($[v_O^{\bullet\bullet}]$ and n, respectively) is dependent on the partial pressure of oxygen, p_{O_2}. Low levels of p_{O_2} will shift the equilibrium to the product side meaning that there to a large extent will be oxygen vacancies charge-compensated by electrons.

Similarly, a hydrogen-containing atmosphere may result in protonic point defects. These protons will be located in the electron cloud of the oxide ion, such that they can be considered to be hydroxide defects situated on oxygen-sites, $OH_O^\bullet$. This proton is free to move and can also be denoted as an interstitial proton, $H_i^\bullet$ even though this is not common practice. Examples of the protonation of oxide ions are:

$$H_2(g) + 2O_O^X = 2OH_O^\bullet + 2e^/ \qquad \textbf{Equation 2.4}$$

or

$$H_2O(g) + 2O_O^X = 2OH_O^\bullet + 2e^/ + \frac{1}{2}O_2(g) \qquad \textbf{Equation 2.5}$$

From these dissolution reactions, it can be seen that the concentration of protons is both dependent on the activities of the hydrogen source (i.e. water vapour or hydrogen gas) and oxygen.

By combining Equation 2.3 and Equation 2.5, one can arrive at the hydration reaction, which is of great importance for the thermodynamic understanding of proton conductors:

$$H_2O(g) + O_O^X + v_O^{\bullet\bullet} = 2OH_O^\bullet \qquad \textbf{Equation 2.6}$$

The equilibrium for the formation of protonic defects (Equation 2.6) can be described by a dissociation of a water vapour molecule into a hydroxide ion and a proton. The hydroxide ion will fill an oxygen vacancy while the proton will form a covalent bond with a lattice oxygen, thus creating two protonic defects for each water molecule.

Most of the defects that have been described so far have arisen intrinsically in the crystal lattice. However, extrinsic aliovalent[1] dopants may be introduced to induce certain defects within the structure. For the work done in this thesis, $CaSnO_3$ was acceptor-doped with Sc_2O_3 resulting in Sc'_{Sn}, which needs to be charge-compensated by positively charged extrinsic point defects. This can for instance result in:

$$2CaO + Sc_2O_3 = 2Sc'_{Sn} + 2Ca^x_{Ca} + 5O^x_O + v^{\bullet\bullet}_O \qquad \textbf{Equation 2.7}$$

or

$$2CaO + Sc_2O_3 + \tfrac{1}{2}O_2(g) = 2Sc'_{Sn} + 2Ca^x_{Ca} + 6O^x_O + 2h^{\bullet} \qquad \textbf{Equation 2.8}$$

Realistically, both of these equilibria may take place, but one is generally more dominant than the other. Also, intrinsic effective negatively charged defects e.g. electrons may even be consumed in a similar manner to compensate for the introduced dopant. However, such an intrinsicity can only result in small concentrations of defects, and will constitute only a small percentage of the dopant concentration. Thus, the net effect from the dopant will result from the creation of point defects as described in the above equations (Equation 2.7 and Equation 2.8).

However, oxygen vacancies may be hydrated in the presence of a hydrogen source and can therefore alter the equilibria described:

$$H_2O(g) + 2CaO + Sc_2O_3 = 2Sc'_{Sn} + 2Ca^x_{Ca} + 4O^x_O + 2OH^{\bullet}_O \qquad \textbf{Equation 2.9}$$

The total electroneutrality for the samples studied is as follows:

$$2[v^{\bullet\bullet}_O] + p + [OH^{\bullet}_O] = [Acc'] + n \qquad \textbf{Equation 2.10}$$

where $[Acc']$ is the concentration of the acceptors in the sample. Thus, for Sc-doped $CaSnO_3$, this concentration is given by the concentration of the dopant and the tin vacancies that have arisen due to evaporation.

[1] Aliovalent: Different valence to the ions in the host structure.

$$[\mathrm{Acc}^{/}] = 4[\mathrm{v}_{\mathrm{Sn}}^{////}] + [\mathrm{Sc}_{\mathrm{Sn}}^{/}] \qquad \textbf{Equation 2.11}$$

2.1.3. Defects in $CaZr_{1-x}Sc_xO_{3-\delta}$

For Sc-doped $CaZrO_3$, the defect structure is much the same as in $CaSnO_3$ with obvious exceptions such as the thermodynamic parameters and unlike tetravalent tin, zirconium is not known to be volatile and should therefore not evaporate. Therefore the total concentration of acceptors in this material should be equal to concentration of the dissolved dopant i.e. $[\mathrm{Sc}_{\mathrm{Zr}}^{/}] = [\mathrm{Acc}^{/}]$. However, the defect equilibria derived for $CaSn_{1-x}Sc_xO_{3-\delta}$ are still completely valid for this material and will therefore not be repeated here.

2.1.4. Concentration of defects as a function of p_{O_2}

The concentration of point defects may depend on the partial pressure of oxygen, p_{O_2}. Using Equation 2.3 and Equation 2.6 for the formation of oxygen vacancies and protons respectively, the following equilibrium constants are derived:

$$\mathrm{K}_{\mathrm{v}_{\mathrm{O}}^{\bullet\bullet}} = \frac{[\mathrm{v}_{\mathrm{O}}^{\bullet\bullet}] n^2 {p_{\mathrm{O}_2}}^{\frac{1}{2}}}{[\mathrm{O}_{\mathrm{O}}^{\mathrm{X}}]} \qquad \textbf{Equation 2.12}$$

$$\mathrm{K}_{\mathrm{hydr}} = \frac{[\mathrm{OH}_{\mathrm{O}}^{\bullet}]^2}{[\mathrm{v}_{\mathrm{O}}^{\bullet\bullet}][\mathrm{O}_{\mathrm{O}}^{\mathrm{X}}] p_{\mathrm{H_2O}}} \qquad \textbf{Equation 2.13}$$

In addition, for electronic defects the equilibrium constant for intrinsic ionisation is always valid:

$$\mathrm{K}_{\mathrm{i}} = np \qquad \textbf{Equation 2.14}$$

At very low p_{O_2}, the equilibrium Equation 2.3 will be shifted to the product side making oxygen vacancies and electrons the majority defects in this region. It can therefore be assumed that under dry conditions $2[\mathrm{v}_{\mathrm{O}}^{\bullet\bullet}] \gg p, [\mathrm{OH}_{\mathrm{O}}^{\bullet}]$ and $n \gg [\mathrm{Acc}^{/}]$. The reduced electroneutrality then becomes $2[\mathrm{v}_{\mathrm{O}}^{\bullet\bullet}] = n$. Substituting this expression into the equilibrium constant for the formation of oxygen vacancies (Equation 2.12) gives the following function for the concentration of the majority defects:

$$n = 2[\mathrm{v}_{\mathrm{O}}^{\bullet\bullet}] = \left(2\mathrm{K}_{\mathrm{v}_{\mathrm{O}}^{\bullet\bullet}}\right)^{\frac{1}{3}} {p_{\mathrm{O}_2}}^{-\frac{1}{6}} \quad \textbf{Equation 2.15}$$

The concentration of the minority defects, p and $[\mathrm{OH}_{\mathrm{O}}^{\bullet}]$, is similarly found by substitution into Equation 2.14 and Equation 2.13 respectively:

$$p = \mathrm{K}_{\mathrm{i}}\left(2\mathrm{K}_{\mathrm{v}_{\mathrm{O}}^{\bullet\bullet}}\right)^{-\frac{1}{3}} {p_{\mathrm{O}_2}}^{\frac{1}{6}} \quad \textbf{Equation 2.16}$$

$$[\mathrm{OH}_{\mathrm{O}}^{\bullet}] = \left(\frac{1}{4}\mathrm{K}_{\mathrm{v}_{\mathrm{O}}^{\bullet\bullet}}\right)^{\frac{1}{6}} {\mathrm{K}_{\mathrm{hydr}}}^{\frac{1}{2}} {p_{\mathrm{O}_2}}^{-\frac{1}{12}} {p_{\mathrm{H_2O}}}^{\frac{1}{2}} \quad \textbf{Equation 2.17}$$

As the p_{O_2} increases, the material enters an extrinsic region, where the concentration of the majority defect is determined by the concentration of the dopant i.e. the reduced electroneutrality is $2[\mathrm{v}_{\mathrm{O}}^{\bullet\bullet}] = [\mathrm{Acc}^{/}]$. Thus, at a moderate p_{O_2} and dry conditions, it can be assumed that $n \ll [\mathrm{Acc}^{/}]$ and $2[\mathrm{v}_{\mathrm{O}}^{\bullet\bullet}] \gg [\mathrm{OH}_{\mathrm{O}}^{\bullet}], p$. This indicates that the concentration of ionic point defects will be independent of p_{O_2} in this region, while the concentration of the electronic defects will have the following dependencies:

$$n = \left(2\mathrm{K}_{\mathrm{v}_{\mathrm{O}}^{\bullet\bullet}}\right)^{\frac{1}{2}} \left[\mathrm{Acc}^{/}\right]^{-\frac{1}{2}} {p_{\mathrm{O}_2}}^{-\frac{1}{4}} \quad \textbf{Equation 2.18}$$

$$p = \mathrm{K}_{\mathrm{i}}\left(2\mathrm{K}_{\mathrm{v}_{\mathrm{O}}^{\bullet\bullet}}\right)^{-\frac{1}{2}} \left[\mathrm{Acc}^{/}\right]^{\frac{1}{2}} {p_{\mathrm{O}_2}}^{\frac{1}{4}} \quad \textbf{Equation 2.19}$$

At the highest levels of p_{O_2}, the equilibrium in Equation 2.3 will be shifted towards the reactant side of the equation resulting in holes being the majority defect charge-compensating the acceptors i.e. the reduced electroneutrality is $p = [\mathrm{Acc}^{/}]$. The concentration of the electronic defects is therefore independent of p_{O_2}. The concentration of the ionic defects is found by substitution of the reduced electroneutrality into the equilibrium constant expressions Equation 2.12, Equation 2.13 and Equation 2.14:

$$[\mathrm{v}_{\mathrm{O}}^{\bullet\bullet}] = \mathrm{K}_{\mathrm{v}_{\mathrm{O}}^{\bullet\bullet}} {\mathrm{K}_{\mathrm{i}}}^{-2} [\mathrm{Acc}^{/}]^2 {p_{\mathrm{O}_2}}^{-\frac{1}{2}} \quad \textbf{Equation 2.20}$$

$$[\mathrm{OH}_{\mathrm{O}}^{\bullet}] = \left(\mathrm{K}_{\mathrm{v}_{\mathrm{O}}^{\bullet\bullet}} \mathrm{K}_{\mathrm{hydr}}\right)^{\frac{1}{2}} {\mathrm{K}_{\mathrm{i}}}^{-1} [\mathrm{Acc}^{/}] {p_{\mathrm{O}_2}}^{-\frac{1}{4}} {p_{\mathrm{H_2O}}}^{\frac{1}{2}} \quad \textbf{Equation 2.21}$$

The varying p_{O_2}dependencies of the different point defect concentrations are summarised in a Brouwer diagram (Figure 2.2a), which can be very useful for the interpretation of conductivity trends in materials such as $CaSn_{0.95}Sc_{0.05}O_{3-\delta}$.

2.1.5. Concentration of defects as a function of p_{H_2O}

In addition to p_{O_2}, concentrations of defects may similarly also depend on the partial pressure of water vapour, p_{H_2O}. From the hydration reaction (Equation 2.6), an increase in p_{H_2O} at constant p_{O_2} should result in the formation of protonic defects if p_{O_2} is of an appropriate order of magnitude (should be low enough for $2[v_O^{\bullet\bullet}] \gg p$). Conversely, a low p_{H_2O} i.e. a dry atmosphere should shift the equilibrium towards oxygen vacancies meaning that these will be fully charge-compensated by the concentration of the acceptors, $2[v_O^{\bullet\bullet}] = [Acc^{/}]$. In this region, the concentration of the electronic defects will remain constant while the concentration of protons is given by the following:

$$[OH_O^{\bullet}] = \left(\frac{1}{2}K_{hydr}\right)^{\frac{1}{2}} [Acc^{/}]^{\frac{1}{2}} p_{H_2O}{}^{\frac{1}{2}} \qquad \textbf{Equation 2.22}$$

This concentration profile indicates an increase in the proton concentration with p_{H_2O} and at the highest levels of p_{H_2O}, it can be assumed that the protonic defects charge-compensate the acceptors in the material, $[OH_O^{\bullet}] = [Acc^{/}]$. The concentration of the minority defects is then found by substitution:

$$[v_O^{\bullet\bullet}] = K_{hydr}{}^{-1} [Acc^{/}]^2 p_{H_2O}{}^{-1} \qquad \textbf{Equation 2.23}$$

$$n = \left(K_{v_O^{\bullet\bullet}} K_{hydr}\right)^{\frac{1}{2}} [Acc^{/}]^{-1} p_{O_2}{}^{-\frac{1}{4}} p_{H_2O}{}^{\frac{1}{2}} \qquad \textbf{Equation 2.24}$$

$$p = K_i \left(K_{v_O^{\bullet\bullet}} K_{hydr}\right)^{-\frac{1}{2}} [Acc^{/}] p_{O_2}{}^{\frac{1}{4}} p_{H_2O}{}^{-\frac{1}{2}} \qquad \textbf{Equation 2.25}$$

The varying p_{H_2O}-dependencies are summarised in a Brouwer diagram in Figure 2.2b.

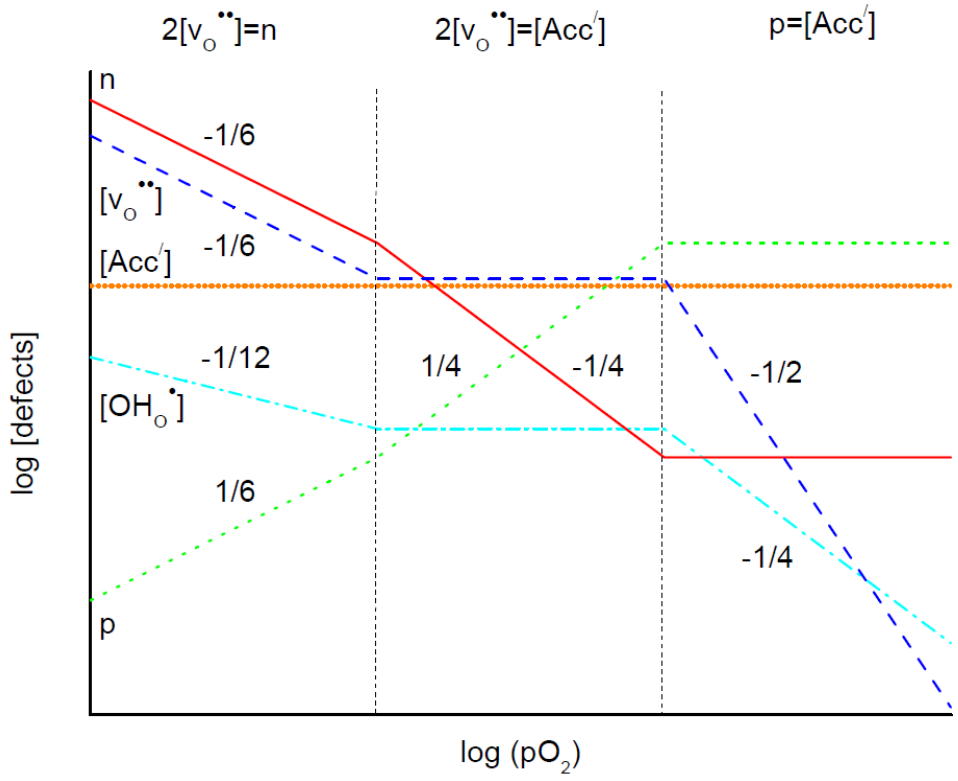

(a)

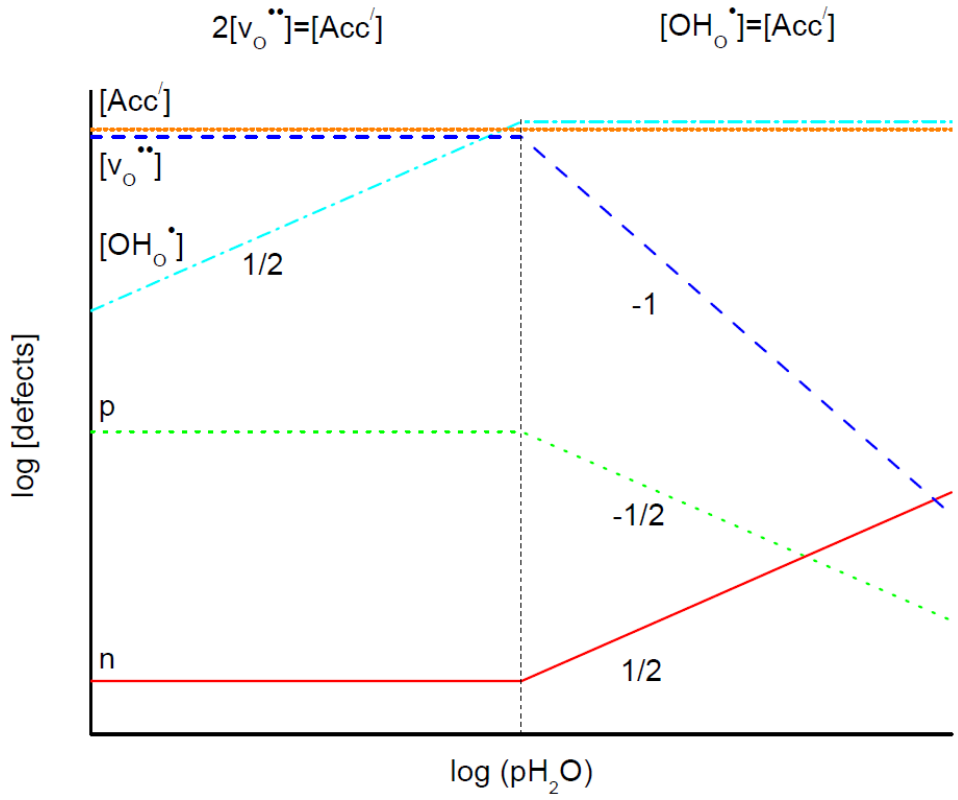

(b)

Figure 2.2: The Brouwer diagram shows how the concentrations of point defects vary as a function of the partial pressure of oxygen (p_{O_2}) and water vapour (p_{H_2O}), (a) and (b) respectively, in $CaSn_{1-x}Sc_xO_{3-\delta}$ and $CaZr_{1-x}Sc_xO_{3-\delta}$.

2.1.6. Hydration thermodynamics in oxides

Oxygen vacancies may be hydrated to form protonic defects in the lattice through the hydration reaction (Equation 2.6). Its equilibrium constant, K_{hydr} from Equation 2.13 may also be described by its standard Gibbs energy, enthalpy and entropy changes, $\Delta_{hydr}G^0$, $\Delta_{hydr}H^0$ and $\Delta_{hydr}S^0$ through

$$K_{hydr} = \exp\left(-\frac{\Delta_{hydr}G^0}{RT}\right) = \exp\left(\frac{\Delta_{hydr}S^0}{R}\right)\exp\left(-\frac{\Delta_{hydr}H^0}{RT}\right) \qquad \textbf{Equation 2.26}$$

The hydration reaction (Equation 2.6) and its equilibrium expression (Equation 2.26) are extremely useful in predicting the proton conduction behaviour in oxides. With them, the proton concentration in any material can be modelled against temperature and pressure with a simple electroneutrality condition. For instance, in Sc-doped $CaZrO_3$ under certain conditions, this would read:

$$2[v_O^{\bullet\bullet}] + [OH_O^{\bullet}] = [Sc_{Zr}^{/}] \qquad \textbf{Equation 2.27}$$

However, not all oxides show this simple tendency of forming protonic defects from oxygen vacancies. For some perovskites with smaller band gaps, holes are found to the charge-compensating defects rather than oxygen vacancies. For instance, $BaPrO_3$ has been predicted to yield a very exothermic hydration enthalpy of oxygen vacancies, but the holes suppress the protons giving rise to a significantly lower enthalpy from the following reaction [19]:

$$H_2O(g) + 2O_O^x + 2h^{\bullet} = 2OH_O^{\bullet} + \frac{1}{2}O_2(g) \qquad \textbf{Equation 2.28}$$

The defect situation is thus quite different with a different electroneutrality condition. Moreover, this hydration reaction is also dependent on the partial pressure of oxygen.

2.2. Electrical conductivity

When an electric field, E, is applied to a sample, charged species will be subject to a force proportional to both the electric field and the charge of the species. This force gives rise to a net current density, i_i, which is then given by:

$$i_i = z_i e c_i u_i E = \sigma_i E \qquad \textbf{Equation 2.29}$$

where σ_i is the partial conductivity of the charge carrier *i* while c_i, u_i and z_ie are the concentration, mobility and charge of the carrier, respectively. The partial conductivity can also be used to define the transport number, t_i, of a charge carrier:

$$t_i = \frac{\sigma_i}{\sigma_{tot}} \qquad \textbf{Equation 2.30}$$

where σ_{tot}, the total conductivity, is the sum of the partial conductivities of all the contributing charge-carrying species. The transport number from Equation 2.30 takes values between 0 and 1, and the sum of the transport numbers of all the charge carriers is always unity.

The transport mechanism of the charge carriers varies from itinerant, large and small polaron mechanisms to an activated hopping process. For most of the work done in this thesis, the charge carriers can often be assumed to occur via activated hopping. In such cases, the conductivity will consist of two exponential temperature dependencies; one from the charge mobility, ΔH_{mob}, and one from the formation of the charge carrier (concentration), ΔH_d.

$$\sigma_i = \frac{\sigma_0}{T}\exp\left(\frac{\Delta H_d + \Delta H_{mob}}{RT}\right) \qquad \textbf{Equation 2.31}$$

By plotting ln ($\sigma_i T$) versus 1/T from Equation 2.31, one can extract both the enthalpy of formation of the charge carriers and the enthalpy of mobility from the slope while all the temperature independent terms such as the entropy of defect formation is included in the pre-exponential factor, which will come out as the intercept.

2.2.1. Isotope effect

When an oxide exhibits proton conductivity, a decrease in the conductivity is observed when switching from a hydrogen-containing atmosphere (H_2 or H_2O) to a deuterium-containing atmosphere (D_2 or D_2O). This is commonly referred to as the isotope effect and is linked to the large mass ratio of the respective hydrogen isotopes. The conductivity can be related directly to diffusion through the Nernst-Einstein relation:

$$\sigma_i = \frac{(z_ie)^2 c_i D_i}{k_B T} \qquad \textbf{Equation 2.32}$$

where D_i is the self-diffusion coefficient of the defect species *i* and k_B is the Boltzmann constant. The self-diffusion coefficient of the defect species is proportional to the frequency of sufficiently energetic jump attempts, ω, which again is proportional to the vibration frequency, ν. Under a simple harmonic oscillator approximation, this vibrational frequency can be equated to:

$$\nu = \frac{1}{2\pi}\sqrt{\frac{k}{\mu}} \qquad \textbf{Equation 2.33}$$

where k is the spring constant of the bond (O-H or O-D in this case) and μ is the reduced mass. Due to the large differences in masses in the hydrogen isotopes, the proton conductivity should decrease substantially when substituting protons ($OH_O^{\bullet}$) with deuterons ($OD_O^{\bullet}$):

$$\sigma_{OH_O^{\bullet}} = \sqrt{2}\sigma_{OD_O^{\bullet}} = 1.414\sigma_{OD_O^{\bullet}} \qquad \textbf{Equation 2.34}$$

This is normally seen as oversimplified as the oscillators themselves have different zero-point energies typically giving protons 0.04-0.06 eV lower activation energy than deuterons. At the same time, it may be further complicated by sticking probability and quantum tunnelling. It is therefore normal to find isotope effects that are both lower and higher than the classical values of 1.414.

2.3. Impedance spectroscopy

Impedance spectroscopy is a very powerful tool for analysing the electrical properties of materials. This is mainly due to the fact that resistive and capacitive elements arising from the bulk and grain boundaries in the polycrystalline material can be separated into separate contributions. In this subsection, the underlying background of the technique will be introduced along with a useful model needed to interpret and analyse obtained results.

2.3.1. Alternating current and impedance

Most commonly, an impedance spectrum is recorded by imposing a small alternating voltage or current on a sample. In contrast to a direct current, the alternating voltage and current vary as a function of time. The sinusoidal voltage, U, is characterised by its angular frequency and amplitude, ω and U_0 respectively, by:

$$U = U_0 \sin(\omega t) \qquad \textbf{Equation 2.35}$$

An applied sinusoidal voltage applied to a circuit will result in a sinusoidal current, I, with the same characteristic frequency but due to capacitive or inductive circuit elements, the current may be phase-shifted by an angle θ relative to the voltage:

$$I = I_0 \sin(\omega t + \theta) \qquad \textbf{Equation 2.36}$$

From Ohm's law, the resistance can be given as the ratio between voltage and current. For alternating currents, the term impedance is used to describe this ratio as well as the phase shift between them. It is given the symbol Z and consists of two components; one that is in phase and one that is π/2 out of phase with respect to the voltage (Equation 2.37). The in-phase part consists of the ratio between the voltage and the in-phase current, giving the real impedance component. It is termed resistance, R, and reflects the impeded transport of charge carriers through the impedance element. The out-of-phase part is similarly the imaginary impedance component and is termed reactance, X. Therefore, the total impedance may also be represented as a two-dimensional vector with a real part along the x-axis and an imaginary part along the y-axis as shown in Figure 2.3 below.

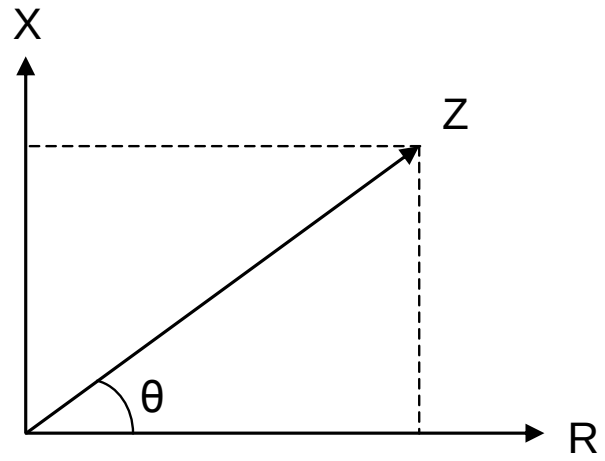

Figure 2.3: Complex impedance

$$Z = \mathrm{Re}(Z) + i(\mathrm{Im}(Z)) = R + iX \qquad \textbf{Equation 2.37}$$

The inverse of the impedance is admittance, Y, and is similarly a complex number obtained by the ratio between current and voltage. The real and imaginary components of the admittance are termed conductance (G) and susceptance (B), respectively:

$$Y = Re(Y) + i\big(Im(Y)\big) = G + iB \qquad \textbf{Equation 2.38}$$

2.3.2. Passive electrical circuit elements

In a polycrystalline material, grains are separated by grain boundaries which give rise to different effects on the charge carriers. The phenomena can be explained by three distinct passive electrical circuit elements that constitute the sample; resistor, capacitor and inductor, which will be discussed briefly.

Resistor

A resistor is an element with long-range transport of charge carriers that gives rise to a conductance, G. Ideally, the voltage across a resistor will instantly give rise to a current and they are therefore considered to be in phase with one another ($\theta = 0$). Consequently, the impedance will only consist of a real part (resistance) that can be given as:

$$Z_{resistor} = R = \frac{U}{I} = \frac{U_0 \sin(\omega t)}{I_0 \sin(\omega t)} = \frac{U_0}{I_0} \qquad \textbf{Equation 2.39}$$

Capacitor

The ideal capacitor consists of two parallel plates separated by vacuum or a dielectric material. As voltage is applied to the plates, charge is built up and the capacitor's ability to store charge depends on its capacitance, C, which is the ratio between the stored charge and the voltage applied. By placing a polarisable medium between the plates, the orientation of the dipoles can reduce the voltage between the plates and consequently increase the resulting capacitance:

$$C = \varepsilon_0 \varepsilon_r \frac{A}{L} \qquad \textbf{Equation 2.40}$$

where ε_r is the dielectric constant (or relative permittivity) of the medium, A is the area of the plates and L is the distance between them. As an alternating voltage is applied over the capacitor, a phase-shifted current will be produced with $\theta = \pi/2$. The impedance of a capacitor will therefore consist of one frequency-dependent imaginary part:

$$Z_{capacitor} = \frac{1}{i\omega C} \qquad \textbf{Equation 2.41}$$

Inductor

In contrast to the capacitor, which is an ideal insulator, the inductor is an ideal conductor. It typically consists of a conducting wire shaped as a coil with no resistance. As a sinusoidal voltage is applied over the inductor, a phase-shifted current with $\theta = -\pi/2$ will be produced. The impedance of an inductor will therefore similarly consist of one frequency-dependent imaginary part:

$$Z_{inductor} = i\omega L \qquad \textbf{Equation 2.42}$$

where L is the inductance of the inductor with units given in henry, H.

These three passive circuit elements can be combined in several different ways to describe the electrical impedance response from all polycrystalline samples.

2.3.3. Impedance sweeps

In an impedance spectroscopy experiment, complex impedance is normally measured over a large range of frequencies. It is then plotted in a so-called Nyquist diagram (-X versus R), which for many polycrystalline materials exhibits one or more semicircles that can be described using different combinations of the before mentioned passive circuit elements. These semicircles can correspond to contributions from the grain interiors, the grain boundaries and the interface between the electrode and the electrolyte. A common way of describing one of the contributions is with a resistor and a capacitor connected in parallel (RC). Thus, three (RC) subcircuits connected in series could be used to describe a typical impedance response from a polycrystalline sample (Figure 2.4).

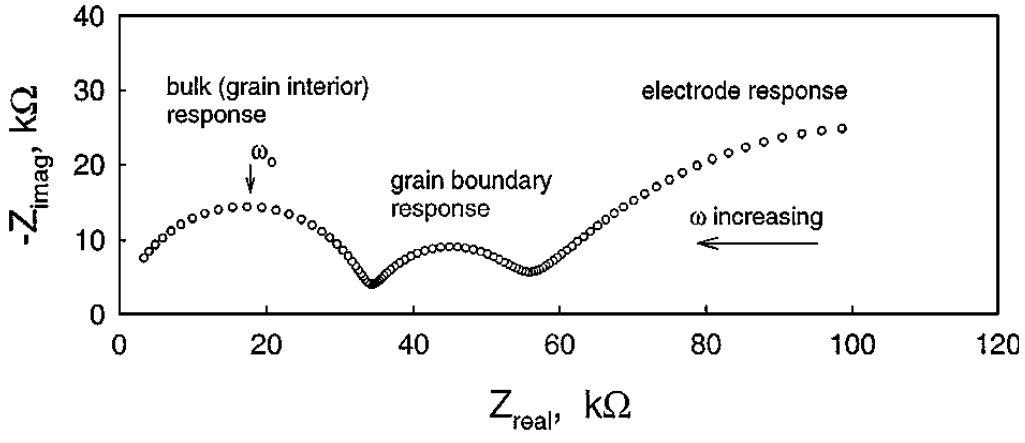

Figure 2.4: Typical impedance response from a polycrystalline sample. Taken from [20].

A notable feature of these semicircles is that the frequency at the apex corresponds to the characteristic frequency, ω_0 of each of the subcircuits (RC). From Equation 2.39 and Equation 2.40 above, it can be found that ω_0 is given by [21]:

$$\omega_0 = \frac{1}{RC} = \frac{A}{L\rho}\frac{L}{\varepsilon_0\varepsilon_r A} = \frac{\sigma}{\varepsilon_0\varepsilon_r} \qquad \textbf{Equation 2.43}$$

From Equation 2.43 above, it should be noted that ω_0 is independent of the geometry of the sample. Unless working with pyroelectric materials, the dielectric constant of a sample can be considered to be independent of temperature. In this thesis, both $CaZrO_3$ and $CaSnO_3$ belong to centrosymmetric space groups and are therefore by definition not pyroelectric. Thus, the temperature-dependency of the characteristic frequency is almost solely due to the specific conductivity (or resistivity) of the sample. This can also further explain the disappearance of the bulk semicircle at relatively low temperatures. A further increase in temperature would similarly result in the disappearance of the grain boundary semicircle.

In a polycrystalline sample, each grain and grain boundary are different in terms of size and orientation to the current and they will therefore result in different impedances. The total impedance will therefore reflect a distribution in these parameters and this will result in a depression of the semicircles observed in the Nyquist plot. In order to simulate these depressed semicircles, a constant phase element (CPE) is assigned with the symbol Q. A CPE has an admittance given by:

$$Y = Y_0(i\omega)^n = Y_0\left[\omega^n \cos\left(\frac{n\pi}{2}\right) + i\omega^n \sin\left(\frac{n\pi}{2}\right)\right] \qquad \textbf{Equation 2.44}$$

In Equation 2.44 above, Y_0 describes a pseudo-capacitance and n is a constant which can vary between -1 and 1. For instance, a capacitor, resistor and inductor take 1, 0 and -1 as values of n, respectively. A system of many grain boundaries is often well represented by a (RQ) subcircuit with n = 0.75 i.e. they are capacitor-like. This new capacitance can also be substituted in the expression for the characteristic semicircle frequency, ω_0:

$$\omega_0 = \frac{1}{(RY_0)^{\frac{1}{n}}} \qquad \textbf{Equation 2.45}$$

Similarly, the real capacitance of the (RQ) subcircuit is then given by:

$$C = \frac{1}{R\omega_0} = Y_0^{\left(\frac{1}{n}\right)} R^{\left(\frac{1}{n}-1\right)}$$ **Equation 2.46**

2.3.4. Brick layer model

In order to separate the contributions from the grain boundaries and bulk, a model needs to be in place. Two of the most prominent models that often are suggested are the parallel model and the series model, where the latter is more well-known as the brick layer model. In the brick layer model, a polycrystalline material is assumed to consist of uniform cube-shaped grains separated by grain boundaries both in parallel and perpendicular to the direction of the applied field. The conducting species can either flow along the parallel grain boundaries or through the grains but they are in both cases geometrically required to cross the series grain boundaries.

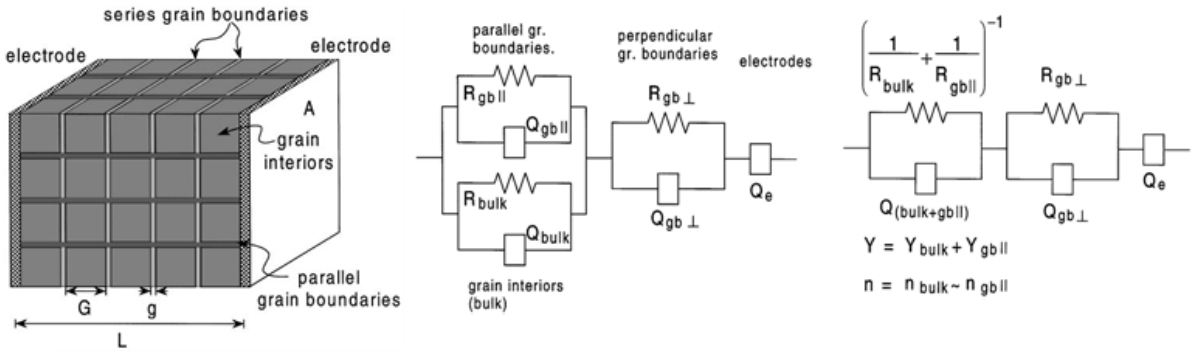

(a) (b) (c)

Figure 2.5: a) Brick layer model, b) equivalent circuit, c) reduced equivalent circuit. All taken from [21].

The geometric parameters are given in Figure 2.5 (a). By defining $\sigma_i = L/AR_i$, with R_i and σ_i being the deconvoluted resistance and specific conductivity from the "ith" semicircle response respectively, it can be found that:

$$\sigma_1 = \left(\frac{2g}{G}\sigma_{gb} + \sigma_{bulk}\right)$$ **Equation 2.47**

$$\sigma_2 = \left(\frac{G}{g}\sigma_{gb}\right)$$ **Equation 2.48**

With these expressions, the specific conductivity of the grain boundary and the bulk, σ_{gb} and σ_{bulk} respectively, can be determined by the sample's microstructure (G and g) and σ_1 and σ_2 obtained directly from an impedance sweep.

However, for the semicircles to be separable into the two contributions it is necessary that σ_{bulk} is greater than σ_{gb}, R_1 and R_2 have to have comparable orders of magnitude and the characteristic frequencies should be significantly different. If fulfilled, the first semicircle can be associated with bulk and the second with perpendicular grain boundaries. The specific conductivities can then be given as:

$$\sigma_{bulk} = \sigma_1 \qquad \textbf{Equation 2.49}$$

$$\sigma_{gb} = \frac{g}{G}\sigma_2 \qquad \textbf{Equation 2.50}$$

As can be seen in Equation 2.49 and Equation 2.50, there is still a need for microstructural parameters in order to find the specific conductivity of the grain boundaries. On the other hand, the ratio g/G can be obtained by considering the capacitances of the (RQ) subcircuits. Due to the unfavourable geometry of the parallel grain boundaries (small area, long length), the conducting species would rather utilise the larger area offered by the bulk (grain interiors). Consequently, the parallel grain boundaries have a negligible contribution to the capacitance C_1. C_1 can then be considered to be solely associated with the bulk while C_2 is due to the perpendicular grain boundaries. Also with the dielectric constants of the bulk and the grain boundary (ε_{bulk} and ε_{gb}) often being similar, $(C_1/C_2) = g/G$, which ultimately gives:

$$\sigma_{gb} = \frac{C_1}{C_2}\sigma_2 \qquad \textbf{Equation 2.51}$$

It is therefore possible to find the specific conductivity contributions from both the bulk and the grain boundaries even without microstructural observations. However, if there were to only be one semicircle observed in the Nyquist plot, impedance data alone cannot determine σ_{bulk} and σ_{gb}. In such a case, the semicircle might correspond to R_{bulk}, $R_{gb,perpendicular}$ or a combination of the two.

2.4. Space charge layer theory

The relative differences in resistance between the grain boundaries and the grain interiors were first attributed to segregation of impurities and secondary phases. However, studies using high resolution transmission electron microscopy (HR-TEM) indicated an intrinsic

grain boundary resistance [13]. An increasingly accepted model that has been used successfully in interpreting this phenomenon in traditional oxygen ion conductors such as acceptor-doped ZrO_2 and CeO_2 is the space charge layer theory [22-24]. It has also recently gained more interest with its extension towards proton conductivity in materials such as acceptor-doped $Er_2Ti_2O_7$ [9], $LaNbO_4$ [25] and $BaZrO_3$ [26, 27].

In electrical terms, a grain boundary consists of a grain boundary core and two adjacent space charge layers of width, λ^* as illustrated in Figure 2.6. In principle, the core can be either positively or negatively charged, but it will here be treated as positively charged for simplicity. To maintain electroneutrality, the positively charged core needs to be balanced. It is therefore compensated by a negative charge in the adjacent space charge layers by a depletion and accumulation of the positively and negatively charged defects, respectively. This causes an electrostatic potential difference between the grain boundary core and the bulk, which is termed the Schottky barrier height, $\Delta\varphi(0)$, which increases with the number of positively charged defects in the core. Thus, a higher $\Delta\varphi(0)$ would correspond to a greater depletion of positively charged defects such as $OH_O^{\bullet}$, while negatively charged defects such as e' will equally increase. Thus, in a case where oxygen vacancies or protons are the majority charge carrier in the material, the resistance in the grain boundaries will be higher than in the bulk.

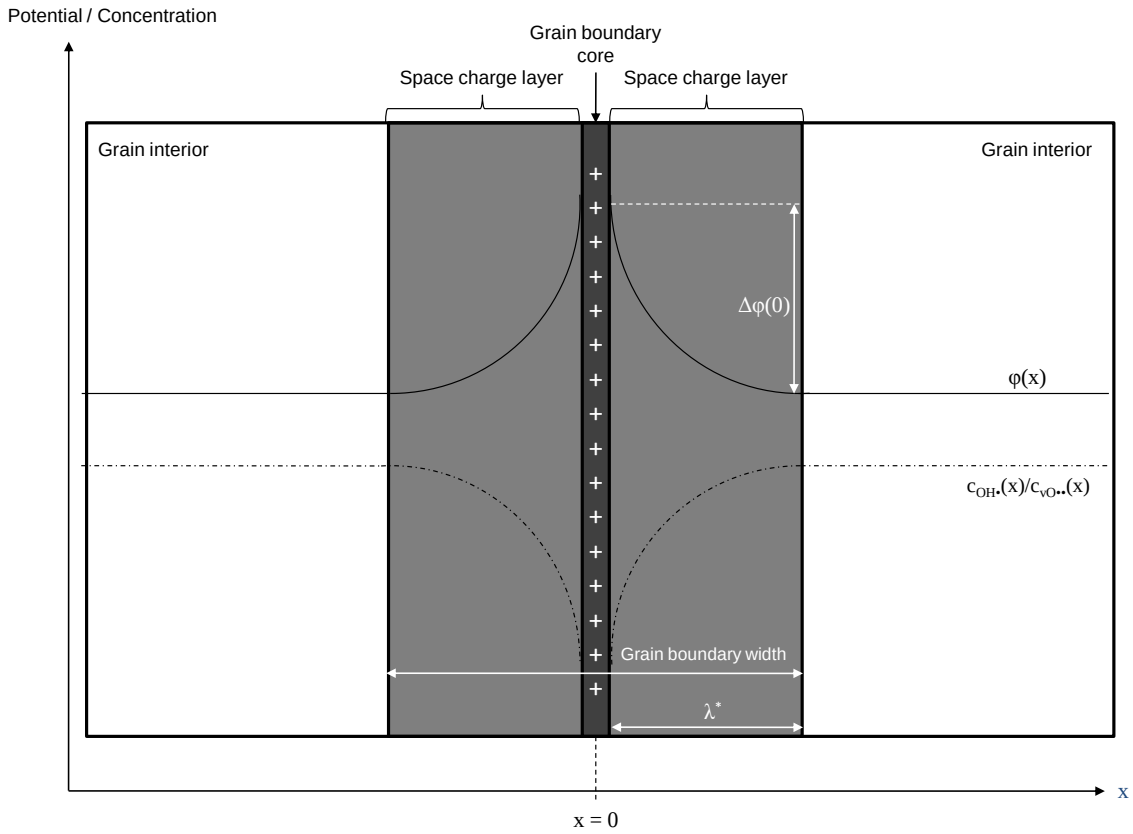

Figure 2.6: Schematic representation of a grain boundary consisting of a positively charged grain boundary core compensated by two adjacent space charge layers. The dotted lines represent the concentration profiles for protons, holes or any other positively charged defect. It should be noted that the slope changes with effective charge i.e. depletion is more severe for oxygen vacancies. The solid lines represent the potential profile.

To quantitatively describe the grain boundary properties, one needs to solve Poisson's equation:

$$\frac{d^2\Delta\varphi(x)}{dx^2} = -\frac{1}{\varepsilon}Q(x) \qquad \textbf{Equation 2.52}$$

where ε is the dielectric permittivity, $Q(x)$ is the net charge density and $\Delta\varphi(x)$ is the electrostatic potential at position x in the space charge layer.

First consider a material with a defect scenario where the oxygen vacancies are charge-compensated by the acceptors. In order to come to a solution to the equation (Equation 2.52), some assumptions have to be in place:

1) The acceptors are immobile and their concentration is thus constant.

2) Equilibrium applies such that the electrochemical potential of mobile oxygen vacancies is equal in the bulk and space-charge layer i.e. $\eta_{v_O^{\bullet\bullet}}(\infty) = \eta_{v_O^{\bullet\bullet}}(x)$
3) Depletion approximation: Oxygen vacancies are so heavily depleted, so that $Q(x)$ is only given by the concentration of acceptors.
4) Mott-Schottky approximation: Acceptor concentration is constant up to the grain boundary core.
5) Boundary conditions to solve equation: $\Delta\varphi(0) = \text{constant}$ and $\Delta\varphi(\lambda^*) = 0$.

With these conditions in place, the solution to Poisson's equation becomes:

$$\Delta\varphi(x) = \frac{e c_{Acc/}(\infty)}{2\varepsilon}(x - \lambda^*)^2 \qquad \textbf{Equation 2.53}$$

where $c_{Acc/}(\infty)$ is the volume concentration of acceptors in the bulk and λ^* is the effective space charge layer width and is given by:

$$\lambda^* = 2L_D\left(\frac{e\Delta\varphi(0)}{k_B T}\right)^{\frac{1}{2}} \qquad \textbf{Equation 2.54}$$

The Debye length, L_D, describes at what distance the grain boundary core's positive charge significantly affects the defects' concentration profile. This length is defined as:

$$L_D = \left(\frac{\varepsilon k_B T}{2e^2 c_{Acc/}(\infty)}\right)^{\frac{1}{2}} \qquad \textbf{Equation 2.55}$$

Using the above equations, one may obtain an expression for the relative volume concentration of oxygen vacancies as a function of position x in the space charge layer:

$$\frac{c_{v_O^{\bullet\bullet}}(x)}{c_{v_O^{\bullet\bullet}}(\infty)} = \exp\left[-\frac{1}{2}\left(\frac{x - \lambda^*}{L_D}\right)^2\right] \qquad \textbf{Equation 2.56}$$

Similar expressions may also be obtained for the concentrations of protons and electron holes:

$$\frac{c_{OH_O^{\bullet}}(x)}{c_{OH_O^{\bullet}}(\infty)} = \exp\left[-\frac{1}{4}\left(\frac{x - \lambda^*}{L_D}\right)^2\right] \qquad \textbf{Equation 2.57}$$

$$\frac{c_{h\bullet}(x)}{c_{h\bullet}(\infty)} = \exp\left[-\frac{1}{4}\left(\frac{x-\lambda^*}{L_D}\right)^2\right] \qquad \textbf{Equation 2.58}$$

From the above equations, it is evident that the concentration of oxygen vacancies depletes more severely than the concentrations of protons and holes due to its double effective charge. This can therefore explain how a material with oxygen vacancies and protons as majority and minority charge carriers respectively seemingly exhibits oxygen vacancy conductivity in the grain interiors and proton conductivity in the grain boundaries.

Assuming that the charge mobility of the charge carriers is the same in the grain boundaries and the bulk of the material, the conductivity as a function of position x in the space charge layer may be obtained:

$$\sigma(x) = \sigma(\infty)\exp\left(\frac{2e\Delta\varphi(x)}{k_B T}\right) = \sigma_{bulk}\exp\left(\frac{2ze\Delta\varphi(x)}{k_B T}\right) \qquad \textbf{Equation 2.59}$$

The conductivity of the space charge layer, σ_{gb}, may then be evaluated by integrating over all positions x in the space charge layer (0 to λ^*):

$$\frac{\sigma_{bulk}}{\sigma_{gb}} = \frac{1}{\lambda^*}\int_0^{\lambda^*} \exp\left(\frac{2ze\Delta\varphi(x)}{k_B T}\right) dx \qquad \textbf{Equation 2.60}$$

There is no analytical solution to this integral, but it can be solved numerically to give:

$$\frac{\sigma_{bulk}}{\sigma_{gb}} \cong \frac{k_B T}{2ze\Delta\varphi(0)}\exp\left(\frac{ze\Delta\varphi(0)}{k_B T}\right) \qquad \textbf{Equation 2.61}$$

From this, the Schottky barrier height can be evaluated given that the grain boundary and bulk conductivities are dominated by the same charge carrier. If the material is in a temperature-regime where the concentration of the majority charge carrier is unchanged, the conductivity can easily be related to its bulk conductivity activation energy (Equation 2.31). Similarly, the activation energy of the grain boundary conductivity can be found using:

$$E_{A,gb} = E_{A,bulk} + (ze\Delta\varphi(0) - k_B T)\left[1 + \frac{1}{T}\frac{d\left(\ln\Delta\varphi(0)\right)}{d\left(\frac{1}{T}\right)}\right] \qquad \textbf{Equation 2.62}$$

From this equation, it can be noted that the activation energy of the grain boundary, $E_{A,gb}$, consists of two contributions; one reflecting the mobility ($E_{A,bulk}$) and one reflecting the concentration profile of the charge carriers in the space charge layer. The latter term is dependent on the Schottky barrier height as well as its temperature dependency.

3. Literature

3.1. The $ASnO_3$ series (A = Ca, Sr and Ba)

As there is limited literature available on the electrical properties and defect structure of $CaSnO_3$, related perovskites such as $BaSnO_3$ and $SrSnO_3$ are discussed to give an indication of its properties in relation to the work done in this thesis.

3.1.1. Crystal structure of $ASnO_3$ (A = Ca, Sr and Ba)

$CaSnO_3$ is reported to be a distorted perovskite oxide in the orthorhombic space group $Pbnm$ (# 62). Using the Glazer notation [28], it occupies a three-tilt $a^+a^+c^-$ system indicating two in-phase tilts of the same magnitude along the a- and b-axis and one anti-phase tilt along c-axis of a different magnitude for the SnO_6 octahedra [29]. By increasing the size of the A-site cation in the order Ca → Sr → Ba, the magnitude of the tilting decreases resulting in higher tolerance factors and degrees of symmetry, as shown in Figure 3.1. This is further demonstrated in Table 3.1 where the Sn-O-Sn angle decreases due to the octahedral tilting. $BaSnO_3$ occupies the cubic space group $Pm\bar{3}m$ (# 221), while $SrSnO_3$ occupies the same space group as $CaSnO_3$ [30]. However, while $BaSnO_3$ exhibits no known phase transitions as a function of temperature, $SrSnO_3$ has been found to undergo a continuous transition from $Pbnm$ to orthorhombic $Imma$ at 909 K and a first-order transition to the tetragonal $I4/mcm$ phase at 1073 K [31]. $CaSnO_3$ is only reported to undergo a transition to a post-perovskite $Cmcm$ phase above 40 GPa at 2000 K [32], which is considered to be outside the range of interest for this thesis. Due to a lower symmetry, $SrSnO_3$ and $CaSnO_3$ possess two uniquely different oxygen ion positions, which may become limiting for the transport of defects. It should additionally be noted that substitutions for Sn^{4+} with larger or smaller ions will result in higher and lower degrees of tilting, respectively. In other words, Y^{3+} (0.90 Å [33]) and Sc^{3+} (0.745 Å [33]) as substituents for Sn^{4+} (0.69 Å [33]) will effectively lower the symmetry in these systems.

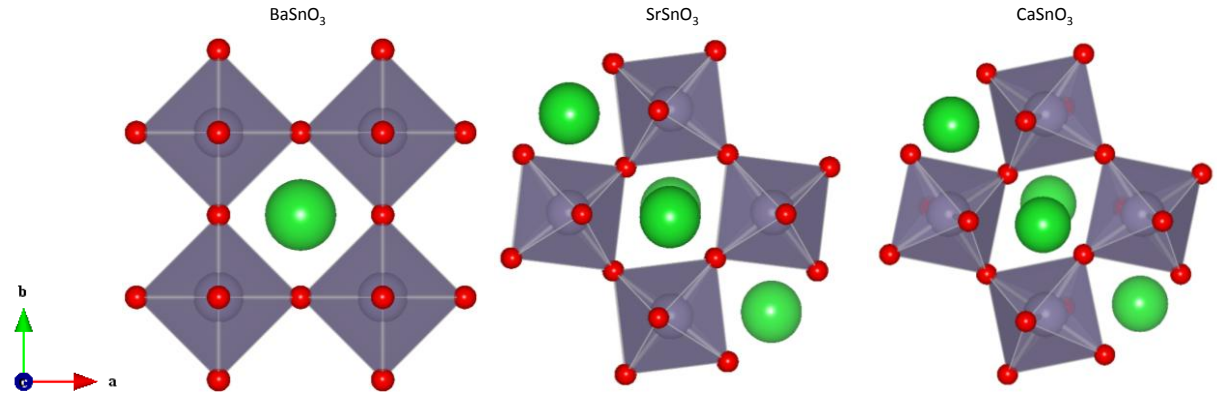

Figure 3.1: Projection of the room temperature phases of $BaSnO_3$, $SrSnO_3$ and $CaSnO_3$ along the c-axis. The structure has been drawn according to information given by Zhang et al. [30]. Details are summarised in Table 3.1

Table 3.1: Structural details of $ASnO_3$ taken from Zhang et al. [30].

	x	y	z	Wyckoff	Sn-O-Sn angle
Ba	0.5	0.5	0.5	1b	180 °
Sn	0	0	0	1a	
O	0.5	0	0	3d	
Sr	0.5029	0.5215	0.25	4c	160.5 °
Sn	0	0.5	0	4b	
O(1)	0.0623	0.4924	0.25	4c	159.6 °
O(2)	0.7202	0.2808	0.0328	8d	
Ca	-0.01364	0.0528	0.25	4c	146.7 °
Sn	0	0.5	0.5	4b	
O(1)	0.1023	0.4647	0.25	4c	148.2 °
O(2)	0.6961	0.2989	0.0526	8d	

3.1.2. Electrical properties of $ASnO_3$ (A = Ca, Sr, Ba)

In 2007, Zhang et al. [30] investigated the $ASnO_3$ perovskite series and found that they were all wide band gap materials indicating that their conductivity will only constitute minor contributions of electronic conduction. Moreover, the band gaps increased in the order Ba → Sr → Ca suggesting that $CaSnO_3$ exhibits the lowest concentration of electronic defects. The band gaps were estimated from reflectance spectra to be 3.10, 4.06 and 4.44 eV for Ba, Sr and Ca, respectively. The band gap for $BaSnO_3$ is also consistent with previously reported values of 3.4 eV [34], 3.12 eV [35] and 2.95 eV [36]. A trend is also observed in the dielectric constants of this series, with approximate values of 25, 12 and 6 for Ba, Sr and Ca, respectively [31, 37, 38].

Only a few reports exist on the electrical conductivity of this series, where most of the attention has gone to $BaSnO_3$. It has for instance been measured for $BaSn_{1-x}Co_xO_{3-\delta}$ ($x \leq 0.2$) which exhibited an increased grain boundary and bulk conductivity with increasing levels of cobalt substitution. This is consistent with an increasing amount of positive charge carriers such as oxygen vacancies. Parkash et al. [39] attribute the conductivity behaviour to having holes as the majority charge carriers due to positive Seebeck coefficients for all values of x. It is however unlikely that holes are the majority charge carriers given the wide band gap reported for $BaSnO_3$ (3.4 eV) but this may be a result of the mixed valency of cobalt. It has also been observed that $Ba_{1-x}Sr_xSnO_3$ generally has a lower conductivity with higher degrees of Sr substitution. But, it is difficult to ascertain if this is an effect of microstructure, band gap or both, as the former was found to change with x [37]. However, it may reflect a diminishing hole concentration or symmetry reduction of the structure. Other conductivity measurements by Wang [40] have indicated that Y-doped doped $BaSnO_3$ exhibits proton conductivity at low temperatures with hydration enthalpies ranging from -45 to -84 kJ mol^{-1} for dopant levels of 0.05 to 0.375. The corresponding hydration entropies varied from -94 to -129 J K^{-1} mol^{-1}. As such, Wang argued that the best performing $BaSnO_3$ sample was the one with the highest level of Y substitution.

3.2. $CaZrO_3$

3.2.1. Structure

Similarly to $CaSnO_3$ and $SrSnO_3$, $CaZrO_3$ is a distorted perovskite occupying the $Pbnm$ space group. It therefore also possesses two uniquely different oxygen ion positions as shown in Figure 3.2. At room temperature, it exhibits higher degrees of octahedral tilting, which is demonstrated in the Zr-O-Zr angles displayed in Table 3.2. This is also reflected in its tolerance factor, which is 0.914 compared to 0.93 for $CaSnO_3$. It undergoes a transition to a cubic $Pm\bar{3}m$ phase at about 2173 ± 100 K [41]. A compressibility study by Ross et al. using single-crystal X-ray diffraction indicated no analogous transition to a post-perovskite phase up to 8.7 GPa at room temperature as found for $CaSnO_3$ [42].

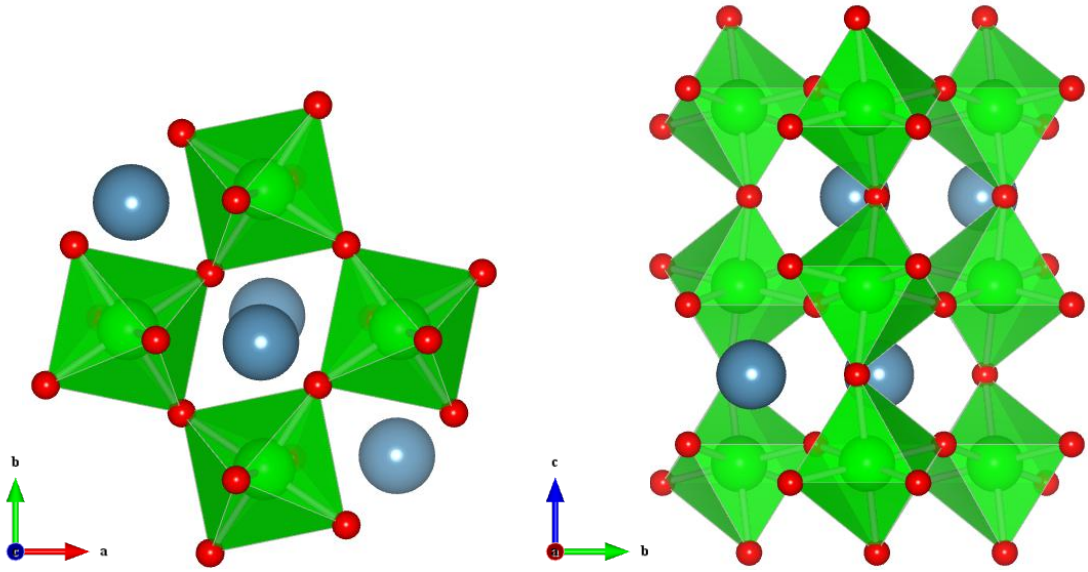

Figure 3.2: Projection of the room temperature phase of $CaZrO_3$ along c-axis (left) and a-axis (right). Structure has been drawn according to information given by Ross et al. [42]. Details are summarised in Table 3.2.

Table 3.2: Structural details of $CaZrO_3$ taken from Ross et al. [42].

	x	y	z	Wyckoff	Zr-O-Zr angle
Ca	0.9886	0.0473	0.25	4c	145.9 °
Zr	0	0.5	0	4b	
O(1)	0.3977	0.9611	0.25	4c	147.0 °
O(2)	0.6979	0.2999	0.0539	8d	

3.2.2. Hydration of acceptor doped $CaZrO_3$

Acceptor doped $CaZrO_3$ is known to be a proton conductor under wet conditions up to elevated temperatures and as such is used as an electrolyte in commercial hydrogen sensors [43]. Measuring the conductivity as a function of p_{O_2} and p_{H_2O} revealed that acceptor doped $CaZrO_3$ is a mixed p-type and proton conducting oxide under oxidising conditions, while it becomes proton conducting under reducing conditions over a wide temperature range [44-47]. Its behaviour indicates a simplified electroneutrality of:

$$[Acc'] = [OH_O^{\bullet}] + 2[v_O^{\bullet\bullet}] \qquad \textbf{Equation 3.1}$$

where the concentration of oxygen vacancies becomes negligible at low temperatures.

Some conductivity measurements as a function of p_{H_2O} have been included in Figure 3.3. These indicate predominating proton conductivities over a wide range of conditions as demonstrated in the presented p_{H_2O} dependencies ($p_{H_2O}{}^{\frac{1}{2}}$ and $p_{H_2O}{}^{0}$).

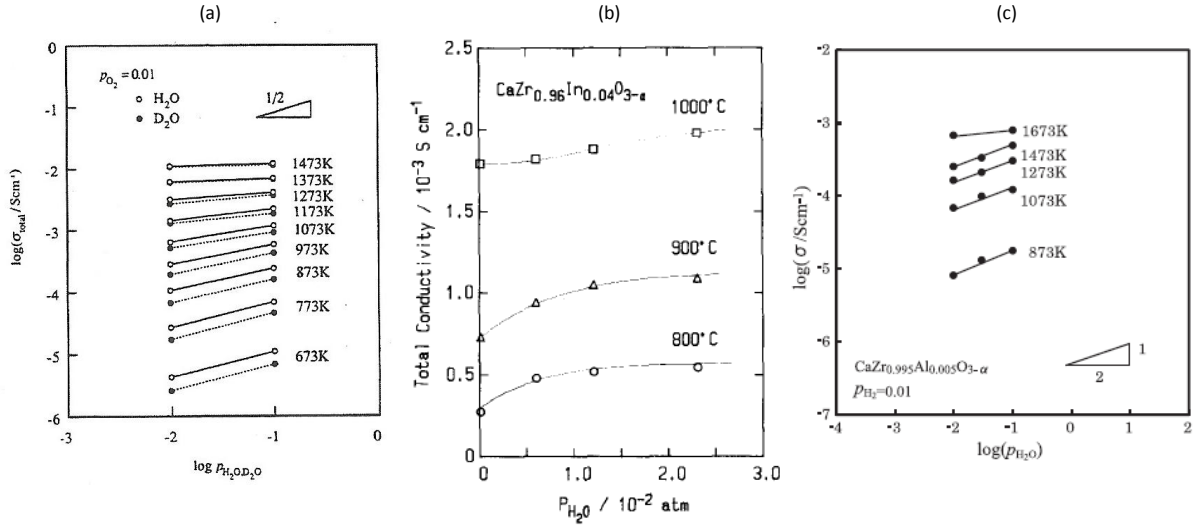

Figure 3.3: Conductivities of acceptor doped $CaZrO_3$ as a function of p_{H_2O} measured at constant p_{O_2}. The acceptor concentration and p_{O_2} decreases in the order a → c. Figures have been taken from Kurita et al. [46], Yajima et al. [48] and Bao et al. [45], respectively.

While most of the literature suggests that acceptor doped $CaZrO_3$ is predominantly proton conducting under reducing conditions up to high temperatures of 1000-1200 °C [45, 46, 48], the thermodynamic parameters for the hydration reaction differ. Based on conductivity measurements, Smith determined the hydration enthalpy of 1 mol % In-doped $CaZrO_3$ to be -87 kJ mol^{-1} with a corresponding entropy change of -64 J K^{-1} mol^{-1} [44]. However, other reports using conductivity and DFT calculations have determined the enthalpy to be more exothermic with values of -194 kJ mol^{-1} [47], -170 kJ mol^{-1} [45] and -146 kJ mol^{-1} [49]. While distinctly different to the low exothermic value reported by Smith, the hydration entropies were also correspondingly higher giving rise to similar proton concentrations at various temperatures. These have also used different levels of doping as well as different dopants, which may influence the thermodynamics. Using atomistic simulation techniques, Davies et al. [50] investigated the change of hydration enthalpies in the $CaZr_{1-x}Y_xO_{3-\delta}$ (CZY) series. They demonstrated that the enthalpy became increasingly exothermic with increasing Y-substitution with values ranging from -58 to -193 kJ mol^{-1} for CZ and CZY10, respectively (Figure 3.4). They suggested this may be due to an increased stability of protonic defects resulting from an increased basicity of the oxide corresponding to previous work done on other Y-doped perovskites by Kreuer et al. [51, 52], Glöckner et al. [53] and Wang [40].

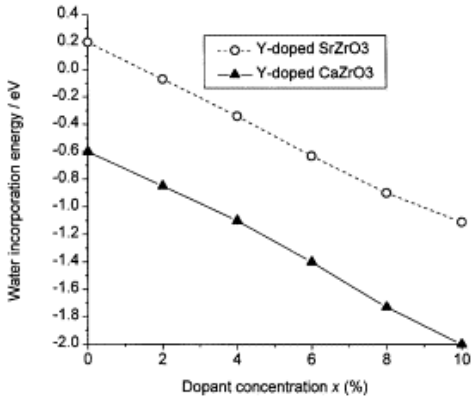

Figure 3.4: The water incorporation energy (hydration enthalpy) becomes increasingly negative with dopant concentration in Y-doped $CaZrO_3$ and $SrZrO_3$. Taken from Davies et al. [50].

The majority of the literature available on proton incorporation in acceptor doped $CaZrO_3$ has indicated a lower hydration than expected based on the concentration of acceptors. For instance, in 0.5 % Al-doped $CaZrO_3$ by Bao et al. [45], the conductivity results were modelled with an effective acceptor concentration of 0.05 % suggesting that only 1/10 of the dopant participated in the proton incorporation. Similar results were indicated for Smith [44] and Kurita et al. [47], where the 10 % doped samples seemed to have effective acceptor concentrations of around 1 and 4 %, respectively. Moreover, the results by Kurita et al. also indicated a smaller proton concentration for the $CaZr_{0.96}In_{0.04}O_{3-\delta}$ than for $CaZr_{0.98}In_{0.02}O_{3-\delta}$. These reduced hydration limits may have connections to the orthorhombic structure of $CaZrO_3$. Islam et al. [54] have found that the two uniquely different oxygen positions, the apical O(1) and the equatorial O(2) sites exhibit distinctly different energies towards proton incorporation. This results in a larger population of protons for the O(1) relative to the O(2) site. Thus a reduced solubility may simply be a result of different hydration thermodynamics of the oxygen sites. Another possible explanation is the formation of positively charged donors in which the substituent occupies the "wrong" site in the perovskite. This has in fact been investigated for $CaZrO_3$ by Islam et al. [55-57] and their investigation indicated that smaller dopants e.g. Sc^{3+} preferentially substitute the Zr-site while the larger cations such as Nd^{3+} substitute the Ca-site. As is indicated in Figure 3.5, it may be difficult to ascertain the selectivity of a Y^{3+} dopant in this system, as it may substitute both sites. The solution energy for In^{3+} has not been calculated but based on its ionic radius of 0.80 Å, it would be reasonable to assume that it will dissolve with a lower energy on the Zr-site (Figure 3.5). However, a small incorporation on the A-site will lower the effective acceptor concentration and thus serves as an additional explanation to the low proton incorporations observed of the beforementioned authors.

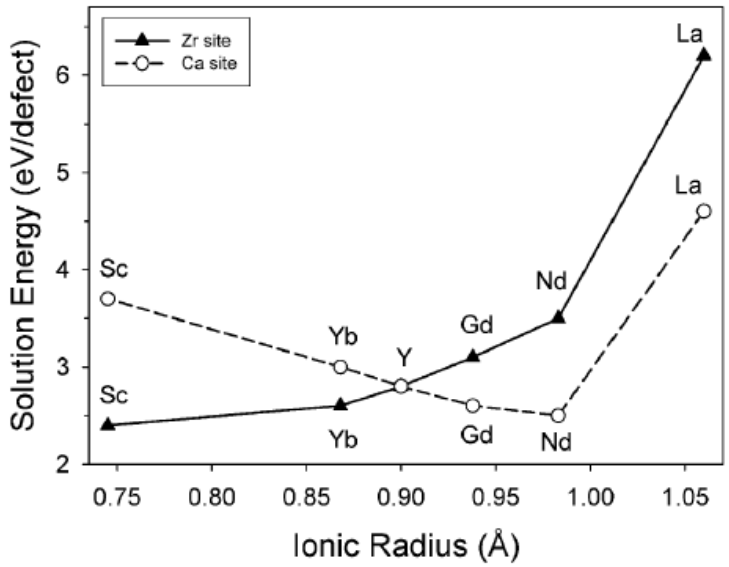

Figure 3.5: Solution energies for trivalent dopant ions at the Ca- and Zr-sites versus dopant ionic radius. Taken from Islam et al. [55].

3.3. Hydration of perovskites

In many oxides, protonic defects are found to be dominating over oxygen vacancies under wet conditions up to relatively high temperatures. Although these defects are present in other oxides than perovskites, much of the data in the literature still suggests proton conductivities of a larger extent in perovskite-type oxides with $BaZrO_3$ being the benchmark for high proton conductivity as can be seen in Figure 3.6. To be able to predict future proton conducting perovskites, correlations between the hydration thermodynamics and materials properties have been sought for.

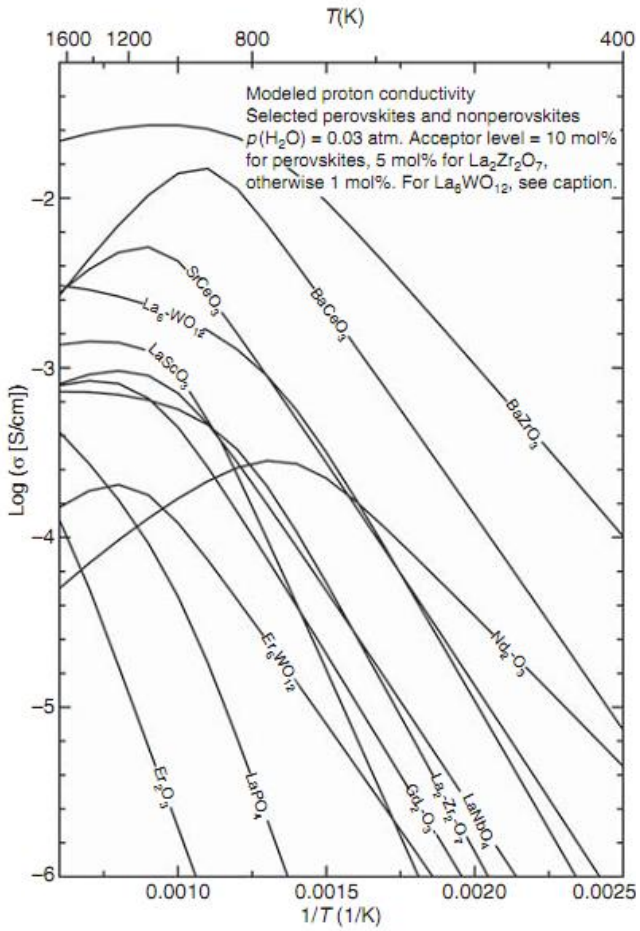

Figure 3.6: Calculated bulk proton conductivities as a function of temperature for a range of oxides found in the literature. "La_6WO_{12}" is an inherently oxygen deficient oxide and as such acts if it has already been acceptor doped. Taken from Norby [58].

The hydration thermodynamics of materials have in actual fact been studied over a number of years using various techniques such as IR spectroscopy, NMR, DFT, thermogravimetry and conductivity measurements. For most of the studied materials, the hydration entropy, $\Delta_{\mathrm{hydr}}S$, has been suggested to be approximately -120 J K^{-1} mol^{-1}, which is consistent with the entropy loss for one mol of gas.

For perovskite oxides, Norby et al. [6, 59] have proposed that the Goldschmidt tolerance factor and the difference in the electronegativity between the B- and A-site cations is somehow related to the hydration enthalpy. For the latter suggestion, this has yielded an empirical formula (Figure 3.7):

$$\Delta_{\mathrm{hydr}}H^0 = -173 + 370\Delta\chi_{\mathrm{B-A}} \qquad \textbf{Equation 3.2}$$

In order to assess this correlation, Bjørheim et al. [49] conducted DFT calculations and conductivity measurements on $PbZrO_3$ for which $\Delta\chi_{\mathrm{B-A}} < 0$. They demonstrated that the

enthalpy of hydration was in fact much less exothermic than predicted by this empirical formula and therefore suggested using the absolute value of $\Delta\chi_{B-A}$ instead, as this could account for such a discrepancy.

However, the current suggested correlations (e.g. Figure 3.7) are often troubled by extensive scattering, which often yields the following questions: Are the underlying theories and assumptions regarding the defect chemistry models wrong or are the correlations themselves too simplistic?

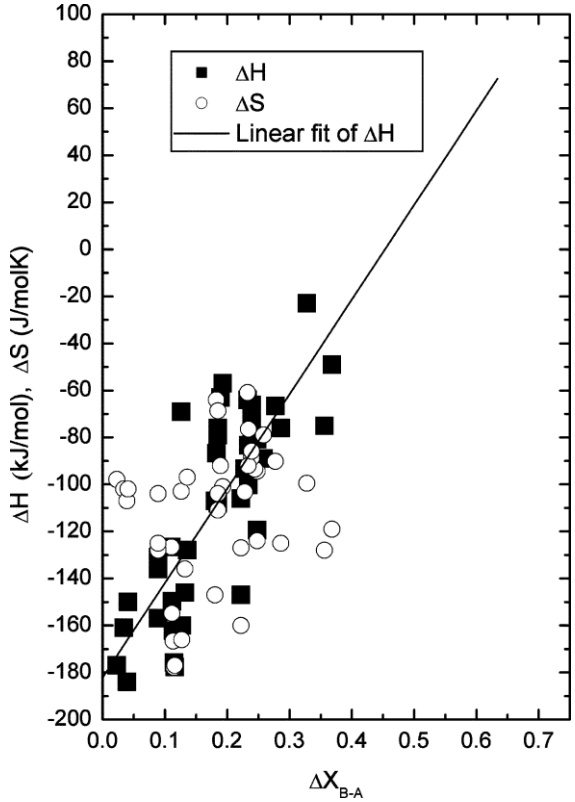

Figure 3.7: There is an apparent relationship between the hydration enthalpy and the difference in electronegativity between the B- and A-site cations. The electronegativities are in the Allred-Rochow scale and the figure is taken from [6].

In the course of tackling these questions, the hydration of acceptor doped $BaZrO_3$ will be the main focus of the discussion. Kjølseth et al. [7] recently employed thermogravimetry (TG) and differential scanning calorimetry (DSC), TG-DSC to evaluate hydration enthalpies of state of the art proton conductors such as Y-doped $BaCeO_3$ and $BaZrO_3$. Kjølseth et al. argue that such a technique eliminates the need for defect modelling, as the enthalpy is evaluated directly by simultaneously monitoring the heat evolved and the mass changes corresponding to hydration. The hydration enthalpy for BZY10 ($BaZr_{0.9}Y_{0.1}O_{2.95}$) was found to be -81 ± 4 kJ mol^{-1} and was consistent over a range of partial pressures of water vapour (0.1-1 atm) and

temperatures (300-900 °C). Additionally, the value was in good agreement with values found from Kreuer et al. (-79.4 kJ mol^{-1}) [51], Schober et al. (-74 kJ mol^{-1}) [60] and Ricote et al. (-83.3 kJ mol^{-1}) [61].

However, there are some large discrepancies in the hydration enthalpies of $BaZrO_3$ evaluated in the literature. In 2008, Yamazaki et al. [62] investigated the water uptake in 20 % Y-doped $BaZrO_3$ using TG over a wide range of temperatures (50-1000 °C) at a constant partial pressure of water vapour. Due to a nonlinearity in the Arrhenius representation (K_{hydr} versus 1/T), Yamazaki et al. suggested that the presence of holes distorts the simplified electroneutrality condition and restricts them from using the high temperature values (above 500 °C). They argue that the concentration of holes cannot be neglected and by only using low temperature enthalpies ranging from -22 to -26 kJ mol^{-1} were evaluated. Even though these values are significantly lower than previous studies suggest, Yamazaki et al. argue that previous work by the beforementioned authors have all made incorrect assumptions regarding a negligible hole concentration. It should also be noted that Yamazaki and his co-workers also found that their values would have been similar (~-100 kJ mol^{-1}) to previous studies if the entire temperature range was employed, which is expected given the general similarities in the data sets obtained.

Kjølseth et al. [7] recently discussed these discrepancies and argued that $BaZrO_3$ with its large band gap and absence of oxidisable cations can only have holes as minority defects compared to oxygen vacancies and protons. Moreover, Kjølseth et al. claim that the enthalpy values are supported by ab initio computer simulations conducted by Bjørheim et al. (-66.6 kJ mol^{-1}) [49]. In the paper, they further suggest that the low temperature regime in the thermogravimetric investigation by Yamazaki and his co-workers may reflect a region where oxygen vacancies are ordered or associated to acceptors. However, recent research by Stokes and Islam [63] using atomistic simulation techniques also demonstrate that $BaZrO_3$ has a low hydration enthalpy (-11.6 kJ mol^{-1}) and as such it is challenging to ascertain the real thermodynamic parameters of this well-studied material.

At the heart of this discussion lies the presence of holes, which may or may not distort the hydration measurements. In light of this, a material dominated by holes such as $BaPrO_3$ [19, 64] might help to shed some light on the discussion. No direct experimental quantification of the hydration enthalpy has been found possible, but Magrasó et al. [19] used the following defect equilibria to calculate the hydration thermodynamics:

$$O_O^X + 2h^\bullet = v_O^{\bullet\bullet} + \frac{1}{2}O_2(g) \qquad \textbf{Equation 3.3}$$

$$\frac{1}{2}H_2O(g) + O_O^X + h^\bullet = OH_O^\bullet + \frac{1}{4}O_2(g) \qquad \textbf{Equation 3.4}$$

Using standard entropy changes for the evolution and consumption of gas (0.5 mol and 0.25 mol, respectively): $\Delta S_{\text{Equation 3.3}} = +60\ \text{J K}^{-1}$ and $\Delta S_{\text{Equation 3.4}} = -30\ \text{J K}^{-1}$ and the fact that $\Delta_{\text{hydr}}H = 2\Delta H_{\text{Equation 3.4}} - \Delta H_{\text{Equation 3.3}}$, Magrasó et al. calculated the hydration enthalpy to be -140 kJ mol^{-1}. This value also corresponds well with modelled results by Stokes et al. (-139.9 kJ mol^{-1}) [63]. However, it is still difficult to ascertain if these values would have been different under reducing atmospheres where the concentration of holes would be negligible.

Putting these problems aside, correlations may still be valuable regardless of discrepancies in the materials, as such correlations might give rise to an increased understanding of the mechanism involved in hydration. Rare earth oxides have been found to correlate to the stability of the oxide using the molar density of oxygen, which can be determined directly from XRD results [65]. This can be explained further by splitting the hydration reaction into two terms; 1) filling of an oxygen vacancy by an oxide ion and 2) protonation of two regular oxygen ions to form two protons:

$$\text{O}_{\text{O}}^{\text{X}} = \text{v}_{\text{O}}^{\bullet\bullet} + \frac{1}{2}\text{O}_2(\text{g}) + 2\text{e}^{/} \qquad \textbf{Equation 3.5}$$

$$\frac{1}{2}\text{H}_2\text{O}(\text{g}) + \text{O}_{\text{O}}^{\text{X}} = \text{OH}_{\text{O}}^{\bullet} + \frac{1}{4}\text{O}_2(\text{g}) + \text{e}^{/} \qquad \textbf{Equation 3.6}$$

The hydration enthalpy can be then be expressed as $\Delta_{\text{hydr}}H = 2\Delta H_{\text{Equation 3.6}} - \Delta H_{\text{Equation 3.7}}$. For rare earth oxides, the first term is quite independent of the type of oxide making $\Delta_{\text{hydr}}H$ strongly dependent on $\Delta H_{\text{Equation 3.7}}$. As this term is not a well-known entity in most oxides, Larring et al. [65] suggested a correlation to the stability of the oxide evidencing that the most stable rare earth oxides exhibited the most exothermic hydration enthalpies. As a measure of the stability, they used the molar density of oxygen claiming that oxygen vacancies are most stable in loosely bound oxides. However, this trend has been demonstrated to be different in perovskites by Kreuer [66]. He suggests that this may be due to the small variations in the lattice basicity of rare earth oxides, while perovskites exhibit low oxygen vacancy formation enthalpies as a result of low bond strengths and strong relaxation effects.

In 1997, Kreuer [67] found that perovskites had an increasing equilibrium constant of hydration upon changing the A-site from Sr to Ba and suggested that this was due to an increased Brönsted basicitiy of the oxide. A few years later in 2003, he [66] reviewed some Sr- and Ba-based perovskites claiming that the equilibrium constant for hydration decreases

in the order cerate → zirconate → stannate → titanate suggesting that this was further evidence for a link to the oxide basicity.

To elucidate the effects of hydration thermodynamics with doping levels, Kreuer investigated Y-doped $BaZrO_3$ (BZY) [51] and $BaCeO_3$ (BCY) [52] where the Y content was varied from 0.02 to 0.20. He found that for both materials, the hydration enthalpy and hydration entropy became increasingly negative with increasing levels of acceptor dopant as shown in Figure 3.8. He furthermore claimed that this was linked to an increase in the Brönsted basicity of the oxide. Such a link to basicity has additionally been verified by Glöckner et al. [53] and Davies et al. [50] where computational results confirmed an increasingly exothermic hydration enthalpy with increasing Y^{3+} substitution for BCY, $CaZr_{1-x}Y_xO_{3-\delta}$ and $SrZr_{1-x}Y_xO_{3-\delta}$.

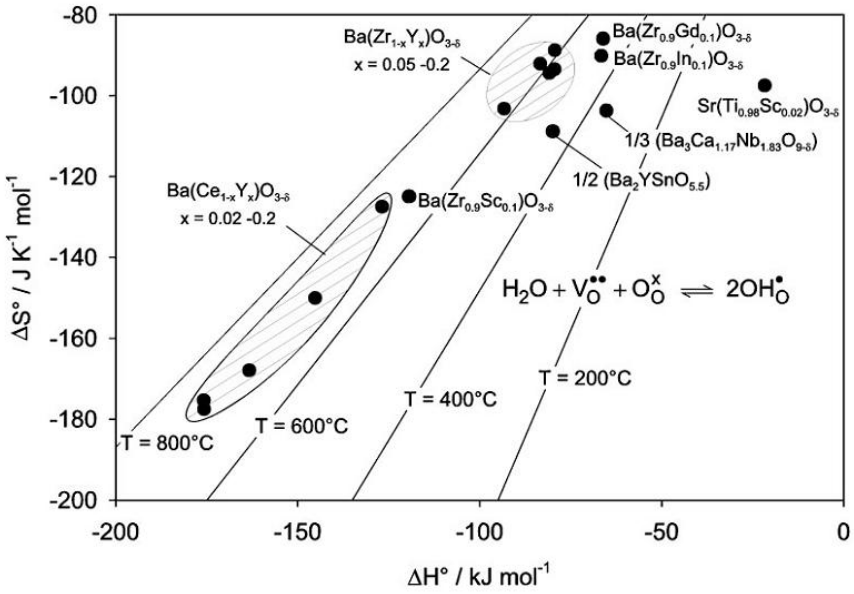

Figure 3.8: Correlation between the entropy and enthalpy of hydration. Different doping levels in $BaCe_{1-x}Y_xO_{3-\delta}$ (BCY) and $BaZr_{1-x}Y_xO_{3-\delta}$ (BZY) exhibit increasingly negative values with increasing x. $BaZrO_3$ doped with 10 % Sc, Gd and In have also been included and show different values to the BZY series. The solid lines represent the dehydration isotherms (K_{hydr} = 1 and p_{H_2O} = 1 atm) where protons remain stable. Taken from Kreuer [66].

Based on work done on acceptor doped $BaZrO_3$ and $BaCeO_3$, Kreuer [66] additionally argued that there exists a correlation between the hydration enthalpy and entropy. Despite an increasingly negative enthalpy, the dehydration temperature consistently has a small variation due to the increasingly negative entropy. He argued that while no complete chemical

understanding of this phenomenon exists, the incorporation of protons is seemingly independent of acceptor dopant concentration as long as the dopant does not affect the electron density of the lattice oxygen. While previous studies have often emphasised that dopants and constituents should ideally have similar ionic radii, Kreuer claims that this approach is too simplistic. In support of this, yttrium seems to be a superior dopant to alternatives such as In and Sc, as the latter seem to reduce the local symmetry thus reducing the saturation limit of the material. Yttrium on the other hand almost does not affect the electron density and thus appears "invisible" for materials such as $BaZrO_3$ and $BaCeO_3$. Various dopants were used and they exhibited different thermodynamics (Figure 3.8), which he suggested to be due to symmetry changes associated with the choice of dopants. In a separate investigation, Kreuer [51] used Mulliken population analysis to investigate the electron density in Y- and Sc-doped samples of $BaZrO_3$. While the Y-doped sample exhibited a close resemblance in the electron densities in the YO_6 and ZrO_6 octahedra, Sc had a much stronger interaction for which the oxygens in the ScO_6 octahedra showed higher electron densities. This suggested that a relation to the electronegativities or basicity of the dopant ions for the incorporation of protons in the oxide exists.

In order to study the proton environment in perovskites, IR spectroscopy measurements have been conducted over the last few years. The characteristic vibrational wavenumber (ν_{OH}) can give an indication of the strength of the OH bond, and as such may help in developing a greater understanding of proton incorporation in oxides. In 2005, Omata et al. [68] investigated the proton environments in hydrated $SrZr_{1-x}Sc_xO_{3-\delta}$ (SZSc) as a function of Sc substitution through IR (Figure 3.9). The results revealed increasing bond strengths with larger degrees of Sc as ν_{OH} was shifted towards higher values. Values of ν_{OH} for some other materials have been included in Table 3.3 and suggest a higher bond strength in the order Ba → Ca → Sr for Ga-doped perovskites. These results thus indicate that the strength of the OH bond cannot be solely attributed to the basicity or electronegativity of the oxide.

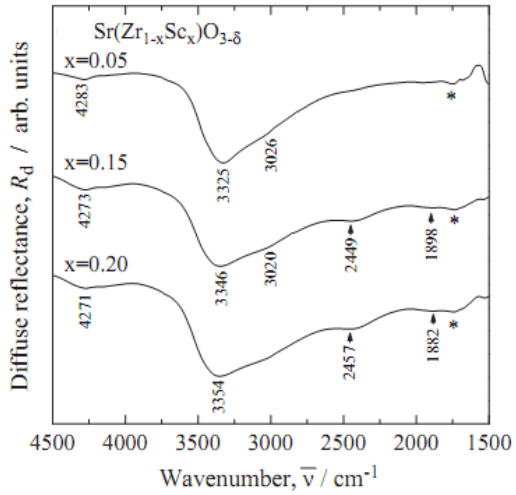

Figure 3.9: IR reflectance spectra of $SrZr_{1-x}Sc_xO_{3-\delta}$ (SZSc) for the ν_{OH} region. Asterisks indicate spectral dips and are not associated with dissolved protons. Taken and modified from Omata et al. [68].

Table 3.3: Vibrational wavenumbers (ν_{OH}) of some perovskites obtained by FTIR experiements. Only the two highest peak values for the OH stretching mode are included. All values have been taken from Omata et al. [69].

Material	ν_{OH} / cm^{-1}	
$BaZr_{0.95}Ga_{0.05}O_{3-\delta}$	3131	2830
$SrZr_{0.95}Ga_{0.05}O_{3-\delta}$	3486	3249
$CaZr_{0.95}Ga_{0.05}O_{3-\delta}$	3451	3366

The solubility of dopants is dependent on the choice of material and dopant and is often found to be high for perovskite-type oxides. Kreuer [66] suggests that symmetry reductions (e.g. from cubic to orthorhombic) often reduces the incorporation of protons due to the formation of several oxygen sites, which in turn may exhibit distinctly different hydration thermodynamics. As similarly discussed for $CaZrO_3$ (section 3.2.2), deviated structures exhibit reduced water solubility limits, e.g. $SrCeO_3$ [70, 71], $SrZrO_3$ [72] and $SrTiO_3$ [66], where the solubility limits ranged from 1.9 % to 3.7 % for nominal acceptor concentrations of 5 %. Such discrepancies led Krug and Schober [72] to suggest three possible explanations: i) dopant atoms occupy the wrong site causing the opposite effective charge as shown in Equation 3.7 for Yb-doped $SrZrO_3$, ii) dopant and oxygen vacancy associate through Equation 3.8 and exhibit less favourable hydration thermodynamics (Equation 3.9) or iii) segregation of dopant to the grain boundaries. It should be additionally noted that at sufficiently low temperatures, the protons may similarly associate with the acceptors according to Equation 3.10, which can effectively lower the proton conductivity of materials.

$$\frac{1}{2}Yb_2O_3 + ZrO_2 = Yb_{Sr}^{\bullet} + Zr_{Zr}^{X} + e^{/} + 3O_O^X + \frac{1}{4}O_2(g) \quad \textbf{Equation 3.7}$$

$$v_O^{\bullet\bullet} + Acc^{/} = (v_O Acc)^{\bullet} \quad \textbf{Equation 3.8}$$

$$H_2O(g) + (v_O Acc)^{\bullet} + O_O^X = 2OH_O^{\bullet} + Acc^{/} \quad \textbf{Equation 3.9}$$

$$OH_O^{\bullet} + Acc^{/} = (OH_O Acc)^X \quad \textbf{Equation 3.10}$$

Associations between acceptors and oxygen vacancies or protons may occur in any oxide and is largely dependent on the binding energy of the associate species. For instance, in $CaZrO_3$, acceptor dopants such as Sc^{3+} are found to be more favourable towards association than Ga^{3+} with values of -0.31 and -0.18 eV respectively. This suggests that trapping of protons is enhanced using Sc rather than Ga as a dopant in $CaZrO_3$ [54]. However, no systematic study of this phenomenon has been conducted further complicating the choice of dopants in oxides.

3.4. Grain boundary conductivity in oxides

High grain boundary resistances have often troubled promising proton conducting oxides such as Y-doped $BaZrO_3$. As is clear from Figure 3.10, the grain boundary conductivities are almost consistently more than one order of magnitude lower than that corresponding to the bulk. In an attempt the elucidate the effects of the grain boundaries due to their detrimental effect on the total conductivity, Iguchi et al. [73] investigated three different compositions in the BZY series (x = 0.05-0.15). The grain boundary conductivity was found to increase by two orders of magnitude with increasing yttrium substitution with values ranging from 3×10^{-8} S cm^{-1} for BZY5 to 2×10^{-6} S cm^{-1} for BZY15 at 300°C in wet O_2 ($p_{H_2O} = 2.3$ kPa). The bulk conductivity was however found to be seemingly independent. Similar results were obtained for $BaCe_{1-x}Gd_xO_{3-\delta}$ (BCGd) where the specific grain boundary conductivity increased by an order of magnitude from x = 0.10 to 0.15 at 300 °C [74].

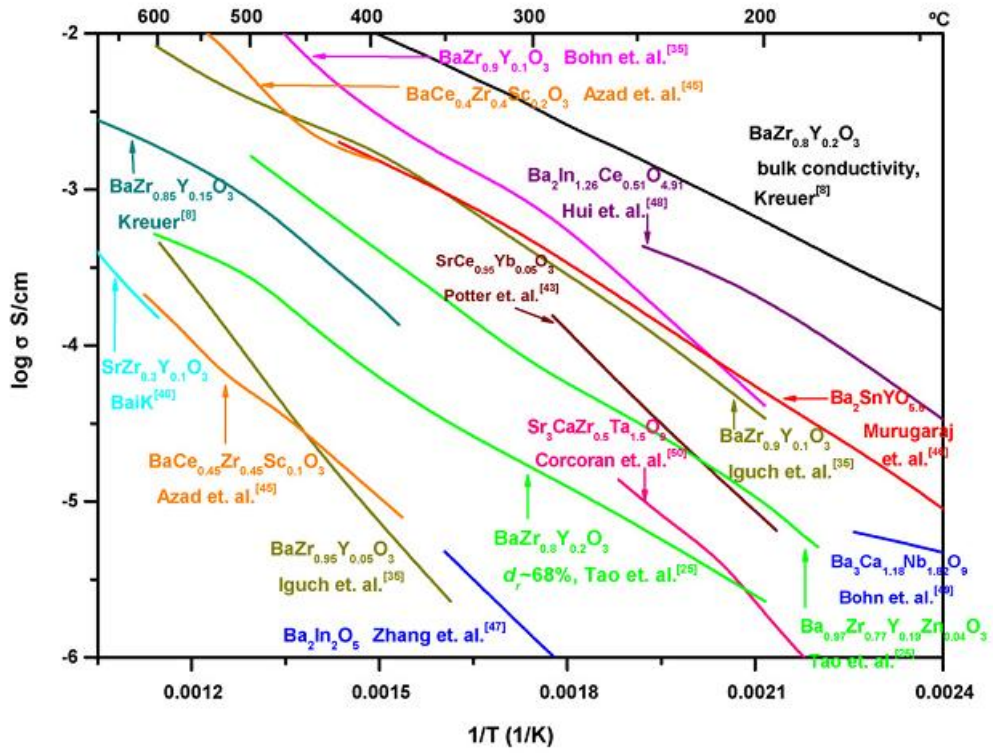

Figure 3.10: Grain boundary conductivities of selected proton conductors available from the literature. The bulk conductivity of BZY20 from Kreuer has been included as a reference. The figure has been taken from Park et al. [74] where all the references are listed.

Investigations involving other A-site cations in $A(Zr,Ce)O_3$ perovskites have only reported modest proton conductivities indicating limited improvements on lowering the grain boundary resistances as can be seen in Figure 3.10 where the grain boundary conductivity of $SrZr_{0.9}Y_{0.1}O_{3-\delta}$ and $SrCe_{0.95}Yb_{0.05}O_{3-\delta}$ by Baik et al. [75] and Potter et al. [76], respectively, have been included. Similar approaches have been attempted by varying the B-site cation in acceptor doped $Ba(Ce_{1-x}Zr_x)O_3$ in which it was found that the specific grain boundary conductivity decreased with increasing x (Figure 3.11) [77]. As shown, both doped samples show a decreased specific grain boundary conductivity with increasing degree of Zr, which is also consistent with previously reported results by Kreuer [66]. While this clearly shows a decreased specific grain boundary conductivity, the total grain boundary resistance will also increase due to smaller grain sizes in the perovskite zirconates. For instance, in work done by Cervera et al. on BZY20, σ_{gb} (not specific) was found to increase by three orders of magnitude at 400 °C when the average grain was varied from 10 to 200 nm [78].

As mentioned, the grain boundary conductivity is consistently lower than its bulk counterpart. The underlying explanation of this, however, differs. The higher resistance has often been attributed to a blocking effect due to a depletion of the charge carriers due to the presence of

space charge layers as described in section 2.4. As mentioned, an increased doping concentration has been found to increase the grain boundary conductivity [73, 74], which has often been explained to be due to an accumulation of $Acc^{/}$ in the space charge layers compensating the positively charged grain boundary core. This was in fact demonstrated with BZY10 by Kjølseth et al. [26] and BZY15 by Groß et al. [79] where EDS spot analysis using TEM consistently indicated a higher yttrium concentration along the grain boundaries relative to the grain interiors. This segregation was argued to occur because of an elastic strain due to the size mismatch of the cations (Y^{3+} and Zr^{4+}). Such a segregation should also decrease the depletion of protons and other positively charged defects to effectively increase the grain boundary conductivity, which is consistent with previous observations for BZY [73, 74] and acceptor doped CeO_2 [24, 80]. This can also be reflected in the Schottky barrier heights, $\Delta\varphi(0)$, which are also found to decrease with increasing levels of acceptors e.g. decreases from ~0.5 V to ~0.4 V for BZY10 to BZY20 [24, 26, 81] at 200-300 °C. It should however be noted that Kjølseth et al. [26] also found that $\Delta\varphi(0)$ was different in wet and dry O_2 (g) for BZY10. They therefore postulated that this difference may reflect a change in the grain boundary core charge. Assuming oxygen vacancies are stabilised in the grain boundary core, the hydration is suggested to compensate oxygen vacancies in the bulk rather than those in the core:

$$H_2O(g) + v^{\bullet\bullet}_{O,bulk} + 2O^{X}_{O,core} = O^{X}_{O,bulk} + 2OH^{\bullet}_{O,core} \qquad \textbf{Equation 3.11}$$

The hydration reaction will then selectively hydrate oxygen vacancies in the bulk and terminate oxygen ions in the core to further decrease the energy differences between the grain boundary core and interior.

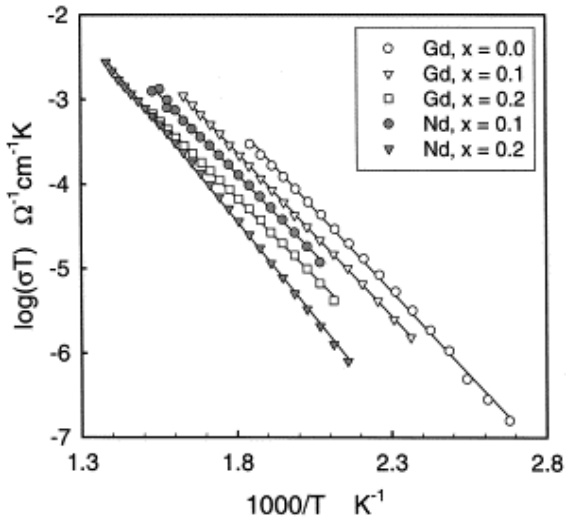

Figure 3.11: The specific grain boundary conductivity as a function of reciprocal temperature (150-450 °C) decreases with increasing Zr content for $BaCe_{0.9-x}Zr_xM_{0.1}O_{3-\delta}$ (M = Gd, Nd). Taken from Ryu et al. [77].

Sintering temperatures have also been found to enforce effects on the grain boundary conductivities. As $BaZrO_3$ may be troubled by evaporation of BaO at higher temperatures, the effects of sintering temperatures on the specific grain boundary conductivities may be unclear. As such, a recent investigation by Sánchez-Bautista et al. [82] on 10,15 and 20 % Dy-doped CeO_2 sintered at temperatures of 1350-1500 °C will instead be presented. They provided evidence for lower specific grain boundary conductivities and higher Schottky barrier heights for the samples that were sintered above 1400 °C suggesting that this reflected a larger depletion of oxygen vacancies. They argued that this could be related to the formation of nanodomains of oxygen vacancies causing a trapping effect. By lowering the temperature to 1400 °C, these domains may be more restrained thus lowering $\Delta\varphi(0)$ and effectively increasing the concentration of oxygen vacancies in the space charge layers. $\Delta\varphi(0)$ was furthermore found to decrease with increasing levels of dysprosium at all sintering temperatures demonstrating a larger segregation of acceptors to the positively charged grain boundary core as already discussed.

The bulk and grain boundaries may also exhibit different dependencies on the partial pressures of water and oxygen. For instance, in BZY10 [26] and acceptor doped CeO_2 [24], it was found that while the bulk conductivity was independent of p_{O_2} reflecting ionic conductivity, the grain boundary conductivity increased weakly with decreasing p_{O_2} under reducing conditions, indicating mixed ionic and n-type conduction. This was suggested to be due to an accumulation of electrons in the space charge layers to compensate for the positive grain boundary core. This has similarly been found in Ca-doped $Er_2Ti_2O_7$, in which the

resistances associated with the grain boundary response exhibited a strong dependency on p_{H_2O}, while the bulk resistance was seemingly independent (Figure 3.12) [9]. For this Fjeld et al. suggested that such a dependency either reflected the presence of a proton conducting siliceous phase in the grain boundaries or a stronger depletion of oxygen vacancies than protons due to the double effective charge through the following concentration profiles:

$$\frac{c_{v_O^{\bullet\bullet}}(x)}{c_{v_O^{\bullet\bullet}}(\infty)} = \exp\left[-\frac{1}{2}\left(\frac{x-\lambda^*}{L_D}\right)\right] \qquad \textbf{Equation 3.12}$$

$$\frac{c_{OH_O^{\bullet}}(x)}{c_{OH_O^{\bullet}}(\infty)} = \exp\left[-\frac{1}{4}\left(\frac{x-\lambda^*}{L_D}\right)\right] \qquad \textbf{Equation 3.13}$$

In an attempt to investigate the effect of silicon impurities, Fjeld [10] prepared four different samples of Ca-doped $Er_2Ti_2O_7$ where both the acceptor dopant concentration and the silicon content varied. By doing so, it was found that the electrical responses of all four samples demonstrated the same dependencies on p_{H_2O} and p_{D_2O} as had been found earlier suggesting that this was in fact a result of the existence of space charge layers and an inherent property of Ca-doped $Er_2Ti_2O_7$.

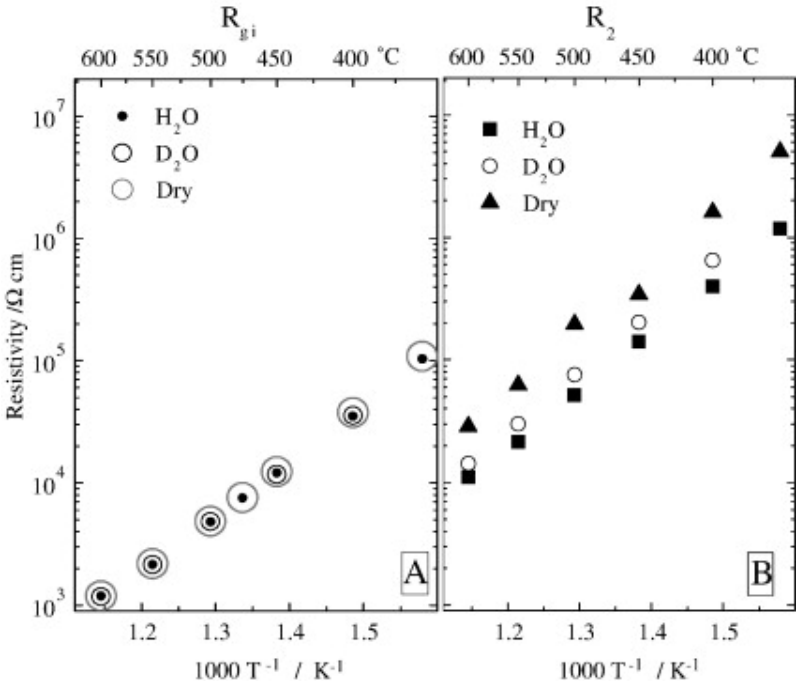

Figure 3.12: Resistivities corresponding to the grain interiors (A) and grain boundaries (B) versus reciprocal temperature for Ca-doped $Er_2Ti_2O_7$ by Fjeld et al. [9].

3.5. Sintering aids in oxides

The use of sintering aids in oxides has shown promising results as it allows improved densification of poorly sinterable materials such as SnO_2 and $BaZrO_3$. By way of example, work done on acceptor doped $BaZrO_3$ will be presented. Babilo and Haile [83] investigated the sintering of BZY15 substituted with 4 mol % ZnO exhibiting a decreased sintering temperature of 1300 °C (1700-1800 °C is normally needed for BZY). The introduction of ZnO was largely segregated to the grain boundaries but no secondary phases were observed from XRD and SEM. As such, the authors attributed the improved sinterability to an increased grain boundary mobility. This was similarly suggested by Park et al. [84] in work done on the use of CuO as a sintering aid in 15-25 % Yb doped $BaZrO_3$. In recent research on Y-doped $Ba(Zr,Ce)O_3$, the use of ZnO was similarly found to segregate in the grain boundaries. However, the authors demonstrated that a eutectic BaO-ZnO phase with a melting temperature of 1098.7 °C was formed and this was in fact responsible for the increased densification process contradicting previous suggestions of improved grain boundary mobilities [85]. While both theories offer explanations to the observed phenomena, no unifying theory is available suggesting that the sintering may be attributed to either one or even both. At the same time, all reports found that excessive use of ZnO in oxides have shown adverse effects on the conduction and suggest that only minimal amounts be used for improved sinterability.

4. Experimental

4.1. Synthesis

4.1.1. Solid state reaction route (SSR)

The SSR method of synthesis was successfully employed for all compositions of $CaZr_{1-x}Sc_xO_{3-\delta}$ and $CaSn_{1-x}Sc_xO_{3-\delta}$ summarised in Table 4.1. SSR is often used in inorganic synthesis due to its simple nature and high success ratio. The reaction between the reactants, which are often oxides or carbonates, is diffusion-limited and the technique therefore often requires high temperatures and repeated runs in order to get a homogenous sample. Disadvantages concerning this type of synthesis include limited control of reaction mechanism, poor distribution of dopants and possibilities of evaporation of volatile constituents due to repeated heating sequences.

Table 4.1: Compositions of samples that were synthesised in the work done for this thesis.

Composition	Abbreviated form	Synthesis
$CaZr_{0.95}Sc_{0.05}O_{3-\delta}$	CZSc5	SSR
$CaZr_{0.9}5Sc_{0.1}O_{3-\delta}$	CZSc10	SSR/WCR
$CaZr_{0.85}Sc_{0.15}O_{3-\delta}$	CZSc15	SSR
$CaZr_{0.8}Sc_{0.2}O_{3-\delta}$	CZSc20	SSR/WCR
$CaSn_{0.95}Sc_{0.05}O_{3-\delta}$	CSSc5	SSR
$CaSn_{0.9}Sc_{0.1}O_{3-\delta}$	CSSc10	SSR
$CaSn_{0.85}Sc_{0.15}O_{3-\delta}$	CSSc15	SSR
$CaSn_{0.8}Sc_{0.2}O_{3-\delta}$	CSSc20	SSR

The starting materials used in the synthesis were $CaCO_3$ (Fluka, 99.0%), $CaCO_3$ (chelometric standard, Sigma-Aldrich, 99.97 %), SnO_2 (Alfa Aesar, 99.9 %), ZrO_2 (gold label, ceramic grade, Aldrich Chemical Company, 99 %), ZrO_2 (Alfa Aesar, 99.7%) and Sc_2O_3 (Reacton, Alfa Aesar, 99.9 %).

Stoichiometric amounts of $CaCO_3$, Sc_2O_3 and SnO_2 or ZrO_2 were mixed in an agate mortar followed by ball milling for 30 minutes at 200 rpm with 15 minutes intervals using isopropanol as the milling medium. After milling, the isopropanol was evaporated in a heating cupboard at 150 °C and the mixed powders were then coldpressed into pellets of 13, 20 or 25 mm diameters using stainless steel dies at a uniaxial pressure of approximately 100 MPa.

The Sc-doped $CaSnO_3$ pellets were calcined at 900 °C for 5 hours followed by three calcinations at 1000 °C for 15 hours. Ball milling was repeated between each calcination to ensure sufficient mixing. Higher calcination temperatures (1100 °C and above) resulted in the formation of a secondary phase of Ca_2SnO_4 presumably due to the evaporation of tin (see section 2.1.2 for more details). To avoid evaporation of tin in the samples, the pellets were covered in their own powder and packed into platinum foil during the calcinations.

The Sc-doped $CaZrO_3$ pellets were calcined twice at 1200 °C and 1400 °C for 15 hours following the work done by Jens Bragdø Smith [44]. Both solid state reactions proceeded through:

$$\mathrm{CaO} + (1 - \mathrm{x})\mathrm{BO}_2 + \frac{\mathrm{x}}{2}\mathrm{Sc}_2\mathrm{O}_3 \rightarrow \mathrm{CaB}_{1-\mathrm{x}}\mathrm{O}_{(3-\delta)} \qquad \textbf{Equation 4.1}$$

where B is either Zr or Sn.

4.1.2. Wet chemical reaction route (WCR)

Additional samples of CZSc10 and CZSc20 (abbreviated form taken from Table 4.1) were synthesised using a WCR with citric acid as a complexing agent.

In this method, the reactants are dissolved in a polyprotic carboxylic acid such as tartaric or citric acid. The cations are then stabilised as citrate complexes and when the solution is heated to its boiling point and dehydrated, the cations are homogeneously distributed in the resulting crust. WCR offers advantages over the traditional solid state synthesis by ensuring sufficient mixing of the reactants as well as lowering the temperatures needed for calcination. However, strong acids are often needed to dissolve the oxides, which may dissolve some of the silica glass presenting themselves as impurities in the samples.

For the syntheses of CZSc10 and CZSc20, the reactants used were $CaCO_3$ (chelometric standard, A.C.S. reagent, Sigma-Aldrich, 99.97 %), Sc_2O_3 (REacton, Alfa Aesar, 99.9 %), $ZrO(NO_3)_2 \bullet xH_2O$ (technical, Sigma-Aldrich), $C(OH)(COOH)(CH_2 \bullet COOH)_2 \bullet H_2O$ (citric acid monohydrate, GPR RECTAPUR, VWR International, 99.5 %) and concentrated HNO_3 (65 %, GR for analysis, Merck).

As the zirconium complex contained an unknown number of crystallised water molecules, a thermogravimetric measurement was conducted. The resulting weight loss upon heating corresponded to five water molecules per formula unit of $ZrO(NO_3)_2 \bullet xH_2O$ (Figure 4.1).

$CaCO_3$ was similarly investigated to ensure no absorbed water, but its mass loss only corresponded to the decomposition to CaO (Figure 4.1).

The synthesis proceeded by dissolving $ZrO(NO_3)_2 \bullet xH_2O$ and Sc_2O_3 in a 1:1 ratio of HNO_3 and H_2O by volume (pH was approximately -0.9) under reflux for approximately four hours. $CaCO_3$ was subsequently added resulting in an immediate reaction yielding gaseous CO_2.

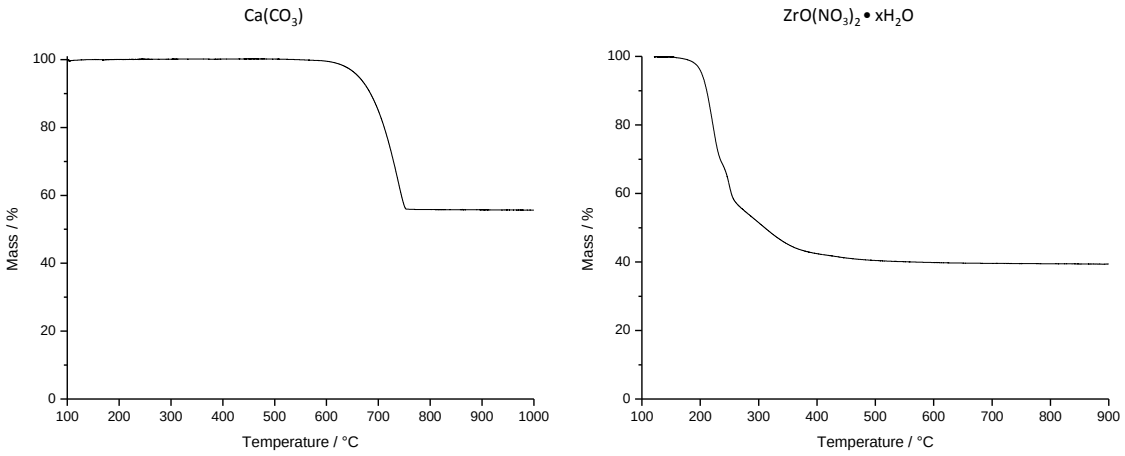

Figure 4.1: Thermogravimetric measurements of $CaCO_3$ (left) and $ZrO(NO_3)_2 \bullet xH_2O$ (right). These were both measured using the TG-DSC specified in section 4.5.

After all the reactants had dissolved, slightly more than three moles of citric acid were added for each mole of cations in order to ensure sufficient stability of the complex. This resulted in a clear solution. Upon bringing the solution to the boiling point of approximately 90 °C, the solution eventually got more viscous and a yellow tinge appeared, which became more prominent with time. To avoid decomposition of the complex, the solution was placed into a heating cupboard at 200 °C for 1 hour resulting in a porous and brown crust. The crust was crushed and fired at 450 °C for 12 hours to burn off all the organic materials. This caused a full decomposition of the citric acid and the resultant white inorganic precursor was calcined at 1200 °C for 12 hours.

4.1.3. Sintering

In order to prepare for electrical measurements of CSSc5 and CSSc10, pellets had to be sintered into dense samples for reliable results. However, due to the reported volatility of tin [86, 87], which may make the densification troublesome, different approaches were attempted. All pellets were packed in their own powder and covered with platinum foil to avoid evaporation.

Sintering in air was performed for CSSc5 at different temperatures and periods following work done by Azad et al. on the synthesis of nominally undoped $CaSnO_3$ [88]. However, the samples all gave unsuccessful densities as shown in Table 4.2.

Previous reports and experiences have shown that for some materials with volatile constituents, fast fire sintering can be used in order to yield dense samples without evaporating the constituents. For instance in $PbZrO_3$, PbO evaporates at relatively low temperatures but with some precautions samples obtained densities up to 92 % [89]. Such a procedure was attempted for CSSc10 with the following temperature program:

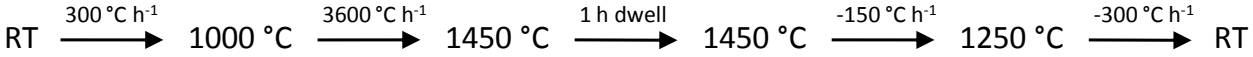

However, no major improvements in densities were found by employing this technique as samples only achieved 67 % of the theoretical density.

Improved sinterability has also often been attributed to using so-called sintering aids. Different reports have demonstrated that small additions of another oxide such as ZnO can lower the sintering temperature significantly, thus limiting evaporation of the tetravalent tin substantially [8, 17, 18, 83]. The disadvantage using this technique is the possibility of formation of secondary phases especially in the grain boundaries. Two separate 10 % Sc-doped $CaSnO_3$ samples with 1 and 2 mol % ZnO added as a substituent for Sn were used giving $CaSn_{0.89}Zn_{0.01}Sc_{0.1}O_{3-\delta}$ (CSZn1) and $CaSn_{0.88}Zn_{0.02}Sc_{0.1}O_{3-\delta}$ (CSZn2), respectively. This approach resulted in samples with densities reaching final values up to 94 % using the following temperature program:

The majority of information regarding the sintering procedures for Sc-doped $CaSnO_3$ is summarised below in Table 4.2.

Table 4.2: Various sintering procedures were attempted but only the use of sintering aids seemed to be successful.

Sample	Composition	Sintering temperature	Dwell / hours	Relative density	Note
CSSc5-1	$CaSn_{0.95}Sc_{0.05}O_{3-\delta}$	1350 °C	15	53%	Secondary phase present
CSSc5-2	$CaSn_{0.95}Sc_{0.05}O_{3-\delta}$	1200 °C	24	57%	-
CSSc5-3	$CaSn_{0.95}Sc_{0.05}O_{3-\delta}$	1300 °C	24	68%	-
CSSc5-4	$CaSn_{0.95}Sc_{0.05}O_{3-\delta}$	1300 °C	48	61%	-
CSSc10	$CaSn_{0.9}Sc_{0.1}O_{3-\delta}$	1450 °C	1	67%	Fast fire sintering
CSZn1	$CaSn_{0.89}Sc_{0.1}Zn_{0.01}O_{3-\delta}$	1350 °C	15	94%	Sintering aid
CSZn2	$CaSn_{0.88}Sc_{0.1}Zn_{0.02}O_{3-\delta}$	1350 °C	15	93%	Sintering aid

4.1.4. Electrodes

Prior to the electrical measurements, circular Pt mesh electrodes with 1 cm diameters were attached to each side of the pellets using Pt paint (Metalor A3788A). Three strokes were applied to each side and dried seperately for 30 minutes in a heating cupboard followed by annealing at 1000 °C for 1 hour in air.

4.2. Sample characterisation

4.2.1. X-ray diffraction (XRD)

XRD was used to study the composition of all samples after each calcination. The measurements were conducted using a Siemens D-5000 diffractometer operating in reflection geometry with a Cu $K_{\alpha 1}$ radiation source (λ = 1.5406 Å) in a 2θ-range of 3-90°. The diffraction data was processed using DIFFRAC^{plus} EVA, where the pattern was indexed and compared to a PDF (Powder Diffraction File) database developed by the ICDD (International Centre for Diffraction Data).

Examples of the XRD patterns are shown in Figure 4.2 CSSc5. It shows the subsequent calcinations done in the SSR synthesis of CSSc5 (900 °C, 5h + 3 × 1000 °C, 15 h). After four calcinations, the sample appeared to be single-phased as evidenced by the diminished peaks associated with the starting materials (CaO and SnO_2). A similar XRD pattern has been included for CZSc10 synthesised by SSR in Figure 4.3.

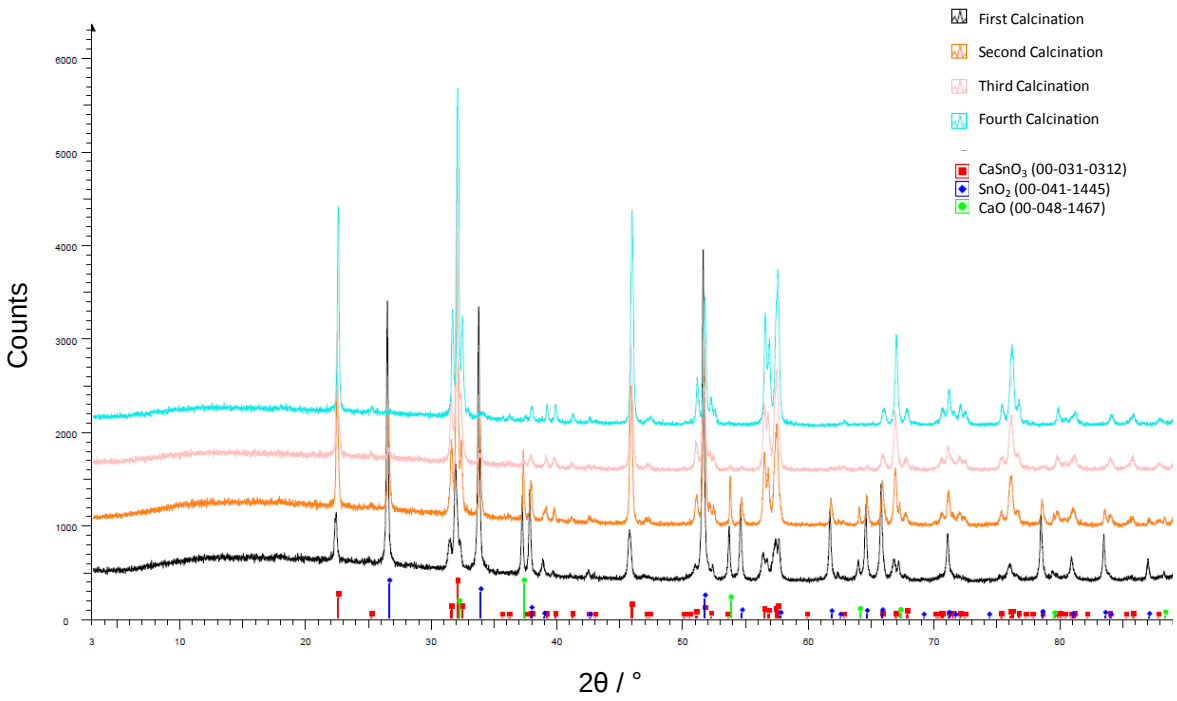

Figure 4.2: XRD patterns at room temperature of CSSc5 after each calcination. The synthesis method employed was SSR.

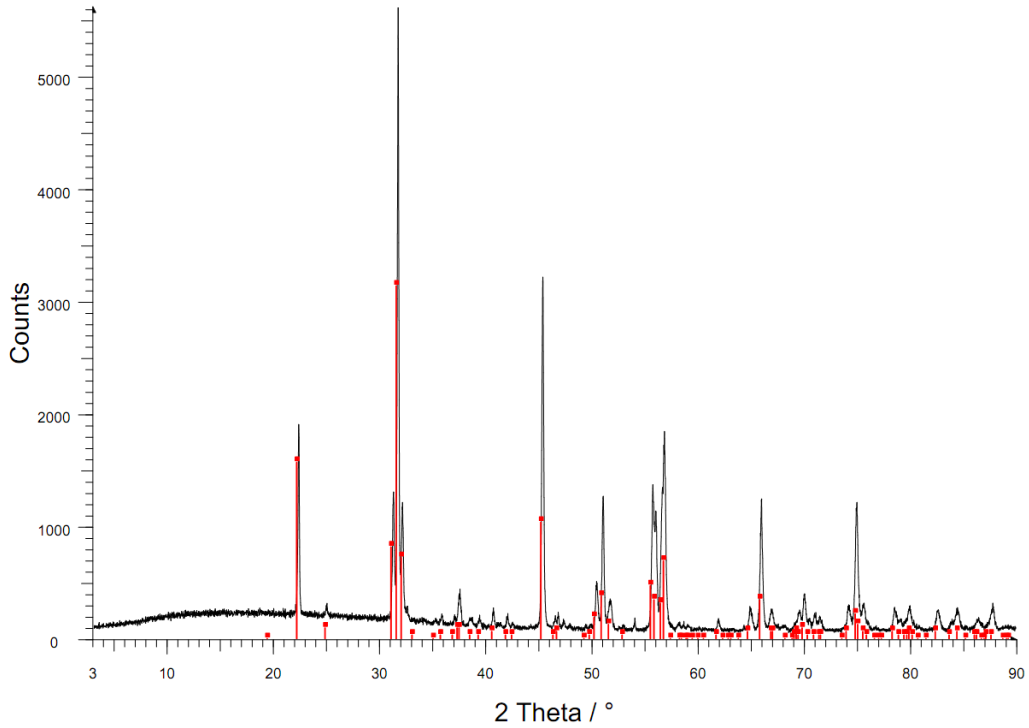

Figure 4.3: XRD pattern at room temperature of CZSc10. Synthesis method employed was SSR. A PDF of $CaZrO_3$ (01-076-2401) has been included for comparison.

4.2.2. Scanning electron microscopy (SEM)

SEM was used to study the microstructure and morphology of the samples after sintering. Additional EDS (Energy Dispersive X-ray Spectroscopy) was also used to study their composition. The measurements were conducted using a FEI Quanta 200 Field Emission Gun - Environmental SEM (FEG-ESEM) consisting of two detectors: an Everhart Thornley Detector (ETD) and a Solid State Detector (SSD). The instrument may additionally be operated under low vacuum by introducing a small amount of water vapour into the chamber.

4.3. Apparatus

4.3.1. Electrical measurement cell

Electrical characterisations of CSSc5 and CSZn1 were performed using a ProboStat measurement cell (NorECs AS, Norway) allowing high temperatures and a gas tight sample environment. The cell, as shown in Figure 4.4, consists of a long alumina support tube on which the sample is mounted. Two electrode contacts are connected to either side of the pellet, which are then held together by a spring load. The cell contains two gas inlets providing gas below and above the sample. This can be used for creating chemical potential gradients across the sample by introducing two different gaseous environments. The cell is sealed using an outer quartz tube and a rubber O-ring. For this thesis, measurements were conducted with the same gaseous environment on either side of the samples. The temperature was monitored and controlled using a S type Pt/Rh thermocouple and temperature controller.

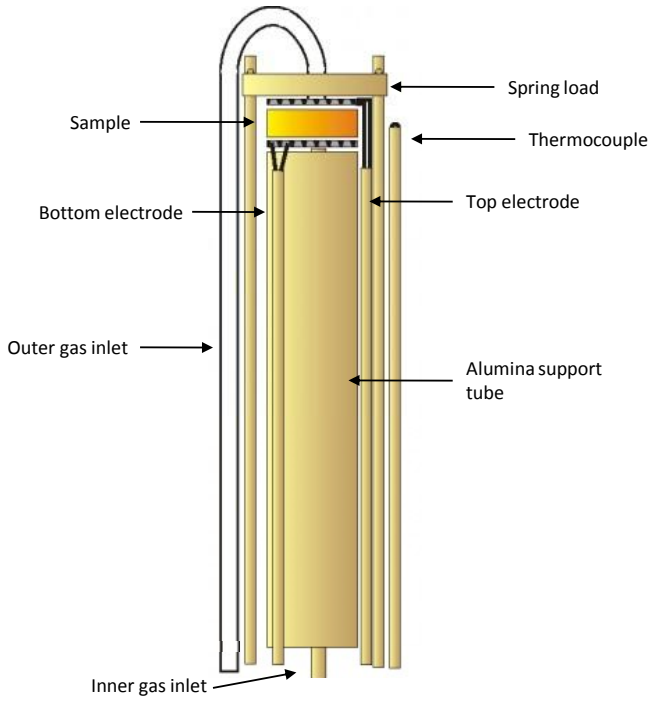

Figure 4.4: Schematic of the Probostat measuring cell used in this thesis. The outer quartz tube has been ommitted from the figure. Taken and modified from [90].

4.3.2. Gas mixer

The atmosphere in the measurement cell was controlled using an in-house built gas mixer depicted in Figure 4.5. As illustrated, the gas mixer consists of eight flowmeters (A-H) arranged pairwise to form four stages of mixtures M1-M4. An excess of each mixture is bubbled over columns of descending heights of dibutyl phtalate (B1-B4), which ensures a constant overpressure through the system. The first three stages serve to dilute O_2 (G1) with Ar (G2) giving an oxygen partial pressure range of 1 atm to 10^{-5} atm. Mixture 3 can subsequently be wetted by H_2O or D_2O via a wetting stage to form mixture 4. This is achieved by bubbling the gas through a saturated solution of KBr giving a p_{H_2O} of 0.03 atm (at 30 °C). This partial pressure is 80 % relative to using pure water and reduces the chance of water condensation in the copper tubes before the gas reaches the measurement cell. The gas from mixture 3 may similarly be dried through a drying stage consisting of P_2O_5. Due to gas leakages in the set-up, dry mixtures also contain a small amount of water estimated to give a p_{H_2O} of about 3×10^{-5} atm [91]. Intermediate water vapour pressures can be achieved by mixing wet and dry portions of the gas.

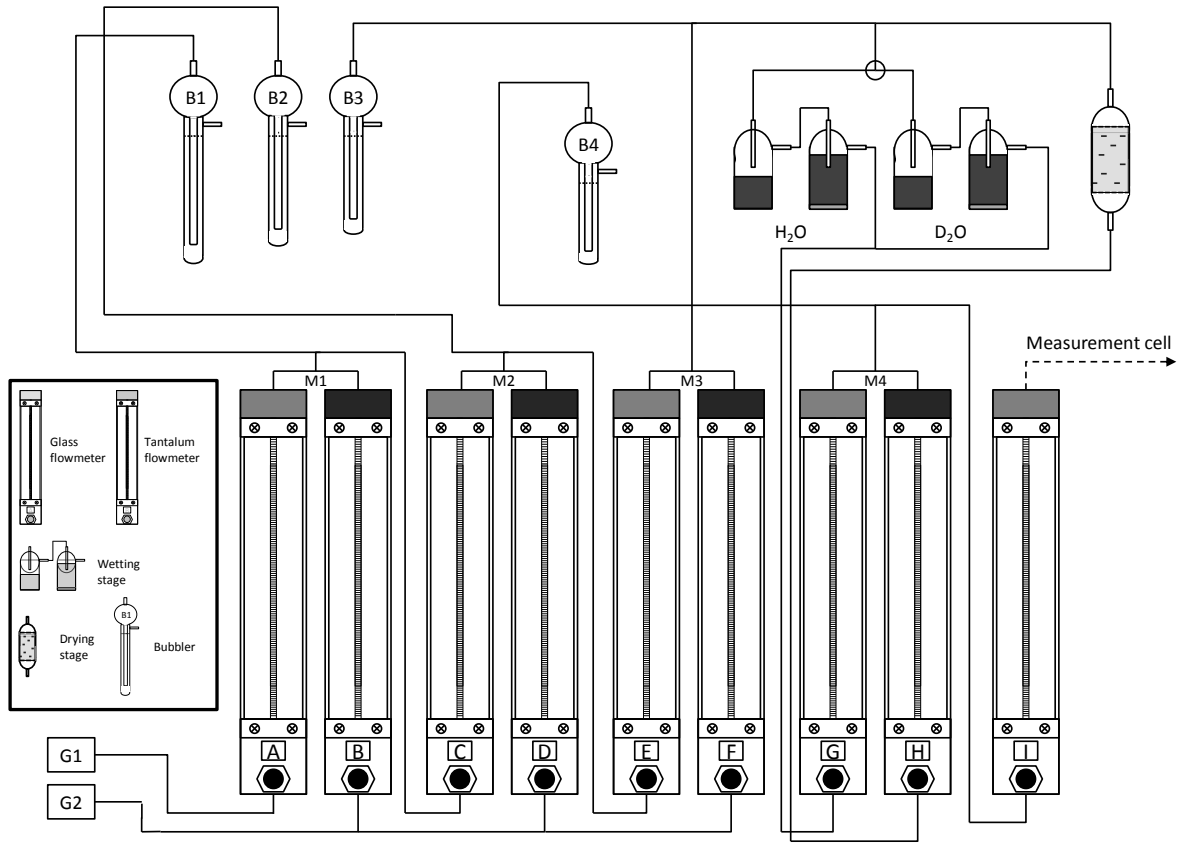

Figure 4.5: Sketch of the gas mixer used in this thesis. G1 and G2 were O_2 and Ar, respectively.

4.4. Electrical measurements

The electrical measurements were conducted using a 2-point 4-wire set-up on two different impedance spectrometers. The first of which was a *HP4192A LF, Impedance Analyzer* with a frequency operating range of 5 Hz – 13 MHz. Its oscillation voltage may be varied between 0 and 1.1 V. This instrument was only used for total conductivity measurements of CSSc5 at a constant frequency of 10 kHz and an oscillation voltage of 1 V. The instrument has an input impedance of 1 MΩ and can thus measure impedances from 0.1 mΩ to 1.3 MΩ. The instrument's accuracy within this range is reported to be within 0.1 % with some larger discrepancies in the low frequency range.

The other instrument used was a *Novocontrol Alpha-AN*. This instrument has an operating frequency range of 3 μHz to 20 MHz. It has an input impedance of 1 TΩ allowing impedance measurements from 10 mΩ to 200 TΩ [92]. The accuracy within this window is reported to be within 0.03 %.

The specific conductivities of the samples were corrected for porosity using the empirical equation:

$$\sigma_s = \frac{\sigma_m}{(1 - v_p)^2} \qquad \textbf{Equation 4.2}$$

where σ_s and σ_m are the specific and measured conductivities, respectively, while v_p is the volume fraction of pores in the samples. Relatively large uncertainties of about 20 % are involved in using Equation 4.2 to estimate σ_s [93]. However, only small improvements may be made using more detailed knowledge regarding the sample's microstructure.

4.5. TG-DSC measurements

For measuring the molar hydration enthalpy directly, *in-situ* combined TG-DSC measurements were conducted. The instrument used was a Netzsch STA (Simultaneous Thermal Analyzer) 449 C Jupiter equipped with a water vapour generator. It is designed to operate under high water vapour pressures using a high water vapour furnace. Water is completely evaporated at 180 °C internally in the vapour generator and introduced to the furnace by a heater transfer line and heating jacket, excluding condensation. Before reaching the sample, the water vapour is preheated to the sample temperature inside the outer flow chamber and guided from the top as indicated in the Figure 4.6. The water vapour pressure may be varied by diluting with N_2 using a purge gas channel controlled by a mass flow controller. The diluting N_2 gas may also be introduced within the water vapour generator directly controlled by a needle valve, but previous work by Kjølseth [94] has found this to give a lower stability. Only the purge gas channel was used to dilute the water vapour in this thesis.

It should be noted that the water vapour pressure of the diluting N_2 gas was not controlled. However, due to the high water vapour pressures being operated with, the uncertainty associated with this is assumed to be negligible. The diluting gas is thus assumed to be dry.

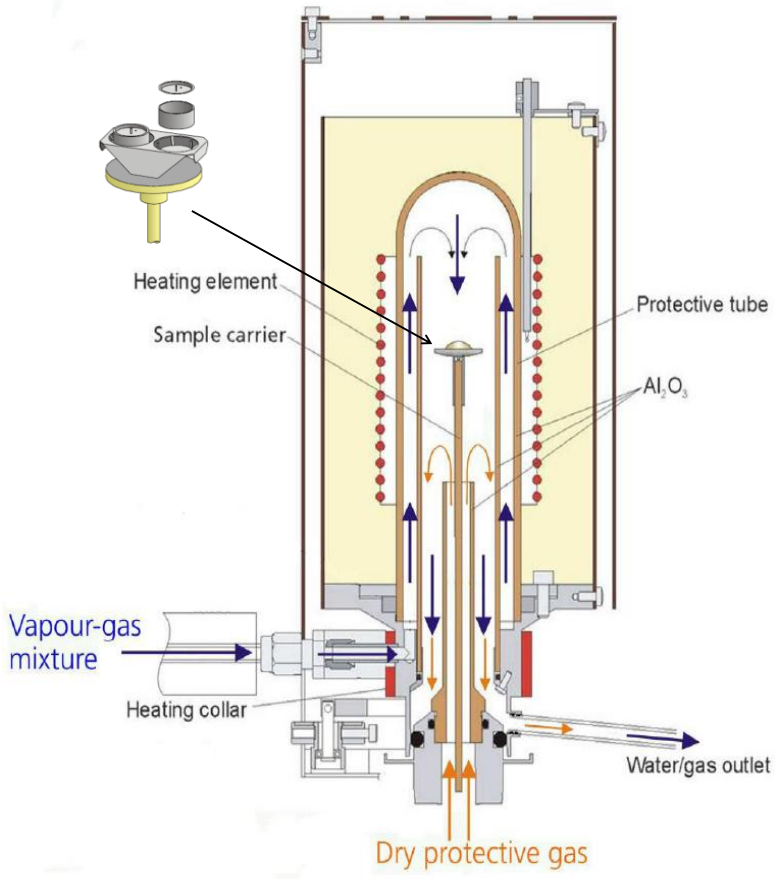

Figure 4.6: Schematic of the TG-DSC instrument used to in this thesis. Taken from [95].

The mass, temperature and DSC sensitivity of the instrument were calibrated prior to measurements. The mass calibration was performed using a built-in calibration procedure. A well-defined mass of 2.0000 g was put on the balance and compared with the nominal value stored internally in the instrument. For the temperature and the DSC sensitivity calibration, measurements were conducted and compared to known phase transitions in six different materials provided by Netzsch [96]. Summarised information regarding the materials used can be found in Table 4.3 along with the appropriate references.

Table 4.3: Details regarding the materials used to calibrate the TG-DSC for temperature and sensitivity. The information was taken from the Netzsch Jupiter 449 C manual.

Material	Type of transition	Temperature / °C	Enthalpy / J g^{-1}	Reference
$RbNO_3$	Trigonal to cubic	164.2	26.6	[97]
$KClO_4$	Orthorhombic to cubic	300.8	104.9	[97]
Ag_2SO_4	Hexagonal to orthorhombic	426.4	51.7	[98]
CsCl	Bcc cubic to fcc cubic	476.0	17.22	[98]
K_2CrO_4	Hexagonal to orthorhombic	668	38.9	[99]
$BaCO_3$	Orthorhombic to trigonal	810	94.9	[100]

A typical calibration measurement would use two Pt/Rh crucibles; one with the sample material and one empty reference crucible. They would then be heated and cooled with rates of 10 K min^{-1} under flowing nitrogen in the range of interest, i.e. around the temperature of the phase transitions. An example of CsCl has been included in Figure 4.7 and shows three heating and cooling cycles. An average of the onset temperature values and integrals of the peaks were calculated for the two latter heating curves yielding values for temperature and DSC sensitivity, respectively. These were then fitted to an internal calibration curve in the Netzsch Proteus program [101]. The polynomials used for the fitting of temperature and DSC sensitivity were:

$$A = 10^{-3}B_0 + 10^{-5}B_1T_{exp} + 10^{-8}B_2{T_{exp}}^2 \qquad \textbf{Equation 4.3}$$

$$C = \left[D_2 + D_3\left(\frac{T-D_0}{D_1}\right) + D_4\left(\frac{T-D_0}{D_1}\right)^2 + D_5\left(\frac{T-D_0}{D_1}\right)^3\right]\exp\left(\frac{D_0-T}{D_1}\right)^2 \qquad \textbf{Equation 4.4}$$

The fitting of the calibration points for temperature and DSC sensitivity are given in Figure 4.8 and Figure 4.9. These calibration files were loaded into the instrument's software prior to measurements. Netzsch reports the accuracy to be within 3 % for the enthalpy evaluations [101].

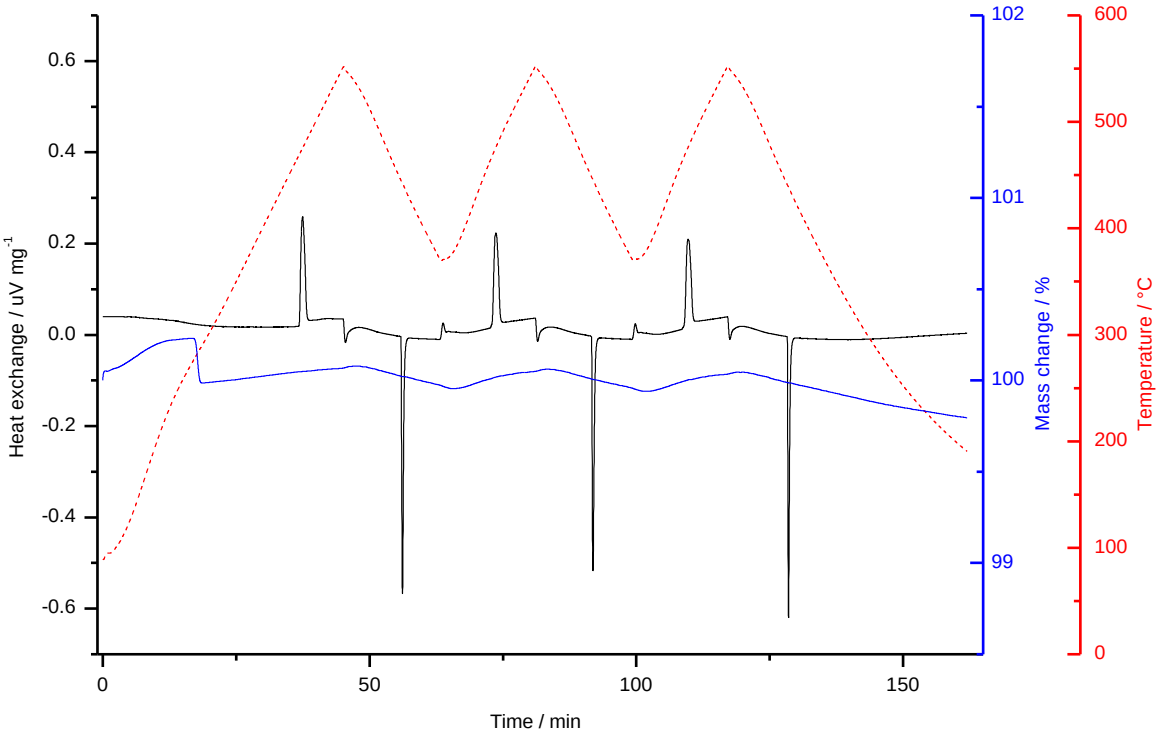

Figure 4.7: Calibration measurement of CsCl. An average of the onset temperatures and the endothermic peak integrals were used as values for the calibration. Only the second and third heating segments were used.

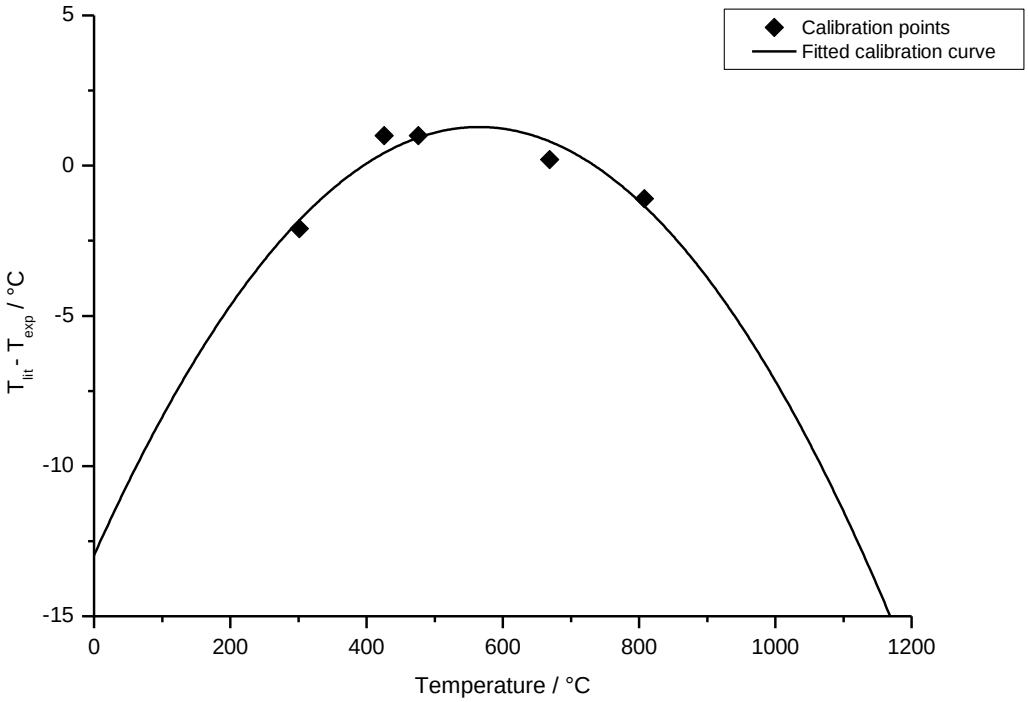

Figure 4.8: Temperature calibration curve used for all TG-DSC measurements.

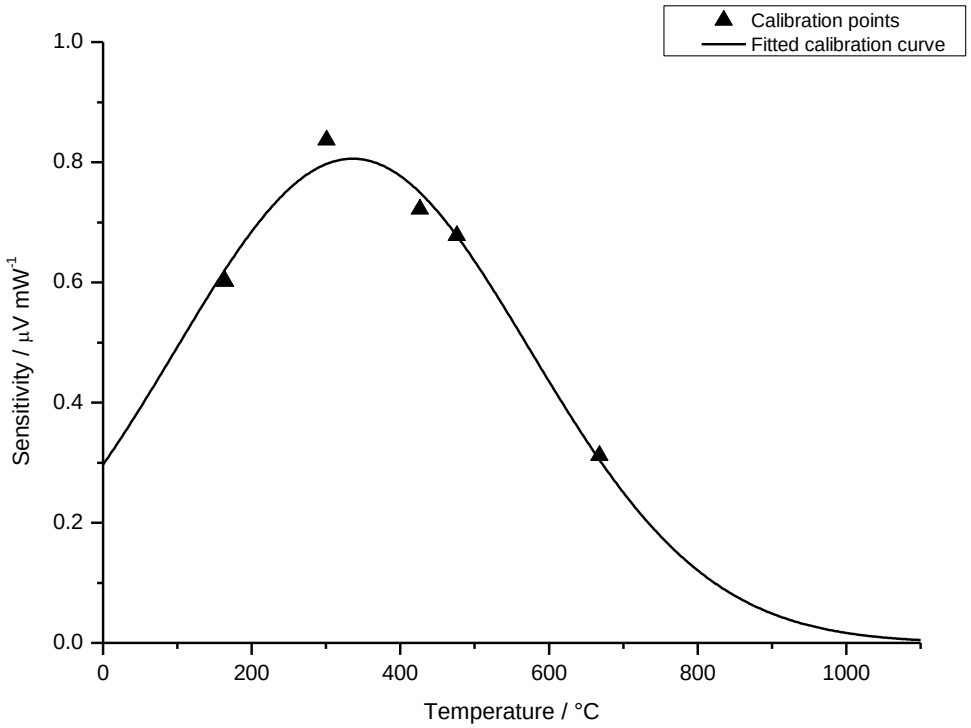

Figure 4.9: DSC sensitivity calibration curve used for all TG-DSC measurements.

A typical TG-DSC measurement would consist of seven steps:

1) Heating to desired temperature (e.g. 500 °C) by 20 K min^{-1} under flowing N_2 (g).
2) Isothermal dwell at 500 °C under flowing N_2 (g) for 30 minutes.
3) First hydration: Isothermal dwell at 500 °C under flowing H_2O (g) for 15 minutes.
4) First dehydration: Isothermal dwell at 500 °C under flowing N_2 (g) for 45 minutes.
5) Second hydration: Isothermal dwell at 500 °C under flowing H_2O (g) for 15 minutes.
6) Second dehydration: Isothermal dwell at 500 °C under flowing N_2 (g) for 45 minutes.
7) Cooling to room temperature by 20 K min^{-1} under flowing N_2 (g).

Gas flows of N_2 (g) and H_2O (g) were 20 ml min^{-1} from the protective gas channel and 150 ml min^{-1} from the heating collar, respectively (Figure 4.6). This corresponded to a rapid change from 1 atm N_2 (g) to 1 atm H_2O (g). All measurements were additionally corrected with a background where both the sample and reference crucibles were empty. Investigations using other backgrounds were made with nominally undoped $CaZrO_3$ (synthesised by SSR using the same procedure discussed in section 4.1.1) and Yttria-stabilised zirconia (8YSZ, TOSOH, Japan) due to their reported negligible water uptakes. However, no major improvements were found and measurements were therefore consistently conducted using an empty reference crucible. Backgrounds were similarly measured using two empty crucibles.

The isothermal steps in a typical sample and background measurement are shown in Figure 4.10 for CZSc20. In the TG signal, the apparent relative weight changes for both the sample and the background upon changing the gas in the reaction chamber. For the background, this weight increase can be ascribed to a change in the buoyancy upon going from the heavier N_2 (g) to H_2O (g) and is in accordance with backgrounds measured by Kjølseth et al. [7]. When correcting for this buoyancy, the resulting mass increase reflects in principle the water incorporation of the sample. The DSC signal shows distinct differences between the background and sample measurements. The background exhibits a small signal difference, which might correspond to a difference in the thermal conductivities of the gases. In the sample curve, there is a clear exothermic peak occurring upon changing from N_2 (g) to H_2O (g). The signal for the dehydration segments are far less prominent but can still be used for interpretation giving results in the same range as the ones obtained for hydration. It should be noted that the DSC curve for the background differs from Kjølseth's measurements conducted using the same instrument. This was only observed after changing the sample holder and might suggest the existence of a small temperature difference inside the sample chamber. There is also a shift in the DSC signal's baseline after hydration, which has been suggested to be due to the difference in thermal conductivity of the dehydrated and hydrated sample.

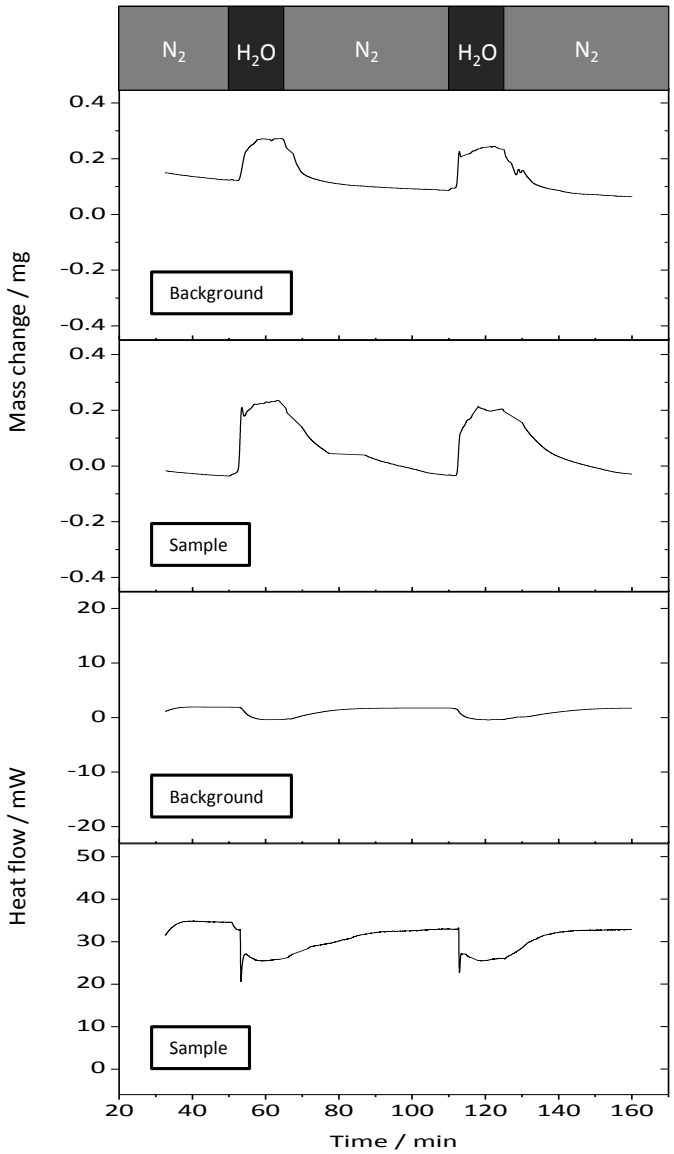

Figure 4.10: Typical sample and background TG-DSC measurements. These were conducted at 500 °C. The sample and background used were CZSc20 and an empty crucible, respectively. The heating and cooling segments have been omitted for clarity.

TG-DSC measurements were conducted at different temperatures (500 - 900 °C) and p_{H_2O} (0.1 – 1 atm). All measurement files were subtracted by a suitable background file. The enthalpies were then calculated by evaluating the integral in the DSC signal peak using the in-built software of Netzsch Proteus. Correspondingly, the mass change was also evaluated yielding the standard molar hydration enthalpies directly. Due to a shift in the baseline, a step function was used to evaluate the area as it is reported to give the best approximation compared to a sigmoidal and linear function [94].

4.6. Thermogravimetric measurements

Thermogravimetric measurements were conducted using a Netzsch 449 F1 instrument in order to model the uptake of water as a function of temperature. The gas atmosphere was controlled and introduced using a small gas-mixer (smaller version of the one depicted in Figure 4.5). Measurements were conducted in wet He and wet H_2 + He (8 and 90 %, respectively) where $p_{H_2O} = 0.02$ atm. These will from hereon be referred to as inert and reducing conditions for the thermogravimetric measurements. Samples were placed in alumina crucibles and ramped and dwelled as shown in Figure 4.11. The gas atmosphere was kept constant during each measurement.

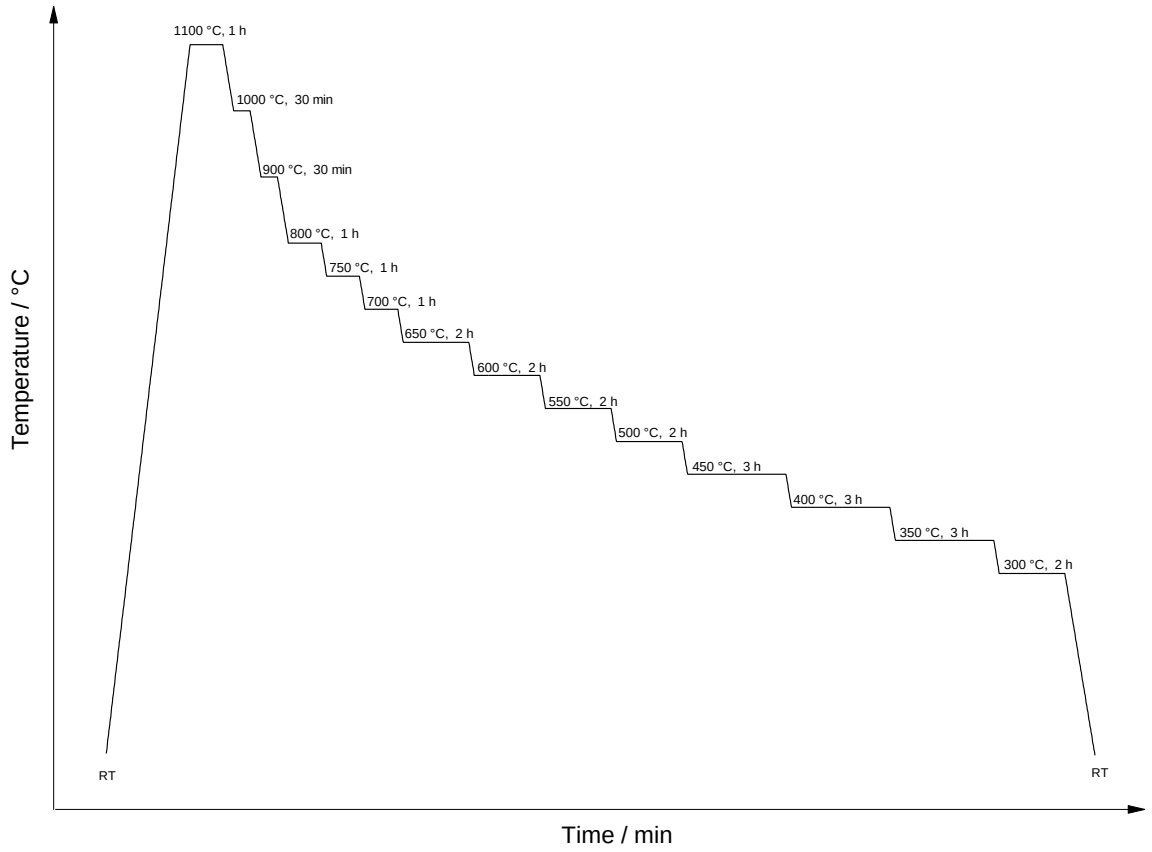

Figure 4.11: Temperature profile used for all thermogravimetric measurements. Heating and cooling segments were ramped at 7 and 5 K min^{-1}, respectively.

4.7. Uncertainties and sources of error

It is difficult to ascertain the extent of all uncertainties and sources of error. However, it is important to be aware of the errors that are present in order to possibly avoid or reduce them.

Large uncertainties of up to 60 % can be associated with the flow meters used in the gas mixers when using flows lower than 20 mm. These uncertainties may however be significantly minimised to around 5 % by adjusting the flows to above 60 mm in the set-up [102].

Any mixer will to some extent exhibit leakages, which will of course influence the gas composition introduced to the sample. As previously mentioned, a dry gas will have a water content of about 30 ppm as estimated by Kofstad and Norby [91] while there is also a small discrepancy in estimating the oxygen partial pressure from the argon gas cylinder. This will therefore mean that the calculated partial pressure in an experiment might deviate from its exact value.

Compositions of all samples studied in this thesis were found using XRD and EDS. However, these have associated uncertainties of 3 weight per cent and 1-2 atomic per cent respectively. Small amounts of impurities and secondary phases may therefore still be present. SEM micrographs showed no indication of any secondary phases and all samples seemed chemically homogeneous thereby supporting the compositional findings done by XRD and EDS.

For a higher degree of reproducibility in the TG-DSC results, masses and hydration peak integrals were calculated five times for every single measurement to obtain reliable hydration enthalpies. This is shown in Figure 4.12 for the TG signal as small variations in the position of the cursor in the software (Netzsch Proteus) may alter the mass uptake quite substantially. Five arbitrary points were therefore used before and after hydrating the samples for both the TG and DSC signal allowing a statistical mean and standard deviation to be evaluated. Several experimental runs were also employed in order to reduce the uncertainties as well as providing reproducible results. Netzsch reports an uncertainty of 3 %, but this was not taken into account as it constituted a minor difference.

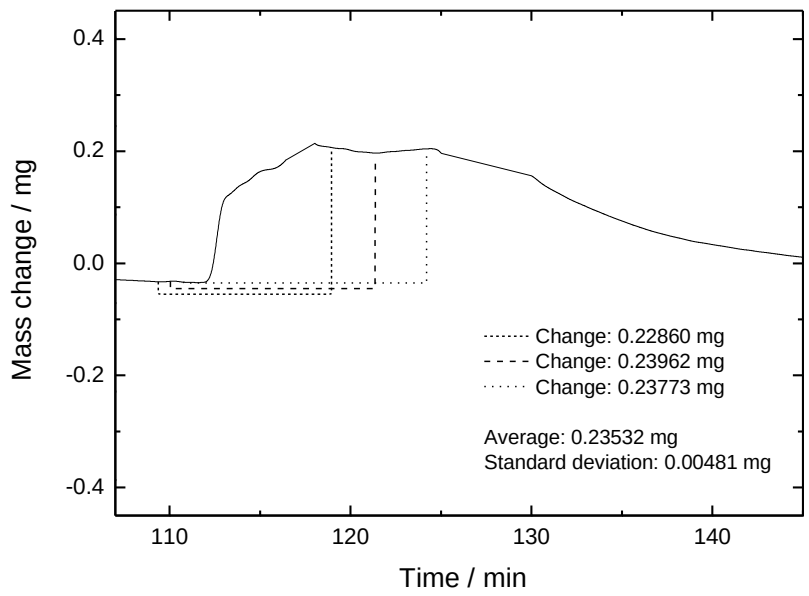

Figure 4.12: TG signal from a TG-DSC measurement demonstrating how the cursor position in the software can alter the resulting mass uptake used in the hydration enthalpy calculations.

As the thermocouple may not always be situated directly next to the sample while conducting measurements, small deviations in the temperatures may also be encountered. In order to reduce the significance of such deviations, the TG-DSC and TG were calibrated for temperature as discussed in section 4.5.

Smaller errors may also be encountered during weighing as the analytical balance used has an uncertainty of ± 0.05 mg. However, these errors are almost completely negligible as they never constitute uncertainties that are larger than 0.7 % for all measurements.

5. Results

In this section, the results from the materials characterisation of $CaSn_{1-x}Sc_xO_{3-\delta}$ (CSSc) and $CaZr_{1-x}Sc_xO_{3-\delta}$ (CZSc) will be presented with emphasis on XRD and SEM. This will be followed by the thermodynamic measurements on both materials with emphasis on TG-DSC. The final section will be focused on the electrical characterisation of the CSSc samples where impedance spectroscopy has been the primary tool.

5.1. Sample characterisation

5.1.1. Effect of calcination temperature on $CaSn_{0.95}Sc_{0.05}O_{3-\delta}$ (CSSc5)

The syntheses of CSSc5 were troubled by formation of secondary phases of Ca_2SnO_4 upon calcination and sintering at temperatures exceeding 1100 °C presumabely due to the reported evaporation of tin. Figure 5.1 shows the XRD patterns for a CSSc5 sample that was calcined at 1100 °C for 15 hours. Peaks corresponding to the (110) and (020) planes in Ca_2SnO_4 are marked and displayed in Figure 5.2. The figures give evidence for tin evaporation as the patterns indicate a larger proportion of Ca_2SnO_4 with prolonged heat treatment at this temperature. Higher temperatures correspondingly amounted to a larger evaporation of tin. Syntheses of Sc-doped $CaSnO_3$ samples were therefore carried out at temperatures below 1100 °C.

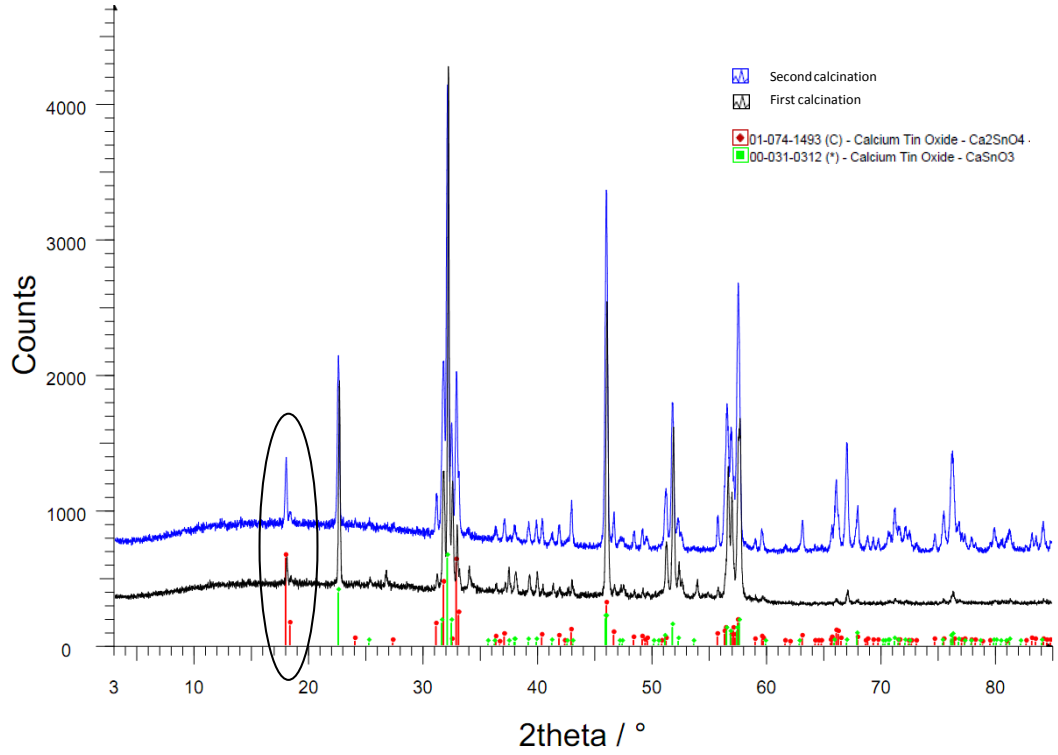

Figure 5.1: XRD patterns measured at room temperature of a CSSc5 sample calcined once and twice at 1100 °C for 15 hours. Marked region is shown in Figure 5.2. Patterns corresponding to the starting materials (CaO and SnO_2) have not been included for clarity.

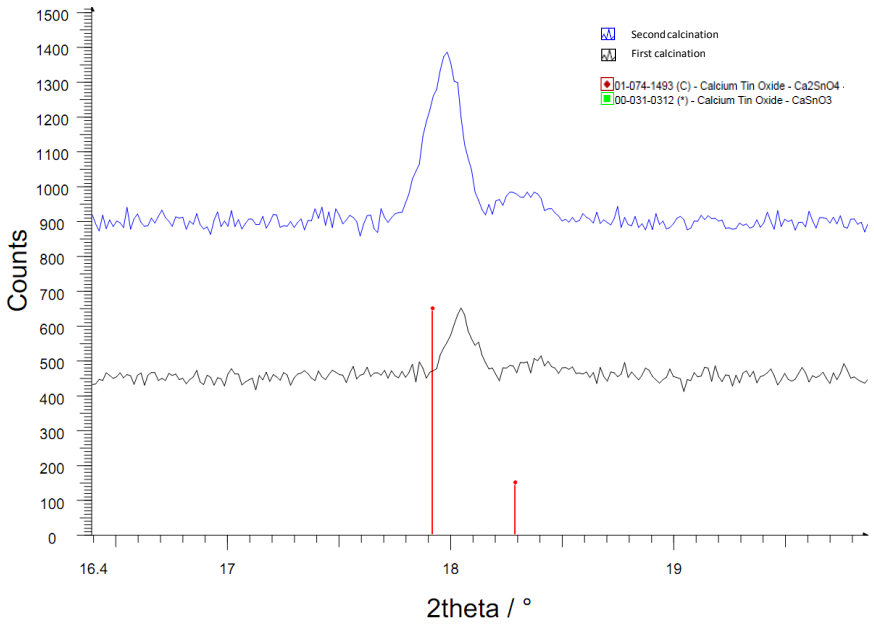

Figure 5.2: Marked region of the XRD pattern shown in Figure 5.1. The peaks correspond to (110) and (020) planes in Ca_2SnO_4.

5.1.2. Effect of sintering aid on the microstructure of CSSc

Due to poor densification upon sintering, small amounts of ZnO were added to increase the sinterability of CSSc5. Micrographs of samples of CSSc10 with ZnO and CSSc5 are displayed in Figure 5.3 and Figure 5.4, respectively. As indicated, ZnO addition increased the relative densities from 57-68 % to 93-94 % of the sintered samples. All micrographs were typical for the microstructure of the samples and no secondary phases were observed. The micrographs further indicate a homogeneous grain size distribution, with diameters ranging from 0.1 to 1 μm. A small increase in the grain sizes upon increasing the sintering temperature from 1200 to 1300 °C was observed (see Figure 5.4).

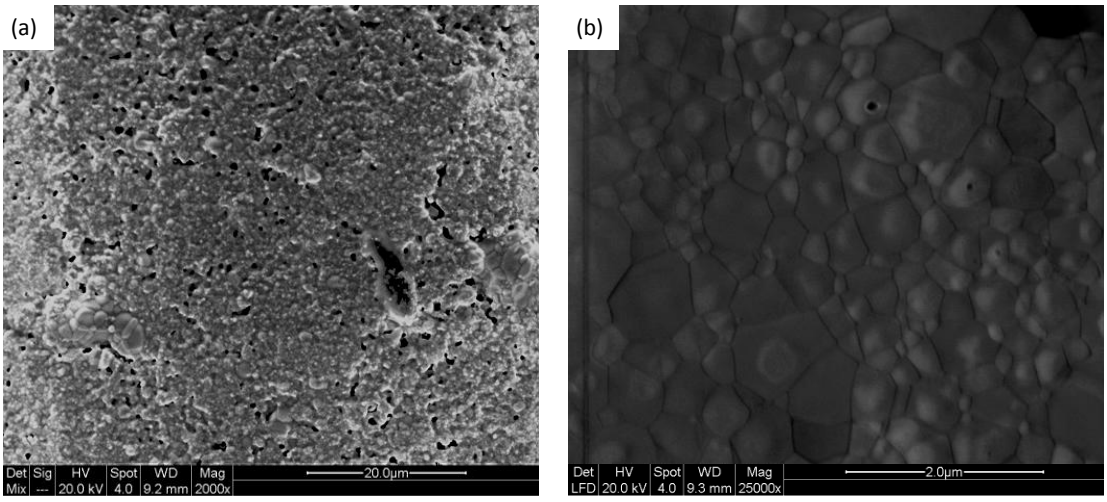

Figure 5.3: Scanning electron micrographs of CSZn2 under low vacuum with different magnifications. (a) is recorded with signals from both the LFD and SSD while (b) only exhibits the signal from the LFD.

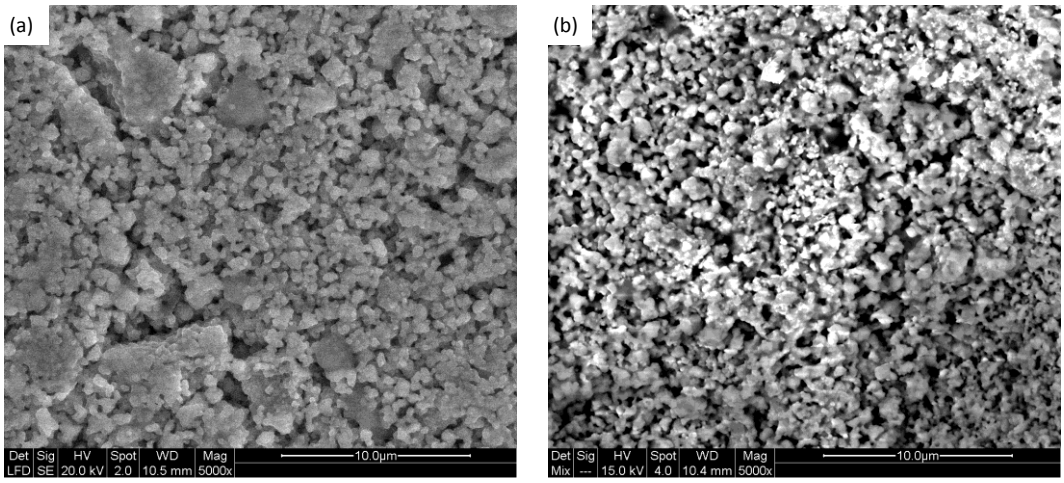

Figure 5.4: Scanning electron micrographs of CSSc5 sintered at 1300 (a) and 1200 °C (b) under low vacuum. (a) is recorded with signals from the LFD while (b) used the signals from both the LFD and SSD.

Table 5.1 summarises the atomic compositions of the grains as obtained using the EDS detector. The measured compositions of all samples were close to the nominal compositions and no indication of Ca_2SnO_4 was detected.

Table 5.1: Atomic percentages of the different elements from three spot analyses of CSZn2 using EDS. The expected percentages are also included.

Element	Scan 1	Scan 2	Scan 3	Average	Expected
Ca	49.54	50.08	49.38	49.67	50
Sn	44.55	44.72	44.35	44.54	44
Sc	4.96	4.56	5.12	4.88	5
Zn	0.94	0.64	1.15	0.91	1

5.2. TG-DSC results of CZSc

5.2.1. Hydration thermodynamics as a function of acceptor concentration

TG-DSC was used to investigate the standard molar hydration enthalpies of $CaZr_{1-x}Sc_xO_{3-\delta}$ (CZSc) with different levels of Sc substitution. Figure 5.5 displays the DSC hydration peak intensities of CZSc with varying levels of Sc dopant while Figure 5.6 shows the corresponding enthalpy change upon hydration. As indicated, the peak intensity increases in correspondence with the increasingly negative hydration enthalpies suggesting a correlation to the amount of incorporated protons.

The increased uncertainty in the evaluated values from 500 to 600 °C can be explained by the fact that the water uptake is lower at 600 °C thus increasing the uncertainty in the mesasured heat evolution and mass change.

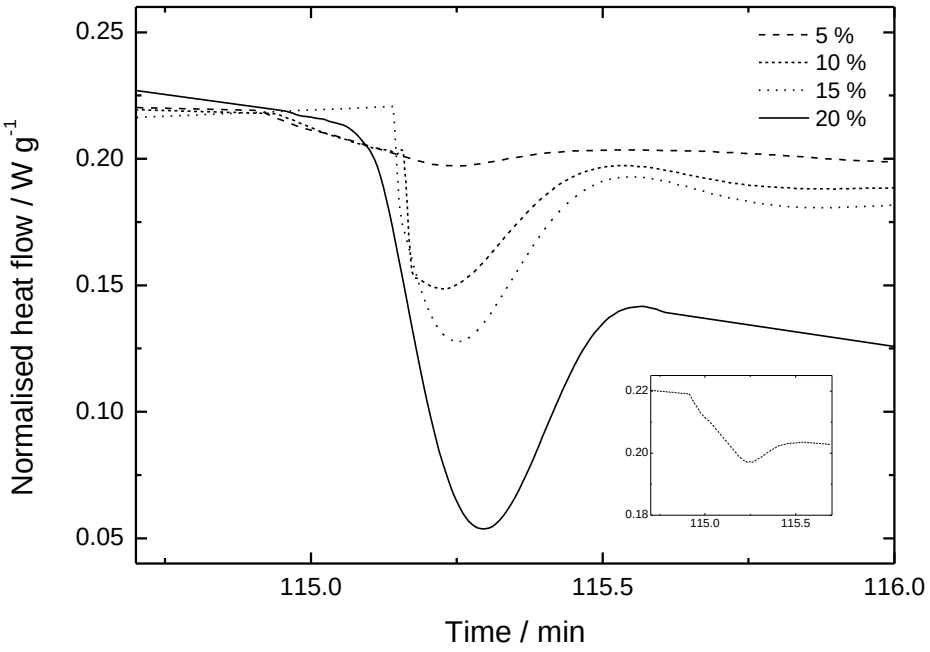

Figure 5.5: DSC hydration peaks as a function of Sc substitution measured at 600 °C. Inset shows hydration peak for CSSc5.

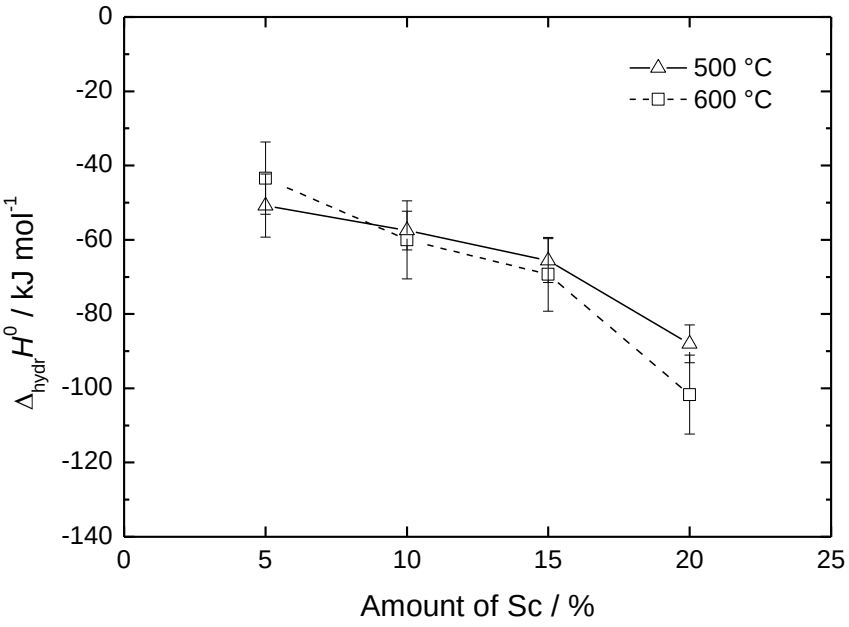

Figure 5.6: Standard molar hydration enthalpies as a function of Sc substitution in CZSc measured by TG-DSC at 500 and 600 °C.

Using the mass uptake associated with the hydration reaction of oxygen vacancies, the equlibrium constant has been calculated allowing an indirect calculation of the standard molar hydration entropy for each individual measurement through:

$$\mathrm{K_{hydr}} = \frac{[\mathrm{OH_O^{\bullet}}]^2}{[\mathrm{v_O^{\bullet\bullet}}][\mathrm{O_O^X}]p_{\mathrm{H_2O}}} = \exp\left(-\frac{\Delta_{\mathrm{hydr}}H^0}{\mathrm{RT}}\right)\exp\left(\frac{\Delta_{\mathrm{hydr}}S^0}{\mathrm{R}}\right) \qquad \textbf{Equation 5.1}$$

This assumes that the hydration reaction of the sample has reached its thermodynamic equilibrium during the hydration steps in the TG-DSC measurements. The different trends for the values evaluated at 500 and 600 °C may reflect an incorrect assumption.

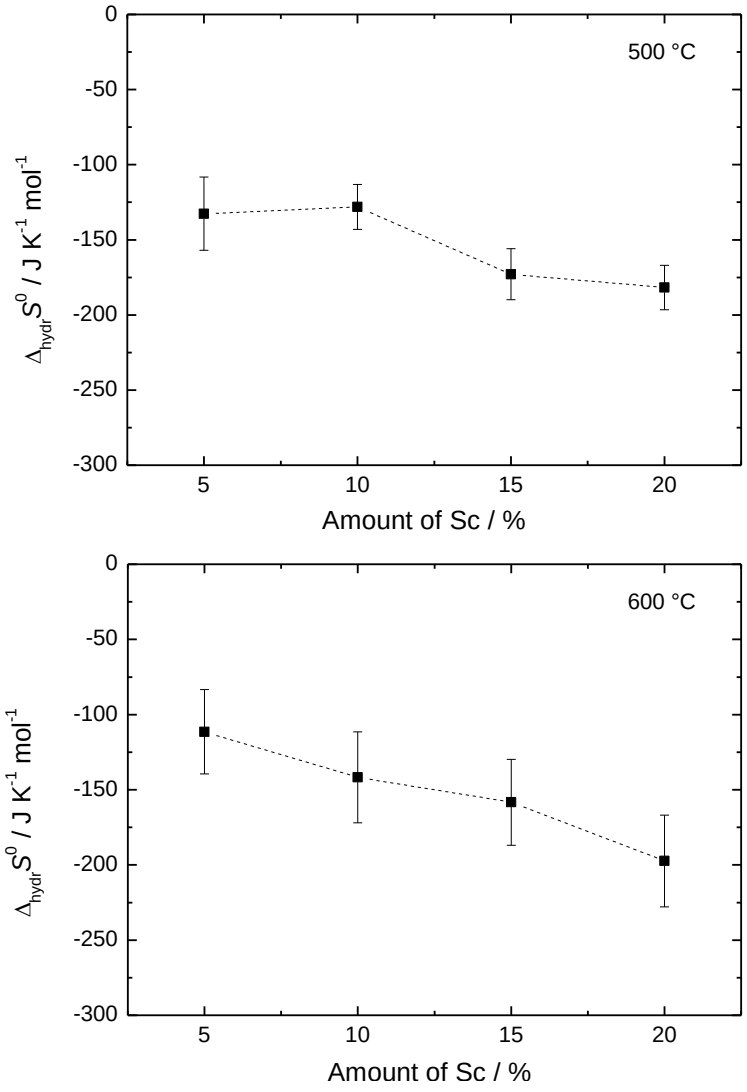

Figure 5.7: Standard molar hydration entropies for CZSc indirectly evaluated using TG-DSC at 500 °C (top) and 600 °C (bottom).

5.2.2. Hydration thermodynamics as a function of temperature

As a difference in the evaluated enthalpies and entropies was observed for the measurements conducted at 500 °C and 600 °C, the standard molar hydration enthalpy and entropy of CZSc20 was measured as a function of temperature (500-900 °C). Figure 5.8 shows how the DSC hydration peak intensities vary with temperature. These indicate that both thermodynamics and kinetics play a role in the TG-DSC experiments conducted. The decrease in intensity from 500 to 600 °C may be explained with respect to the unfavourable thermodynamics while the increase from 600 to 800 °C may be due to more favourable hydration kinetics. The final decrease in intensity between 800 and 900 °C can again be related to the less favourable thermodynamics. The corresponding hydration enthalpies and entropies are displayed in Figure 5.9 and Figure 5.10, respectively. Although the intensities vary somewhat with temperature, the enthalpies and entropies are reasonably temperature independent with an average value of -93 ± 3 kJ mol^{-1} and -182 ± 21 J K^{-1} mol^{-1}, respectively. All evaluated values are within the uncertainties of the measurements. These findings suggest that the thermodynamics are independent of the degree of hydration in accordance with previous work by Kjølseth [94].

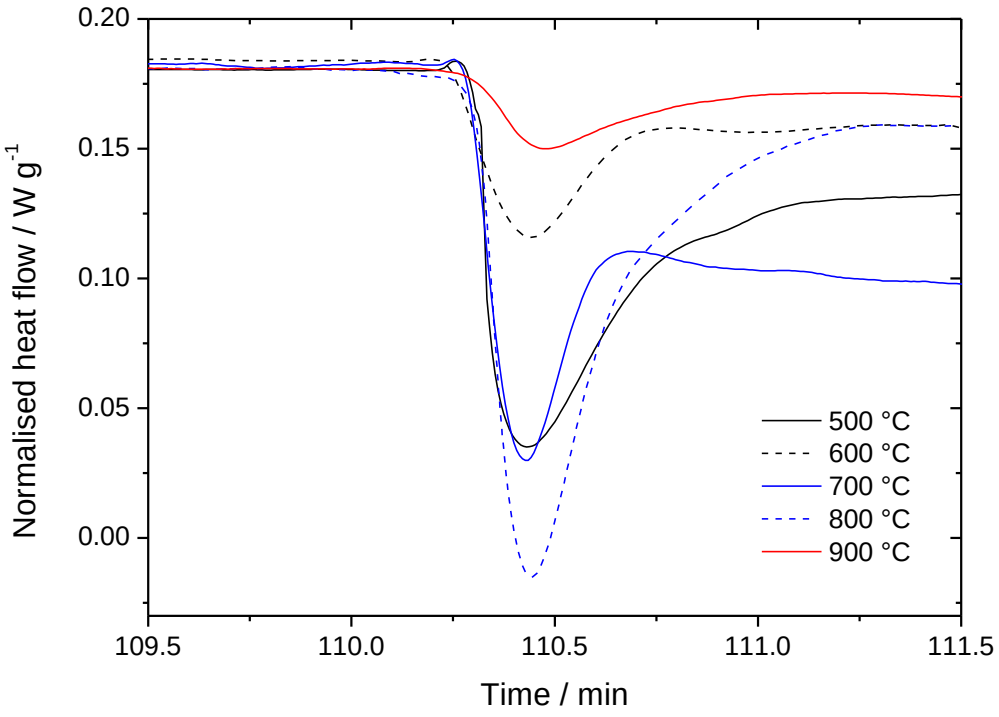

Figure 5.8: DSC hydration peaks as a function of temperature for CZSc20.

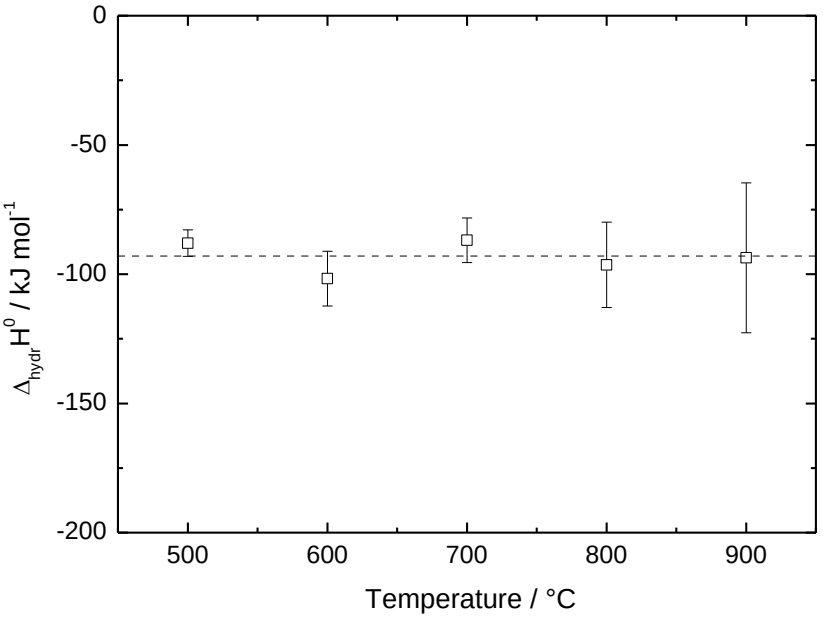

Figure 5.9: Standard molar hydration enthalpies determined for CZSc20 as a function of temperature measured by TG-DSC.

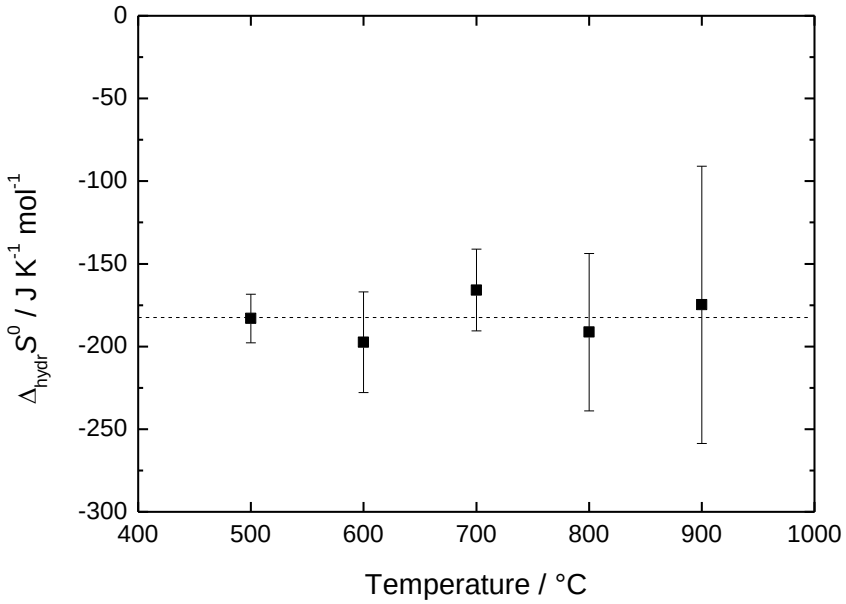

Figure 5.10: Standard molar hydration entropies determined indirectly for CZSc20 as a function of temperature using TG-DSC.

5.2.3. Hydration thermodynamics as a function of p_{H_2O}

In order to verify that the hydration thermodynamics are independent of the degree of hydration, values were evaluated as function of p_{H_2O} for CZSc20.

Figure 5.11 shows how the DSC hydration peak intensities vary with p_{H_2O}. It displays an increasing intensity with increasing p_{H_2O} , thus indicating a correlation to the amount of absorbed protons. The intensity decreases from 0.1-0.2 atm and more noticeably from 0.8-0.9 atm, but this is believed to be due to experimental discrepancies.

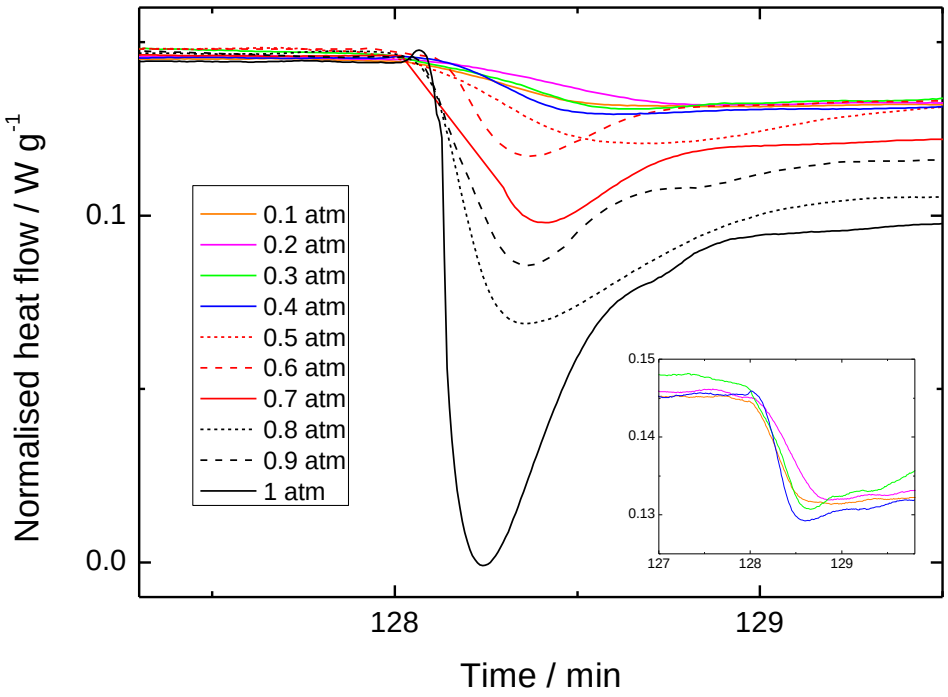

Figure 5.11: DSC hydration peaks as a function of p_{H_2O} for CZSc20 at 500 °C.

The resulting hydration enthalpies and entropies are summarised in Figure 5.12 and Figure 5.13, respectively. These indicate similarly to the temperature dependency experiments that the hydration thermodynamics of CZSc20 are independent of the degree of hydration. The evaluated enthalpy (-85 ± 7 kJ mol^{-1}) and entropy (-187 ± 21 J K^{-1} mol^{-1}) are also in agreeement with the average value evaluated from the temperature dependencies. The larger uncertainties associated with the measurements conducted at lower partial pressures of water vapour is again linked to a lower water uptake as evidenced from the decreasing peak intensity with decreasing p_{H_2O}.

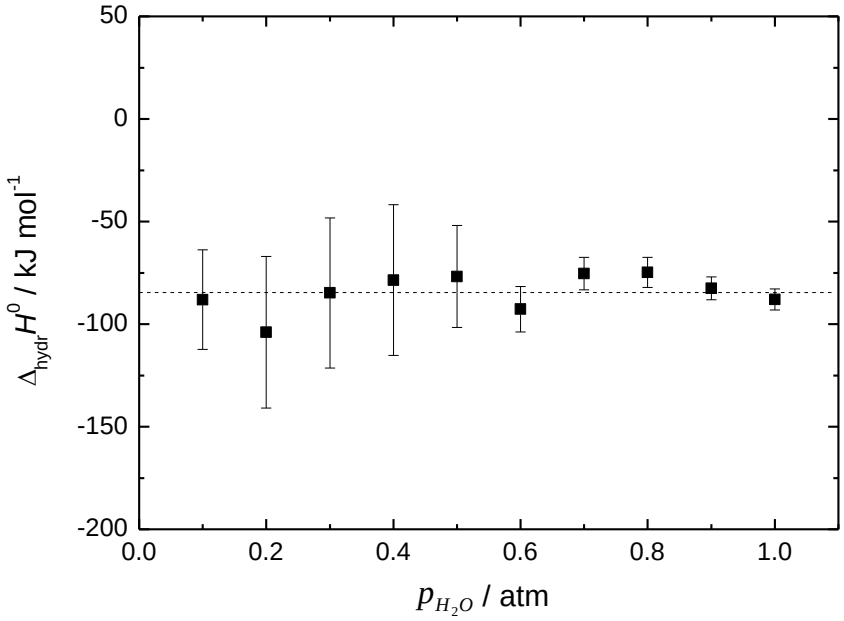

Figure 5.12: Standard molar hydration enthalpies determined for CZSc20 as a function of p_{H_2O} at 500 °C measured by TG-DSC.

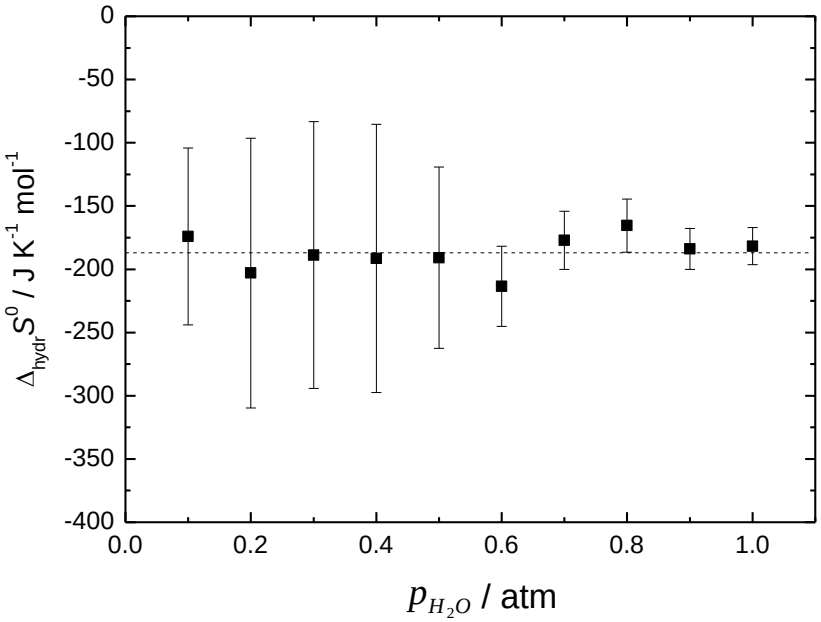

Figure 5.13: Standard molar hydration entropies determined indirectly for CZSc20 as a function of p_{H_2O} at 500 °C using TG-DSC.

5.3. TG-DSC results of CSSc

5.3.1. Hydration thermodynamics as a function of acceptor concentration

As for CZSc, the hydration thermodynamics of CSSc was studied using the TG-DSC technique. Figure 5.14 and 5.15 presents the enthalpy and entropy of hydration, respectively. Despite the discrepancies in the results, hydration enthalpies and entropies become increasingly negative with increasing levels of Sc.

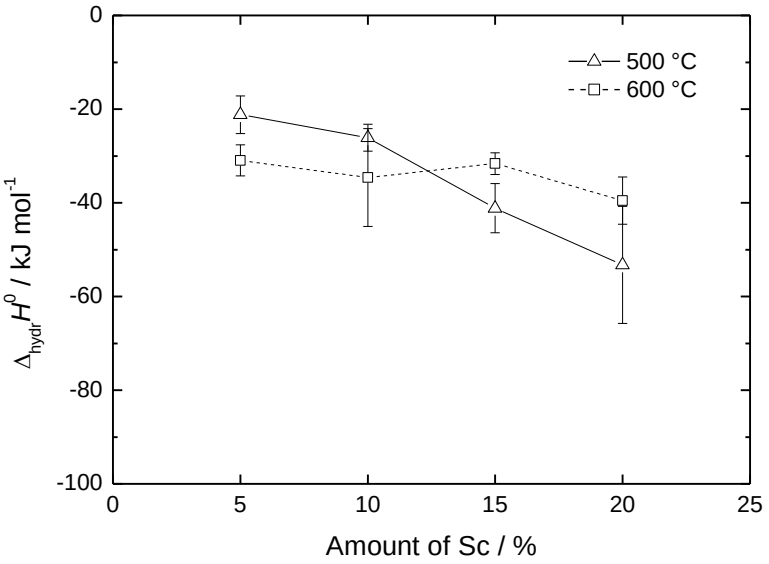

Figure 5.14: Standard molar hydration enthalpies of CSSc as a function of Sc substitution evaluated by TG-DSC at 500 °C and 600 °C.

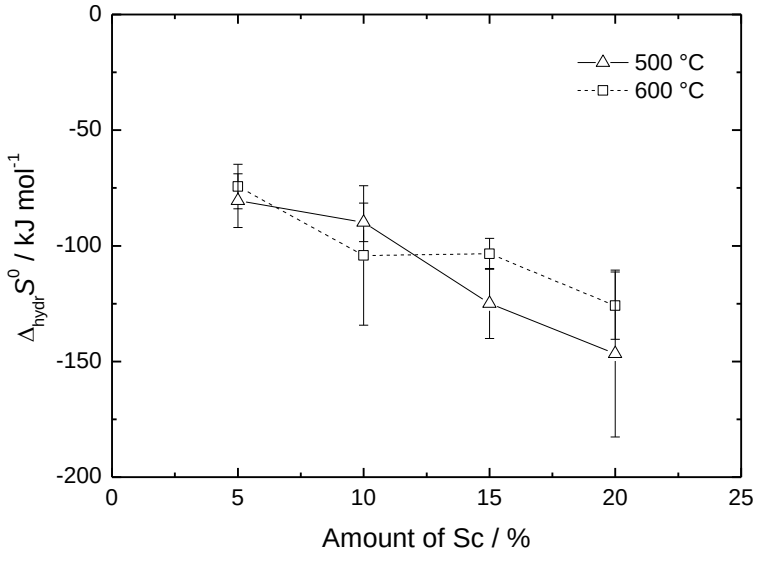

Figure 5.15: Standard molar hydration entropies of CSSc as a function of Sc substitution evaluated by TG-DSC measurements at 500 °C and 600 °C.

The DSC hydration peaks for CSSc with varying levels of Sc are given in Figure 5.16. As illustrated, CSSc10 exhibits the highest intensity at 500 °C. The trend difference in intensities for CZSc and CSSc may be reflected through the calculated proton concentrations and equilibrium constants based on the evaluated thermodynamics. These are summarised in Table 5.2. As is indicated, the trend in peak intensities are in agreement with the evaluated proton concentrations. This is also reflected for the measurements conducted at 600 °C.

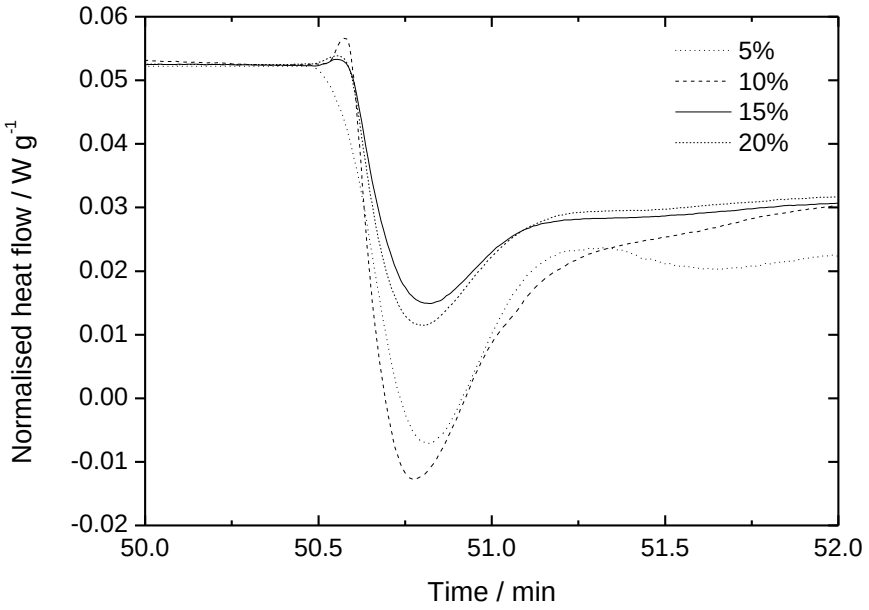

Figure 5.16: DSC hydration peak intensities as a function of amount of Sc dopant in CSSc.

Table 5.2: Summary of the evaluated thermodynamic parameters, equilibrium constants and proton concentrations at 500 °C. All values have been found using the experimental results from TG-DSC.

Amount of Sc / %	$\Delta_{hydr}H^0$ / kJ mol^{-1}	$\Delta_{hydr}S^0$ / kJ mol^{-1}	$K_{hydr} \times 10^{-5}$	$[OH_O^{\bullet}]$ / mol/mol
5	-21 ± 4	-80 ± 10	174	1.0%
10	-26 ± 3	-90 ± 11	114	1.2%
15	-41 ± 5	-125 ± 10	17.4	0.60%
20	-53 ± 12	-147 ± 11	7.98	0.48%

5.4. Thermogravimetric investigation of CZSc20 and CSSc10

Thermogravimetric (TG) investigations of CZSc20 and CSSc10 were carried out and the results are shown in Figure 5.17 (a) and (b), respectively. Both exhibit a small instability with

respect to the mass, which is not fully corrected for by appropriate backgrounds. This instability is not encountered at the lower temperatures for CZSc20 presumably due to the oxygen vacancies not being fully hydrated during the isothermal segment. For CSSc10, the negligible water uptake observed correlates well with the thermodynamic parameters obtained from TG-DSC.

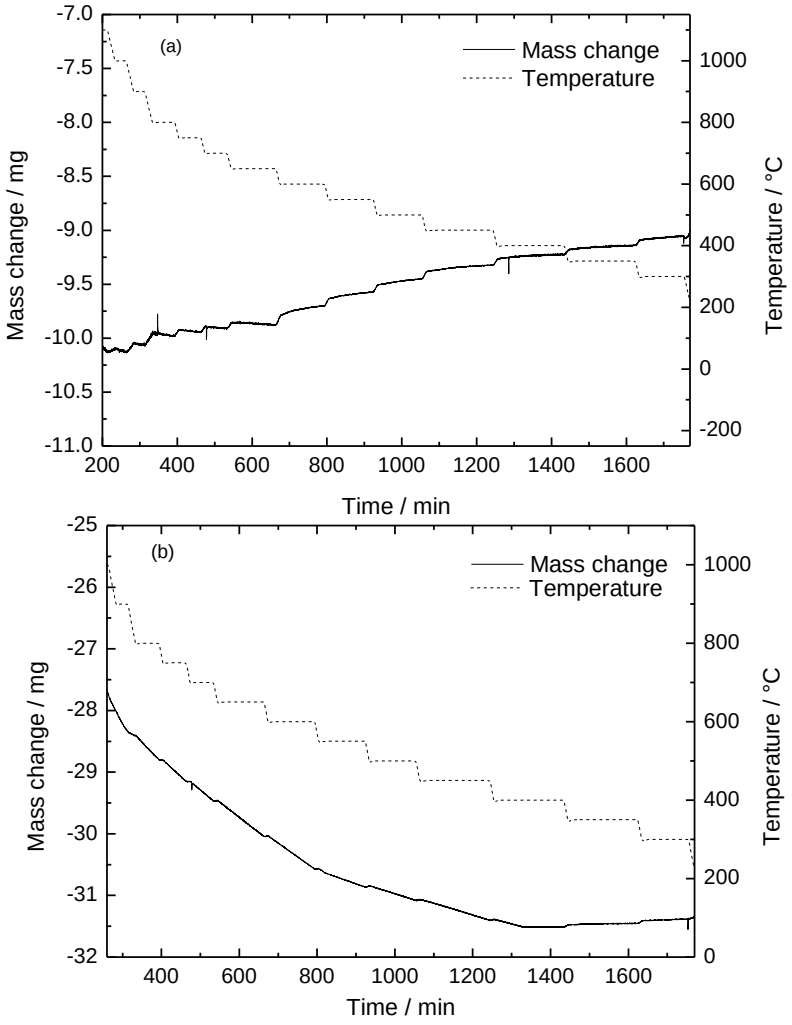

Figure 5.17: Thermogravimetric measurement of CZSc20 (a) and CSSc10 (b) in reducing (8 % H_2 and 90 % He) and inert atmospheres (He), respectively. p_{H_2O} was 0.02 atm for both measurements.

5.5. Electrical characterisation of CSSc5

5.5.1. Impedance spectroscopy analysis

The electrical response of $CaSn_{0.95}Sc_{0.05}O_{3-\delta}$ (CSSc5) was recorded between 150-600 °C using impedance spectroscopy. The frequency interval used was 1 MHz – 1 Hz if not else stated. These impedance spectra allowed the calculation of separate grain boundary and bulk resistivities by implementing the brick layer model specified in section 2.3.4. This is achieved by deconvoluting the spectra using the program EqC for Windows [103]. It should be noted that the impedance spectra presented in the figures are not corrected for geometry and are therefore given in units of Ω. However, when analysing the specific conductivities, both the stray capacitance and geometry were corrected for.

Figure 5.18 presents selected impedance spectra of CSSc5 recorded in dry and wet O_2 and Ar at various temperatures. The spectra consist of up to three contributions, depending on temperature; two distinct high frequency semicircles and a low frequency contribution. The two high frequency contributions merge together to one, large deformed semicircle at temperatures exceeding 400 °C, whereas the low frequency contribution is present in spectra recorded above 300 °C.

An equivalent circuit of two parallel subcircuits in series, $(R_1Q_1)(R_2Q_2)$, was found to be appropriate for temperatures up to 400 °C. At temperatures exceeding 450 °C , the high frequency semicircle was outside the applied frequency range, and the spectra only exhibit two lower frequency semicircles. $R_1(R_2Q_2)(R_3Q_3)$ was thus chosen to be the appropriate equivalent circuit. Upon deconvolution, the corresponding capacitances of the constant phase elements were determined to be 10^{-12}, 10^{-11} and 10^{-6} F cm^{-1}. Capacitances in the pF-range are generally attributed to a bulk response, while grain boundaries and electrodes exhibit typical values of nF and μF, respectively. According to Fleig and Maier [104], a porous sample may decrease the capacitance of the grain boundary semicircle and as such may result in a larger deformed semicircle in line with the presented spectra. Other details from the deconvolution of the impedance spectra in Figure 5.18 are listed in Table 5.3.

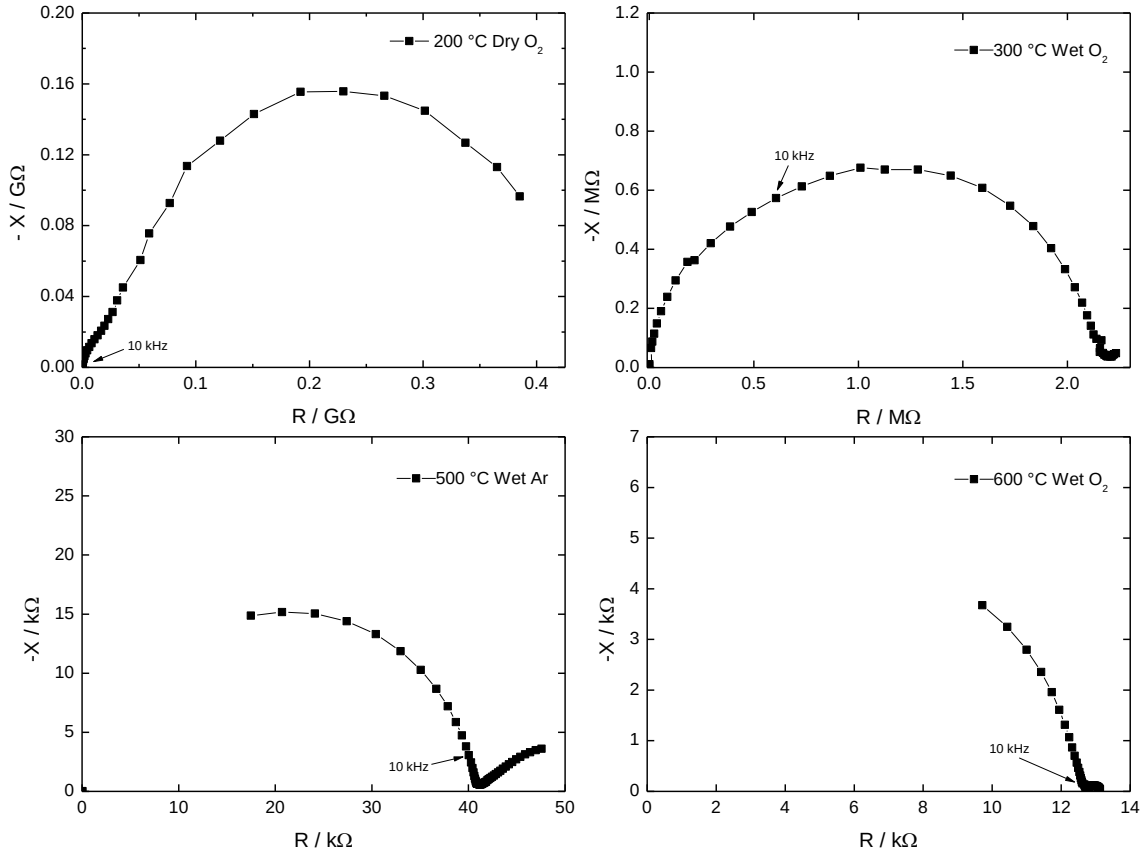

Figure 5.18: Selected impedance spectra of CSSc5 at various conditions measured from 1 MHz to 1 Hz using the Novocontrol instrument. The spectra have not been corrected for stray capacitance, sample geometry or porosity. The results of the deconvolution are summarised in Table 5.3.

The specific grain boundary conductivity could not be calculated based on the capacitances presented as the capacitance was not found to be in the appropriate region for grain boundaries due to the associated porosity of the sample (Figure 5.4). It similarly corresponded to incorrect microstructural parameters as the ratio of the C_2 and C_1 from the second and first semicircle, respectively, normally represents the grain size divided by the grain boundary width (G/g). A common microstructure may consist of microsized grains and nanodimensional grain boundary widths. Thus, the ratio is normally in the range of 1000. However, in this case it was consistently found to be lower than 100. All conductivities that were found to be in the "grain boundary range" were therefore presented as the reciprocal resistivity associated with the second semicircle. This was similarly done for the bulk for comparison.

Table 5.3: Results from the deconvolution of the given impedance spectra in Figure 5.18. The values have been corrected for sample geometry and stray capacitance.

T / °C	Condition	ρ_1 / kΩ cm	n_1	C_1 / pF cm^{-1}	ρ_2 / MΩ cm	n_2	C_2 / pF cm^{-1}	ρ_3 / kΩ cm	n_3	C_3 / µF cm^{-1}
200	Dry O_2	81000	0.88	3.17	1980	0.75	22.4	-	-	-
300	Wet O_2	2530	1	0.97	7.06	0.75	15.8	-	-	-
500	Wet Ar	41.2	-	-	0.138	0.82	11.0	120	0.43	10.4
600	Wet O_2	19.8	-	-	0.0356	0.82	18.6	2.97	0.39	1.01

The dielectric constant, ε_r, can also be extracted from the bulk capacitance with values of 1-2 in the temperature interval studied. However, it was found that after long exposure at higher temperatures (1000-1100 °C), ε_r increased to about 9-11 indicating a change to its electric response. This may stem from the formation of tin vacancies through Equation 2.1 and Equation 2.2 that is demonstrated to occur at 1100 °C and above by XRD (Figure 5.1 and Figure 5.2). However, no evidence of tin evaporation was found by EDS and SEM after the measurements were finalised, but this may be due to the limitations of the equipment. These values are still both considered to be consistent with ε_r of ~ 6 for a single crystal of undoped $CaSnO_3$ by Azad et al. [38].

5.5.2. p_{H_2O} dependencies

The total conductivity (10 kHz) was found to be approximately independent of p_{H_2O} in the temperature range 300 – 1000 °C. To study the effect of p_{H_2O} on the various circuit elements described in the preceeding section, the impedance spectra were measured as a function of temperature (150 – 600 °C), and moreover as a function of p_{H_2O} and p_{D_2O} (3×10^{-5} - 0.03 atm). Figure 5.19 presents spectra obtained at 200 and 400 °C for dry, H_2O- and D_2O-wetted O_2. At 200 °C, the spectra exhibit a large difference in resistance for the "grain boundary" semicircle, while the inset indicates a small difference for the bulk contribution. The larger resistance in D_2O indicates a contribution from protons, while no isotope effect is present for the bulk response. The spectra exhibit a similar effect at 400 °C.

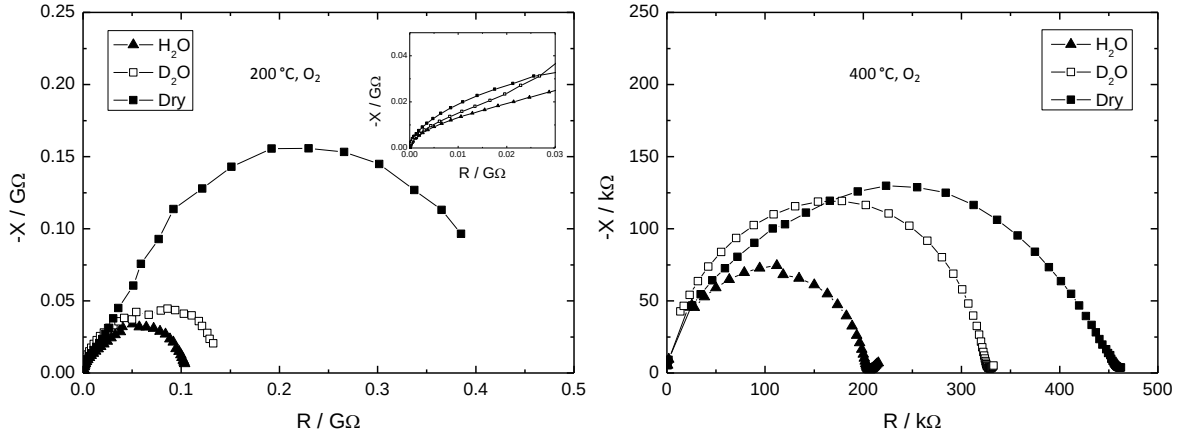

Figure 5.19: Impedance sweeps in O_2 at 200 and 400 °C under wet (H_2O and D_2O) and dry conditions.

The deconvoluted resistivities (ρ_1 and ρ_2, respectively) are summarised in Figure 5.20. ρ_1 is approximately independent of p_{H_2O} in correspondence with the constant frequency measurements and impedance spectra (Figure 5.19) suggesting that the hydration of oxygen vacancies is found to be unfavourable. However, ρ_2 decreased with p_{H_2O} (200-350 °C) indicative of a protonic contribution to the conductivity. The results corresponding to 150 °C show a smaller dependency contradicting the usual trend found for hydration. This can be assumed to be due to slow equilibria, which may limit the diffusion of the defects at such low temperatures. ρ_2 was also independent of p_{H_2O} at 400 °C and above (not shown here).

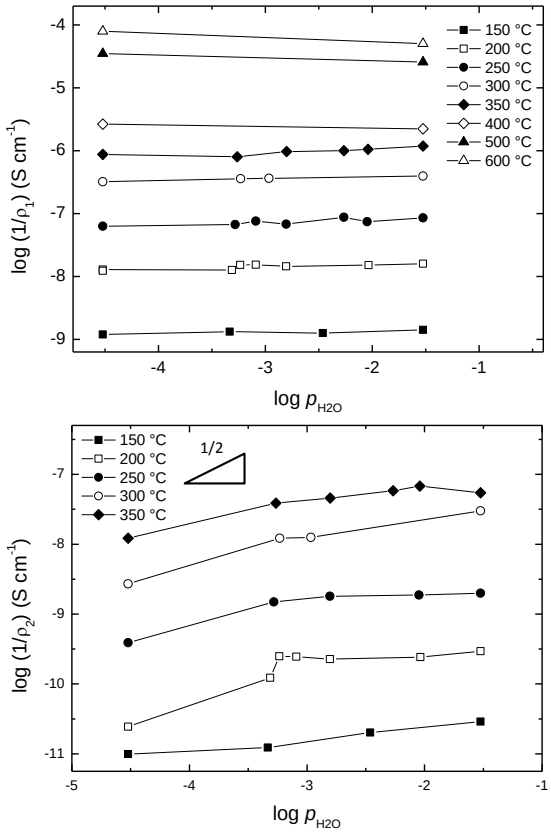

Figure 5.20: Reciprocal bulk (top) and grain boundary (bottom) resistivities as a function of p_{H_2O} in O_2 determined from impedance spectroscopy. Note that the reciprocal bulk resisitivity is the same as its specific conductivity. Grain boundary data have not included any high temperature measurements (400 °C and above) for clarity.

5.5.3. p_{O_2} dependencies

Total conductivity measurements were conducted as a function of p_{O_2} from 400 to 1100 °C (Figure 5.21). The conductivity is independent of p_{O_2} up to 600 °C and increases with p_{O_2} in the interval 800-1100 °C.

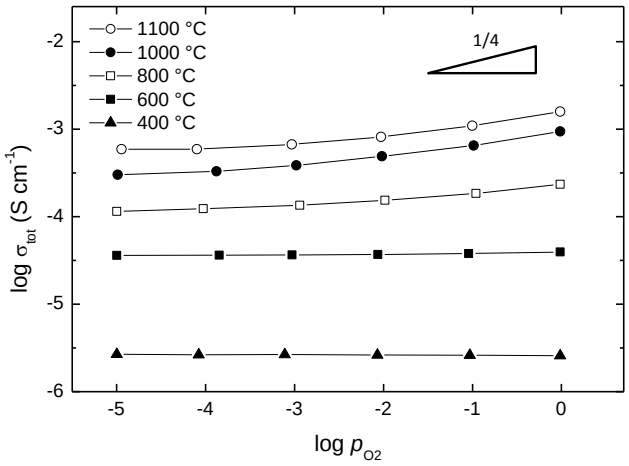

Figure 5.21: Total conductivities measured at 10 kHz as a function of p_{O_2} under wet conditions (p_{H_2O} = 0.03 atm).

Individual specific conductivities from the bulk and grain boundaries were also calculated for lower temperatures (150-500 °C) and are presented in Figure 5.22. These are essentially independent of p_{O_2} in correspondence with the constant frequency measurements.

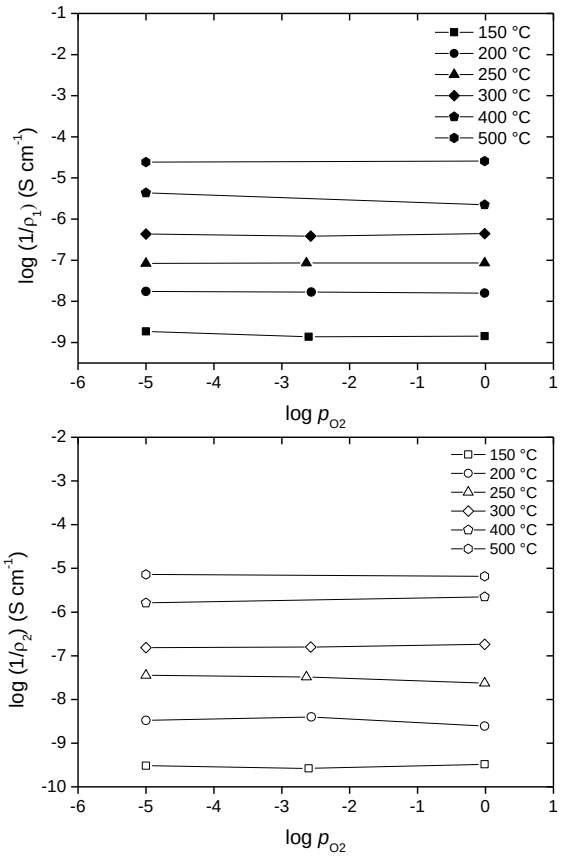

Figure 5.22: Reciprocal resistivities as a function of p_{O_2}. Closed and open symbols correspond to bulk and grain boundaries, respectively.

5.6. Electrical characterisation of CSZn1

5.6.1. Impedance spectroscopy analysis

The electrical response of $CaSn_{0.89}Sc_{0.1}Zn_{0.01}O_{3-\delta}$ (CSZn1) was recorded between 300 and 700 °C using impedance spectroscopy. A few characteristic impedance spectra have been chosen and are shown in Figure 5.23. At 300 °C, the spectra exhibit two contributions and were therefore chosen to be deconvoluted using an equivalent circuit of $(R_1Q_1)(R_2Q_2)$ corresponding to the bulk and grain boundaries, respectively. At 400-500 °C, a third contribution corresponding to an electrode response appears. An equivalent circuit of $(R_1Q_1)(R_2Q_2)(R_3Q_3)$ was thus found to be appropriate for this range. At 700 °C, the semicircle corresponding to the bulk response vanishes and a final equivalent circuit of $R_1(R_2Q_2)(R_3Q_3)$ was therefore used. The four spectra shown have all been deconvoluted with values summarised in Table 5.4. All the values are considered to be typical for each of the contributions.

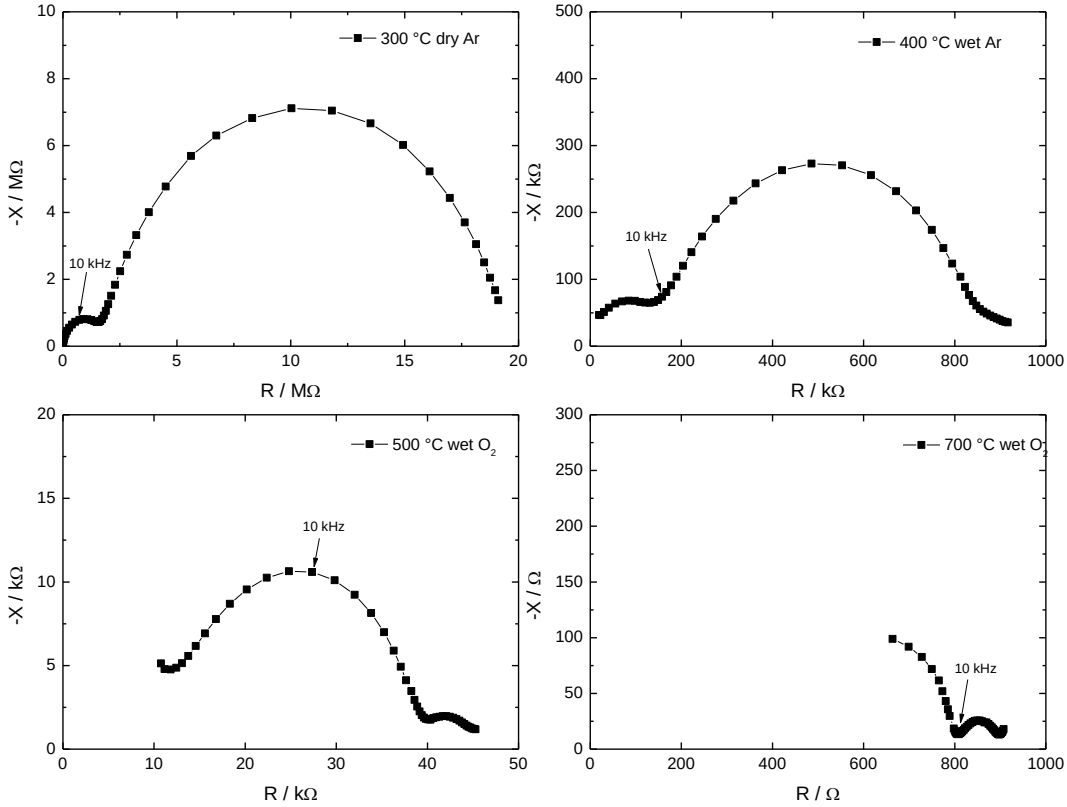

Figure 5.23: Selected impedance spectra of CSZn1 at various conditions measured from 1 MHz to 1 Hz using the Novocontrol instrument. The spectra have not been corrected for stray capacitance, sample geometry or porosity. Results from the deconvolution are summarised in Table 5.4.

ε_r was extracted from the bulk response with values of 14-21 at the various temperatures and conditions studied. The higher dielectric constants in relation to CSSc5 and undoped $CaSnO_3$ (ε_r ~ 6 [38]) could possibly be attributed to the higher levels of acceptor doping and use of sintering aid.

Table 5.4: Results from the deconvolution of the given impedance spectra in Figure 5.23. The values have been corrected for sample geometry and stray capacitance.

T / °C	Condition	ρ_1 / kΩ cm	n_1	C_1 / pF cm^{-1}	ρ_2 / kΩ cm	n_2	C_2 / nF cm^{-1}	ρ_3 / kΩ cm	n_3	C_3 / µF cm^{-1}
300	Dry Ar	4200	0.85	4.69	45000	0.84	0.52	-	-	-
400	Wet Ar	390	0.73	7.24	1760	0.75	0.61	203	0.84	0.99
500	Wet O_2	31.8	0.78	5.58	66.5	0.85	0.54	15.5	0.67	1.73
700	Wet O_2	15.8	-	-	4.1	0.95	1.40	0.30	0.49	14.8

5.6.2. p_{H_2O} dependencies

Conductivities as a function of p_{H_2O} were investigated at 300-500 °C using impedance spectroscopy. Spectra recorded in wet and dry Ar at 300 and 500 °C are given in Figure 5.24. These exhibit differences in resistances between wet and dry conditions indicative of a protonic contribution to the conductivity. These differences also decrease with increasing temperature. The corresponding specific conductivities for the bulk and grain boundaries have been calculated through the brick layer model (see section 2.3.4 for further details) and are summarised in Figure 5.25. At 300 and 400 °C, the conductivities increase with increasing levels of p_{H_2O} while at 500 °C, the conductivity is approximately independent of p_{H_2O}. It should be noted that at 300 °C, the bulk conductivity exhibited a lower p_{H_2O} dependency at low p_{H_2O} than at 400 °C, which may suggest that the sample had not fully equilibrated.

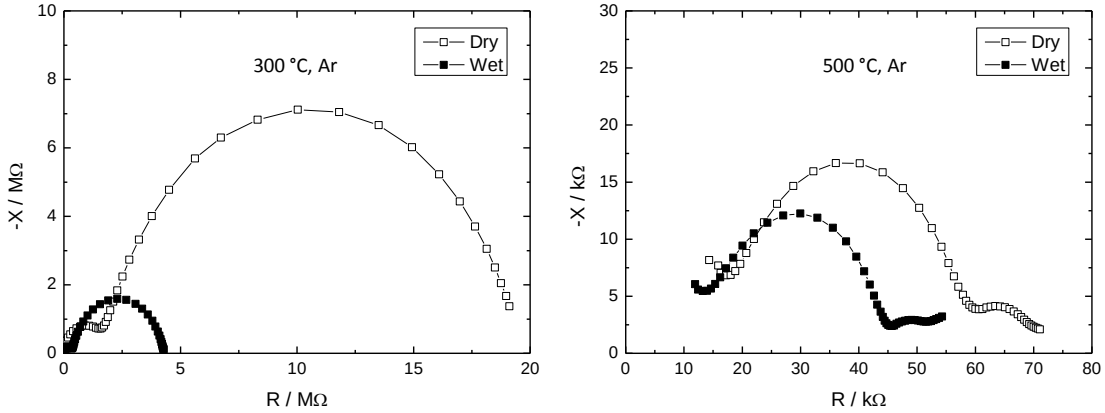

Figure 5.24: Impedance spectra of CSZn1 at 300 and 500 °C in dry and wet Ar.

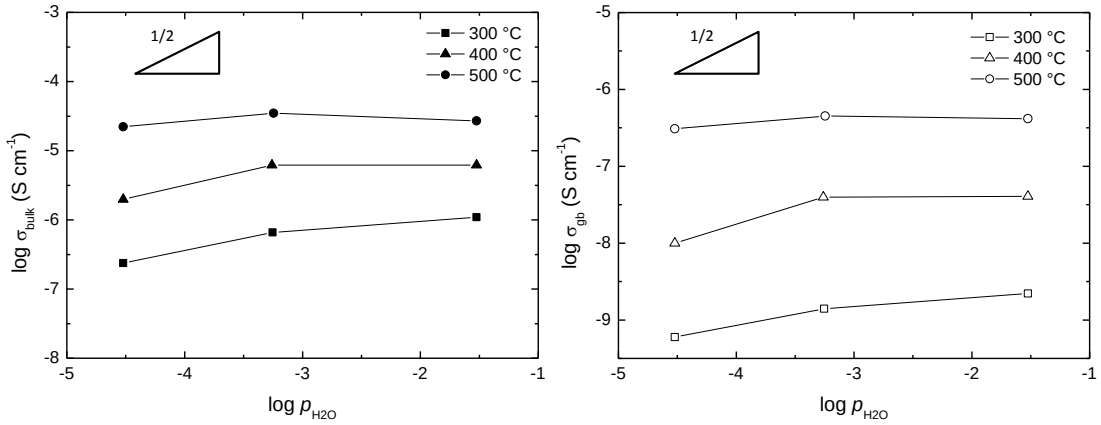

Figure 5.25: Specific bulk (left) and grain boundary (right) conductivities as a function of p_{H_2O}.

Space charge effects

By assuming that the Mott–Schottky approximation applies (see section 2.4 for further details) with equal mobilities in the space charge layers and grain interiors, the Schottky barrier height ($\Delta\varphi(0)$) may be calculated through:

$$\frac{\sigma_{bulk}}{\sigma_{gb}} \cong \frac{k_B T}{2ze\Delta\varphi(0)} \exp\left(\frac{ze\Delta\varphi(0)}{k_B T}\right) \qquad \textbf{Equation 5.2}$$

Schottky barrier heights were calculated by assuming that protons and oxygen vacancies dominated under wet and dry conditions, respectively. These values are summarised in Table 5.5. As indicated the calculated $\Delta\varphi(0)$ is always lower under dry conditions than in wet conditions reflecting a change in grain boundary core charge during hydration as was similarly demonstrated for BZY10 by Kjølseth et al. [26] (see section 3.3 for further details).

All barrier heights were found to be approximately independent of temperature and are of similar magnitudes to those reported for related materials in the literature. The assumption that protons dominate under wet conditions at 500 °C for CSZn1 is supported by the consistency of the $\Delta\varphi(0)$ values.

Using the specific conductivities, activation energies of the bulk were calculated using a van't Hoff plot. Grain boundary activation energies were calculated using Equation 2.62. These energies are summarised in Table 5.5. $\Delta\varphi(0)$ was assumed to be independent of temperature in the course of these calculations. The activation energies are consistently higher under dry conditions, which for the grain boundaries indicates a larger depletion of charge carriers due to the presence of space charge layers. It may be noted that while no grain boundary study has been conducted on acceptor doped $CaSnO_3$, the activation energies are comparable with work done on BZY10 in wet O_2 by Bohn and Schober [105] and Kjølseth et al. [26] with values of 68 kJ mol^{-1} and 81 – 110 kJ mol^{-1}, respectively.

The microstructural parameters calculated based on the bulk and grain boundary capacitances from the impedance spectra indicated an average grain boundary thickness of 5 nm (core and 2 × space charge layer thicknesses) given that the average grain size is assumed to be 0.5 μm. The grain size was based on the SEM micrographs of CSZn2, which are shown in Figure 5.3. Again the Mott-Schottky approximation can be used to calculate the space charge layer thickness, λ^*,through Equation 2.54 and was evaluated with a value of approximately 1.9 nm corresponding well with the grain boundary thickness.

Table 5.5: Calculated Schottky barrier heights and activation energies under various conditions and temperatures. Protons and oxygen vacancies have been assumed to dominate under wet and dry conditions, respectively. *Note that the activation energies for wet O_2 have been calculated using the results under wet Ar.

	$\Delta\varphi(0)$ / V			E_A / kJ mol^{-1}	
	300 °C	400 °C	500 °C	bulk	gb
Wet Ar	0.51	0.52	0.55	64 ± 2	109 ± 1
Dry Ar	0.25	0.27	0.27	88 ± 10	134 ± 3
Wet O_2	-	-	0.54	64 ± 2*	111*

5.6.3. p_{O_2} dependencies

Impedance spectra were similarly recorded as a function of p_{O_2} at 500-700 °C. Impedance spectra recorded at 500 and 700 °C in wet Ar and O_2 are displayed in Figure 5.26. The difference in the respective resistances is larger with increasing temperature. However, these

differences are negligible for both contributions except at the highest temperatures as is indicated in the specific conductivities presented in Figure 5.27. The specific grain boundary conductivities at 700 °C have been calculated using the bulk capacitances at 500 °C under similar conditions. Note that at 1000 °C, the total conductivity is presented.

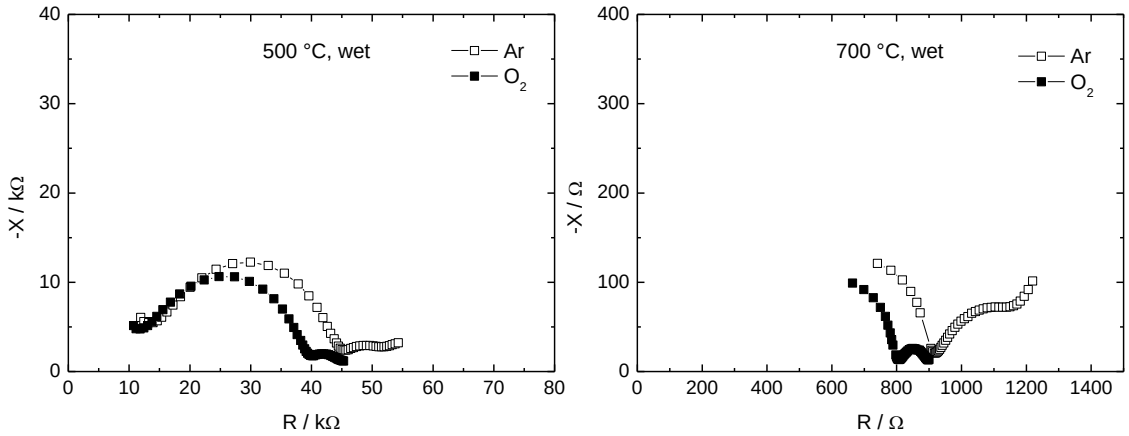

Figure 5.26: Impedance spectra of CSZn1 at 300 and 500 °C in wet Ar and O_2.

There was observed no difference in $\Delta\varphi(0)$ between Ar and O_2 at 500 °C (Table 5.5) suggesting that the grain boundary core charge did not change upon making a change in p_{O_2}.

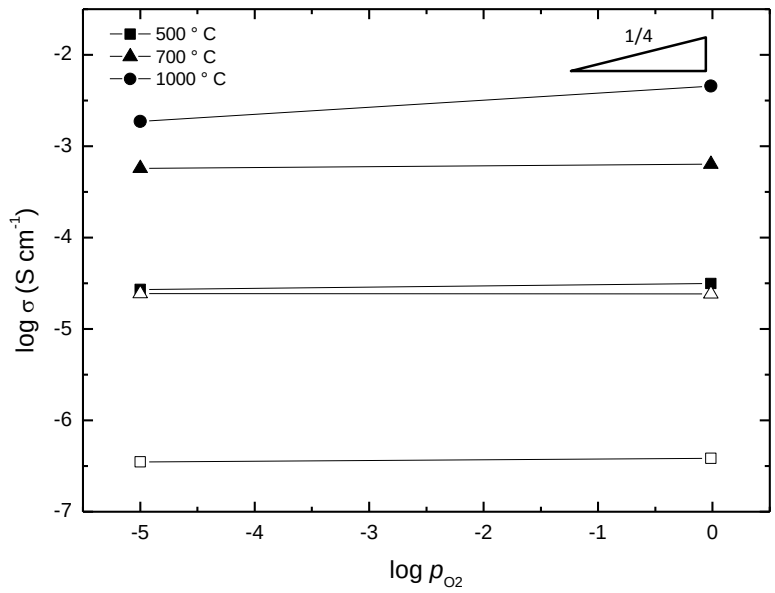

Figure 5.27: Specific bulk (closed symbols) and grain boundary (open symbols) conductivities plotted against p_{O_2}. Specific grain boundary conductivities for 700 °C have been calculated using the bulk capacitances at 500 °C. Conductivity at 1000 °C is the total conductivity from constant frequency measurements.

6. Discussion

In this section, the experimental results obtained by conductivity measurements, TG and TG-DSC will be discussed to describe the defect structure of Sc-doped $CaSnO_3$ and $CaZrO_3$. The discussion will then mainly focus on elucidating the trends in hydration thermodynamics by comparing the results to available literature.

6.1. CSSc – Conductivity, TG and TG-DSC

6.1.1. CSSc – Bulk

Defect structure

The presented partial pressure dependencies of the bulk properties of CSZn1 and CSSc5 will be explained with respect to the full electroneutrality condition

$$n + \left[\mathrm{Acc}^{/}\right] = 2[\mathrm{v}_{\mathrm{O}}^{\bullet\bullet}] + [\mathrm{OH}_{\mathrm{O}}^{\bullet}] + p \qquad \textbf{Equation 6.1}$$

and Brouwer diagrams given in the section on theory (Figure 2.2).

At elevated temperatures (1000-1100 °C), both samples exhibited close to $p_{\mathrm{O}_2}{}^{\frac{1}{4}}$ dependencies at the highest levels of p_{O_2} (Figure 5.21 and Figure 5.27). Such dependencies indicate that the samples are in a region of the Brouwer diagram where the acceptors are fully compensated by ionic defects:

$$\left[\mathrm{Acc}^{/}\right] = 2[\mathrm{v}_{\mathrm{O}}^{\bullet\bullet}] + [\mathrm{OH}_{\mathrm{O}}^{\bullet}] \qquad \textbf{Equation 6.2}$$

As such, the holes act as minority defects and their concentrations increase by $p_{\mathrm{O}_2}{}^{\frac{1}{4}}$ (Figure 5.21 and Figure 5.27). A small concentration of holes is similarly in accordance with the high band gap of 4.44 eV reported by Zhang et al. [30] for undoped $CaSnO_3$. Due to a higher mobility of electronic defects, the electron holes dominate the conductivity at the highest levels of p_{O_2}. Upon lowering p_{O_2}, the concentration of holes diminishes and the conductivity becomes independent of p_{O_2}. Such behaviour corresponds to purely ionic contributions to the conductivity. As the conductivity of both samples exhibited approximately no effect of $p_{\mathrm{H_2O}}$ at temperatures above 400 °C (Figure 5.20 and Figure 5.25), the ionic contribution could be ascribed to oxygen vacancies.

The conductivity of CSSc5 exhibited no p_{H_2O} or H/D isotope effects (Figure 5.19 and Figure 5.20) indicating pure oxygen ion conductivity, i.e. the acceptors are fully compensated by oxygen vacancies $[Acc^{/}] = 2[v_O^{\bullet\bullet}]$. This behaviour differed for the conductivity of CSZn1, which at lower temperatures (300-400 °C) exhibited close to a $p_{H_2O}{}^{\frac{1}{2}}$ dependency at low p_{H_2O}. Upon increasing p_{H_2O}, the conductivity transcended into a region where it was independent of p_{H_2O}. This demonstrates a transition from $[Acc^{/}] = 2[v_O^{\bullet\bullet}]$ to $[Acc^{/}] = [OH_O^{\bullet\bullet}]$ under dry and wet conditions, respectively. However, given that the p_{H_2O} dependency was always lower than $p_{H_2O}{}^{\frac{1}{2}}$, the acceptors can be considered to be partially compensated by protons under dry conditions (Equation 6.2). These small dependencies are in agreement with the TG measurements of CSSc10 (Figure 5.17b) and unfavourable hydration thermodynamics evaluated by TG-DSC for CSSc5 and CSSc10 (Figure 5.14 and Figure 5.15).

The different p_{H_2O} dependencies exhibited in CSSc5 and CSZn1 (Figure 5.20 and Figure 5.25) can be explained in terms of the increased acceptor concentration, as TG-DSC measurements have demonstrated that higher acceptor concentrations exhibit more negative hydration enthalpies (Figure 5.14). Such a trend indicates a higher proton incorporation for CSZn1 than CSSc5 upon hydration and thus accounts for the observed p_{H_2O} dependencies. Higher levels of acceptors could then correspondingly lead to higher p_{H_2O} dependencies.

Thermodynamic assessment of the bulk conductivity data

Transport properties and hydration parameters were evaluated by fitting the p_{H_2O} dependencies of CSZn1 (Figure 5.25) to a simplified defect model where the acceptor concentration was assumed to be 10 mol % (details are outlined in section 9.1 of the appendix). As the hydration entropy is often considered to be in the range between -80 and -160 J K^{-1} mol^{-1} [59], it was fixed to only vary in this interval during the fitting procedure. All other parameters were allowed to vary freely. The average extracted parameters are given in Table 6.1.

Table 6.1: Average extracted parameters from the modelling performed on the bulk conductivity of CSZn1.

$\Delta_{hydr}H^0$ / kJ mol^{-1}	$\Delta_{hydr}S^0$ / J K^{-1} mol^{-1}	$u_0(OH_O^{\bullet})$ / cm^2 K V^{-1} s^{-1}	$\Delta H_{mob}(OH_O^{\bullet})$ / kJ mol^{-1}	$u_0(v_O^{\bullet\bullet})$ / cm^2 K V^{-1} s^{-1}	$\Delta H_{mob}(v_O^{\bullet\bullet})$ / kJ mol^{-1}
-41 ± 14	-104 ± 23	0.026 ± 0.01	94 ± 1	0.02 ± 0.02	109 ± 5

The extracted enthalpies of proton and oxygen vacancy mobilities from conductivity data are higher than what is considered to be typical values for acceptor doped perovskites (0.4 – 0.6

eV for $\Delta H_{\mathrm{mob}}(\mathrm{OH}_{\mathrm{O}}^{\bullet})$) [106]. This could suggest that these values reflect the reduced symmetry of CSZn1 (see section 3.1.1) as orthorhombic BCY consistently exhibits higher enthalpies of proton mobilities than cubic BZY [106]. Given the higher basicity (or electronegativity) of Sc^{3+}/Zn^{2+} compared to other acceptors such as Y^{3+}, the values may also be a result of trapping due to the stronger interactions between $\mathrm{Sc}_{\mathrm{Sn}}^{/}/\mathrm{Zn}_{\mathrm{Sn}}^{//}$ and the positively charged defects i.e. $\mathrm{OH}_{\mathrm{O}}^{\bullet}$ and $\mathrm{v}_{\mathrm{O}}^{\bullet\bullet}$. $\Delta H_{\mathrm{mob}}(\mathrm{v}_{\mathrm{O}}^{\bullet\bullet})$ is, however, in agreement with the enthalpy of oxygen vacancy mobility reported for $BaSn_{0.875}Y_{0.125}O_{3-\delta}$ (113 kJ mol^{-1}) by Wang [40] suggesting that the evaluated values are reasonable for CSZn1.

The pre-exponential factors of proton and oxygen vacancy mobility are similarly higher than the average values, which for protons are 10-100 cm^2 K/Vs [59]. This could be attributed to a higher vibrational wavenumber of Ca-based perovskites (Table 3.3), which is a direct result of the strength of the OH bond. However, a difference of 300 cm^{-1} in ν_{OH} would only account for a change of 10 % to $u_0(\mathrm{OH}_{\mathrm{O}}^{\bullet})$, and as such cannot fully explain this discrepancy. The increased basicity associated with the introduction of Sc^{3+} may similarly increase the sticking probability as a jumping proton exhibits a stronger electrostatic attraction to the neighbouring oxygen, thus effectively increasing $u_0(\mathrm{OH}_{\mathrm{O}}^{\bullet})$. However, given the large number of parameters that determine these factors, it is difficult to ascertain the true meaning behind their values.

The hydration parameters determined from conductivity data are in agreement with the values evaluated by TG-DSC, $\Delta_{\mathrm{hydr}}H^0$ = -35 kJ mol^{-1} and $\Delta_{\mathrm{hydr}}S^0$ = -104 J K^{-1} mol^{-1} at 600 °C. They similarly correspond to the negligible water uptake exhibited in the TG results (Figure 5.17b) as well as the parameters reported for $BaSn_{0.875}Y_{0.125}O_{3-\delta}$ by Wang [40] with values of -49 kJ mol^{-1} and -87 J K^{-1} mol^{-1}, respectively. Thus, the modelled hydration parameters appear to be accurate for this material.

6.1.2. CSSc – Grain boundaries

Defect structure and thermodynamic assessment

The grain boundary partial pressure dependencies of the two samples will also be explained using the full electroneutrality condition (Equation 6.1) and Brouwer diagams (Figure 2.2). At temperatures above 900 °C the total conductivities of CSSc5 and CSZn1 exhibited close to $p_{\mathrm{O}_2}{}^{\frac{1}{4}}$ dependencies at the highest levels of p_{O_2} (Figure 5.21 and Figure 5.27) indicating that the acceptors are fully compensated by ionic defects i.e. $[\mathrm{v}_{\mathrm{O}}^{\bullet\bullet}]$ and $[\mathrm{OH}_{\mathrm{O}}^{\bullet}]$.

At temperatures up to 350 °C, the grain boundary conductivity of CSSc5 exhibited close to $p_{H_2O}{}^{\frac{1}{2}}$ dependencies at the lower levels of p_{H_2O} and was independent of p_{H_2O} at the higher levels (Figure 5.20). Such behaviour could be ascribed to an increasing concentration of protons compensating the oxygen vacancies i.e. a transition from $[Acc^{/}] = 2[v_O^{\bullet\bullet}]$ under dry conditions to $[Acc^{/}] = [OH_O^{\bullet}]$ under wet conditions. Thus, $[Acc^{/}] = 2[v_O^{\bullet\bullet}] + [OH_O^{\bullet}]$ describes the entire range of p_{H_2O}. This is in accordance with the significant isotope effects exhibited in the grain boundaries at 200 °C (Figure 5.19). The same simplified electroneutrality applies for CSZn1, which exhibits dependencies up to 400 °C (Figure 5.25).

Assuming that grain boundaries exhibit similar transport and hydration properties to the bulk, the p_{H_2O} dependencies of both samples were modelled assuming constant acceptor concentrations of 5 and 10 % for CSSc5 and CSZn1, respectively. Further details regarding the conductivity model are outlined in section 9.1. The modelled conductivities are displayed in Figure 6.1 and compared to the experimental results. The average extracted parameters are summarised in Table 6.2. As indicated, the enthalpies and entropies of hydration become increasingly negative with increasing levels of acceptors in agreement with the TG-DSC results of bulk CSSc (Figure 5.14 and Figure 5.15) and CZSc (Figure 5.6 and Figure 5.7). Such trends will be discussed in more detail in section 6.4.

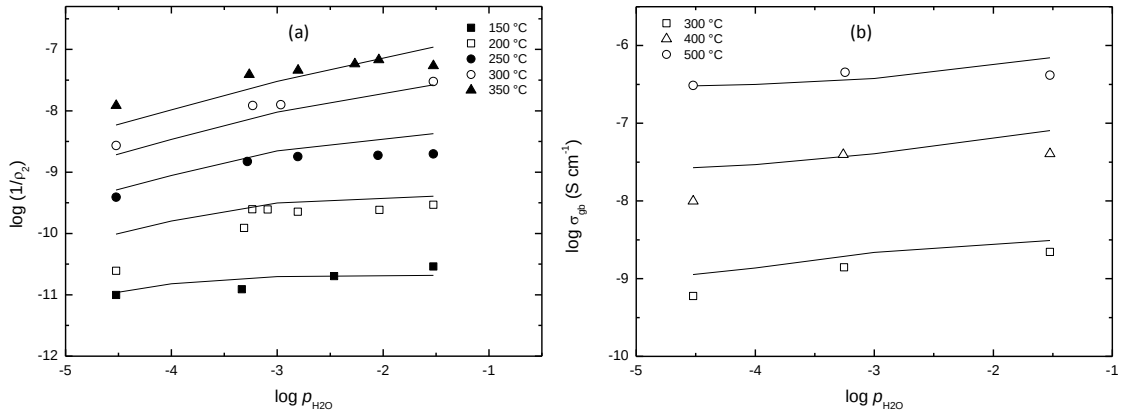

Figure 6.1: Grain boundary conductivities plotted as a function of p_{H_2O} for CSSc5 (a) and CSZn1 (b). Modelled conductivities are represented by the solid lines.

Table 6.2: Extracted parameters from the modelling of the grain boundary conductivities of CSSc5 and CSZn1.

Material	$\Delta_{hydr}H^0$ / kJ mol^{-1}	$\Delta_{hydr}S^0$ / J K^{-1} mol^{-1}	$u_0(OH_O^{\bullet})$ / cm^2 K V^{-1} s^{-1}	$\Delta H_{mob}(OH_O^{\bullet})$ / kJ mol^{-1}	$u_0(v_O^{\bullet\bullet})$ / cm^2 K V^{-1} s^{-1}	$\Delta H_{mob}(v_O^{\bullet\bullet})$ / kJ mol^{-1}
CSZn1	-84 ± 1	-114 ± 1	0.003 ± 0.0004	116 ± 1	0.0005 ± 0.0002	114 ± 2
CSSc5	-68 ± 5	-107 ± 9	0.004 ± 0.0009	103 ± 1	0.002 ± 0.0009	135 ± 2

Space charge effects

Different p_{H_2O} dependencies were exhibited for the bulk and grain boundaries in both samples (Figure 5.20 and Figure 5.25). While this may be a result of different hydration thermodynamics as evaluated in the previous sections (Table 6.1 and Table 6.2), it may also reflect a depletion of oxygen vacancies due to the presence of space charge layers. Such depletions take place to compensate the positive charge of the grain boundary core, and oxygen vacancies deplete more severely than protons due to their double effective charge. Consequently, protons become the majority charge carriers in both samples under wet conditions at low temperatures (300-400 °C). These effects have similarly been demonstrated in acceptor doped $Er_2Ti_2O_7$ by Fjeld et al. [9, 10].

CSSc5 exhibited a larger depletion of oxygen vacancies compared to CSZn1 as indicated in the larger differences in the p_{H_2O} dependencies between the bulk and grain boundaries (Figure 5.20 and Figure 5.25). This suggests a larger Schottky barrier height ($\Delta\varphi(0)$) and grain boundary activation energy ($E_{A,gb}$) in CSSc5 compared to CSZn1 (Table 5.5), which is in accordance with the trend demonstrated in the literature [24, 26, 81]. As such, an undoped sample should exhibit even larger differences in the p_{H_2O} dependencies between the bulk and grain boundaries.

It should be noted that the different p_{H_2O} dependencies may also reflect the existence of a proton conducting phase in the grain boundaries. However, no indication of this was detected by SEM (Figure 5.3 and Figure 5.4) or XRD (Figure 4.2) suggesting that the effects appear to be caused by inherent space charge layers in the samples.

6.2. CZSc – TG and TG-DSC

The defect structure of CZSc will be explained in terms of the Brouwer diagrams and full electroneutrality condition similarly to CSSc (see section 6.1). This will be based on the conductivities of acceptor doped $CaZrO_3$ from the literature (section 3.2.2). At higher temperatures (800 °C and above), conductivities vary as a function of $p_{O_2}^{\frac{1}{4}}$ under oxidising conditions and as such, holes are minority defects in this material [44, 46].

Conductivities in the literature indicate a simplified electroneutrality condition where the acceptors can be described as being fully compensated by oxygen vacancies and/or protons (see section 3.2.2 for further details). This is assumed to apply for all samples of CZSc.

The thermodynamic parameters of hydration may be extracted by modelling the thermogravimetric measurements conducted on CZSc20 (Figure 5.17a) (details in appendix 9.1). However, there were discrepancies in the water uptake obtained under inert and reducing conditions at temperatures below 650 °C. The differences could suggest a transition to a simplified electroneutrality where the concentration of electrons are compensated by oxygen vacancies i.e. $n = 2[\mathrm{v}_{\mathrm{O}}^{\bullet\bullet}]$. As such, a lower p_{O_2} should correspond to a higher proton concentration. Another possibility is that the small concentration of holes under inert conditions are hydrated at elevated temperatures through Equation 6.3. Reducing conditions will thus shift the equilibrium to the right creating differences in the water uptakes measured.

$$\mathrm{H_2O(g)} + 2\mathrm{h}^{\bullet} + 2\mathrm{O}_{\mathrm{O}}^{\mathrm{X}} = 2\mathrm{OH}_{\mathrm{O}}^{\bullet} + \frac{1}{2}\mathrm{O_2(g)} \qquad \textbf{Equation 6.3}$$

The TG results also exhibited limiting hydration kinetics below 600-650 °C (Figure 5.17a) and these temperatures have therefore been excluded in the fitting procedure. This is in agreement with the TG-DSC results of CZSc20 (Figure 5.8) and BZY10 by Kjølseth et al. [7] where hydration kinetics were demonstrated to significantly affect the rate of water uptake at temperatures up to 800 °C. The calculated proton concentrations for both atmospheres are compared to the modelled concentration as shown in Figure 6.2. The extracted thermodynamic parameters were $\Delta_{\mathrm{hydr}}H^0$ = -83 ± 6 kJ mol^{-1} and $\Delta_{\mathrm{hydr}}S^0$ = -136 ± 6 J K^{-1} mol^{-1} when using the water uptake obtained under reducing conditions. Similar results were achieved for the inert conditions. The uncertainty in these values is the resulting standard deviation. The acceptor concentration was assumed to be constant at 20 mol %.

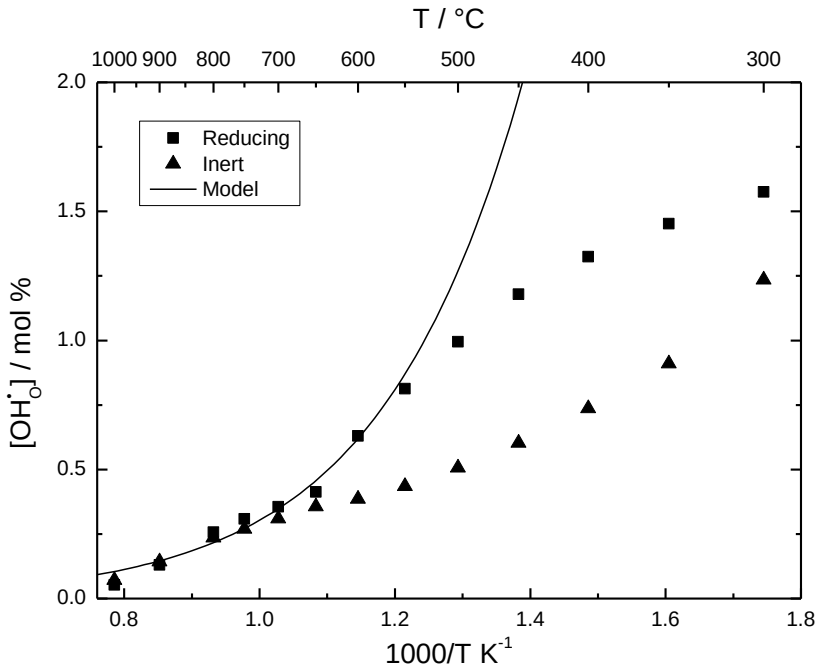

Figure 6.2: Calculated proton concentrations from TG experiments for CZSc20. p_{H_2O} = 0.02 atm for both atmospheres.

The extracted hydration enthalpy is found to be in good agreement with the average hydration enthalpy evaluated by TG-DSC (-95 kJ mol^{-1}) and the value reported by Smith (-87 kJ mol^{-1}) from modelling of conductivity data [44]. However, the effective acceptor concentration has been demonstrated to often be lower than its nominal value [44-46], which may be caused by defect associates, donor dopants and different hydration thermodynamics of oxygen sites as has been discussed in more detail in section 3.2.2. Thus, by varying the effective acceptor concentration in the model to 2, 5, 10 and 20 mol % for the same TG results, we find that there are small differences in the extracted hydration parameters given in Table 6.3.

Table 6.3: Extracted thermodynamic parameters of hydration from the thermogravimetric investigations conducted under reducing conditions.

Effective [Acc$^{/}$] / %	$\Delta_{hydr}H^0$ / kJ mol^{-1}	$\Delta_{hydr}S^0$ / kJ mol^{-1}
2	-91 ± 6	-124 ± 7
5	-85 ± 6	-127 ± 7
10	-83 ± 6	-131 ± 6
20	-83 ± 6	-136 ± 6

6.3. TG-DSC as a technique

Part of the aim of this study was to partially elucidate the validity of TG-DSC by investigating the hydration thermodynamics of CZSc and CSSc using different techniques. Table 6.4 displays the evaluated hydration thermodynamics of CSSc10 and CZSc20. It is assumed that CSZn1 has an acceptor concentration of 10 mol % and as such should be equivalent to CSSc10. The hydration enthalpies evaluated directly by TG-DSC correspond to the values determined by indirect techniques such as TG and conductivity measurements. The evaluated enthalpies were also consistent with respect to temperature (Figure 5.9) and p_{H_2O} (Figure 5.12) for CZSc20 suggesting that the enthalpy is independent of the degree of hydration. This corresponds to earlier work by Kjølseth et al. [7, 94] on BZY10.

Table 6.4: Evaluated hydration thermodynamics of CSSc10 and CZSc20 using different techniques.

	$\Delta_{hydr}H^0$ / kJ mol^{-1}		$\Delta_{hydr}S^0$ / kJ mol^{-1}	
Material	CSSc10	CZSc20	CSSc10	CZSc20
TG-DSC	-30	-95	-97	-182
Conductivity	-41	-	-104	-
TG	-	-83	-	-136

While the hydration entropies are in agreement for CSSc10, the values for CZSc20 are distinctly different (Table 6.4). This discrepancy may indicate an incorrect assumption regarding the TG-DSC entropy calculations, where equilibrium was assumed during the hydration segments. The water uptake from TG-DSC of CZSc20 was consistently lower than the respective TG measurements demonstrating kinetic restrictions of hydration over the entire temperature range (500-900 °C). This suggests that the evaluated hydration entropies of CZSc from TG-DSC are consistently too negative. By assuming that a difference of -48 J K^{-1} mol^{-1} ($\Delta_{\mathrm{hydr}}S^0_{\mathrm{TG-(TG-DSC)}}$ from Table 6.4) is consistent for all doping levels in the CZSc series, proton concentrations may be modelled using the same methodology detailed in the section 9.1 of the appendix. This is given in Figure 6.3. A similar correction is not needed for CSSc, as the evaluated entropies of CSSc10 were consistent for both techniques (Table 6.4).

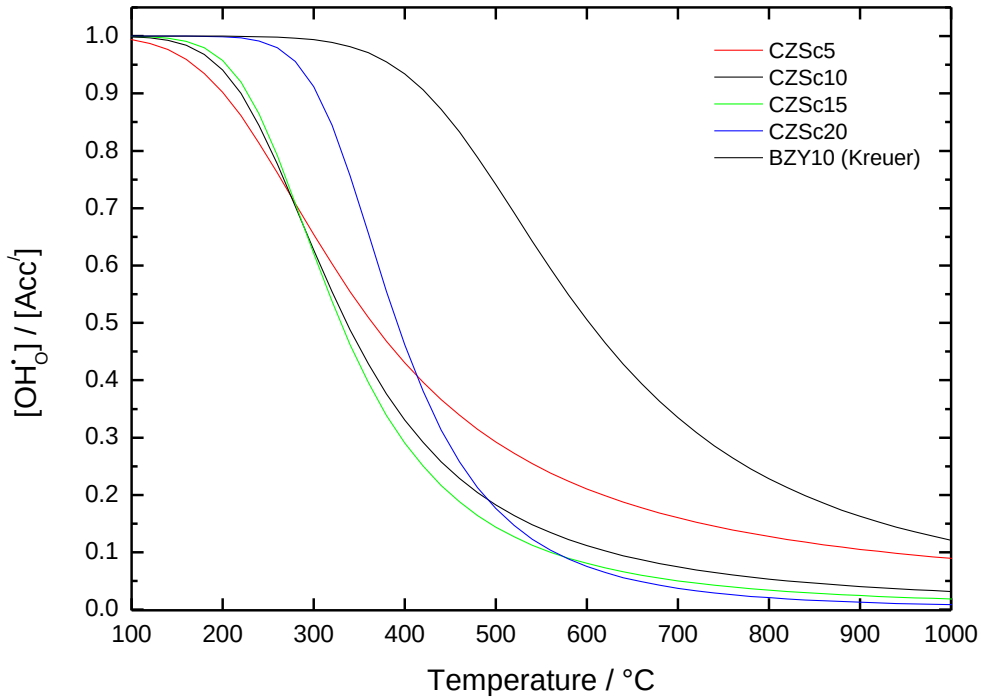

Figure 6.3: Modelled proton concentrations as a function of temperature based on TG-DSC results obtained for CZSc at 600 °C. All calculated entropies have been subtracted by -48 J K^{-1} mol^{-1} as specified in the text. BZY10 with by Kreuer [51] is included for comparison.

Based on the above discussion of results, TG-DSC is indicated to be a valuable technique for the evaluation of hydration enthalpies and entropies thus providing a simple alternative for the determination of hydration thermodynamics of materials. It should be noted that results are more accurate for oxides exhibiting high proton concentrations and quick hydration kinetics limiting its use in certain materials.

6.4. Hydration of perovskites

As touched upon earlier, the thermodynamics of hydration lies at heart in all proton conductors as these parameters determine the water uptake at any given temperature and water vapour partial pressure. Thus, considerable effort has gone into developing correlations between materials properties and $\Delta_{\mathrm{hydr}}H^0$ and $\Delta_{\mathrm{hydr}}S^0$ in oxides in order to predict their proton incorporation and thus hopefully develop good proton conductors for technological commercialisation. However, as discussed in the literature (section 3.3), the current correlations have a limited predicting power due to a high degree of scattering. While this may stem from the discrepancies in the evaluated thermodynamics as illustrated for instance in BZY where values vary from -11.6 to -93.3 kJ mol^{-1} (see section 3.3 for further details),

the correlations themselves may also be too poor. This will be discussed in relation to the results obtained for CZSc and CSSc.

For both series of CSSc and CZSc, the hydration enthalpy and entropy have been shown by TG-DSC to become increasingly negative with increasing levels of Sc substitution (see section 5.2.1 and 5.3.1). While the hydration enthalpy may be correlated to the electronegativity difference of the B- and A-site cations as suggested by Norby et al. [6], the dependency predicted for CZSc is stronger than that observed for other perovskites as illustrated in Figure 6.4a. As $\Delta\chi_{Zr-Sc}$ = 0.02 (Allred-Rochow) [107], a change in the dopant level will not implement a large electronegativity difference for CZSc and thus does not sufficiently explain the observed trend. This is also reflected in work done by Kreuer [52] and Glöckner [53] on BCY, in which $\Delta\chi_{Ce-Y}$ = -0.03, and as such should exhibit a less exothermic enthalpy with higher levels of doping. The reasons for this may however be related to the limitation of using electronegativities, as they are based on the average oxidation state of an element. For instance, it is well known that Sn^{IV} is more electronegative than Sn^{II} [108]. As such, the basicity of the oxide as suggested by Kreuer [51, 52] could be a more useful parameter, as the introduction of a lower charged species such as an acceptor will increase the basicity, thus explaining the observed trends in CZSc, CSSc, BZY [51] and BCY [52] (Figure 6.4b). It should however be noted that an oxide's basicity is interrelated to its electronegativity, which is why they are both capable of explaining the general trends observed in perovskites. However, there is no unit of scale to estimate the basicity of an oxide and as such only qualitative arguments may be made.

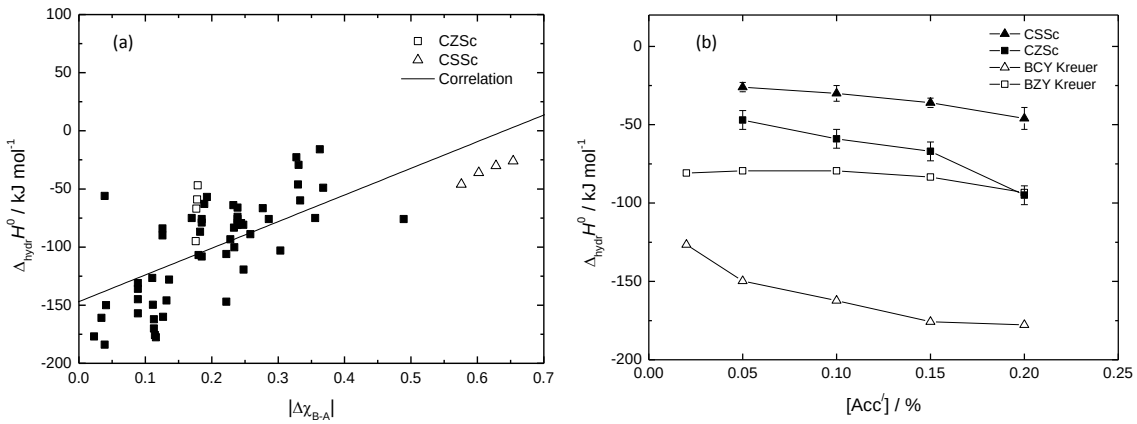

Figure 6.4: Hydration enthalpy plotted against (a) $\Delta\chi_{B-A}$ for a large number of ABO_3 perovskites where results of CSSc and CZSc are included and (b) acceptor concentration for CZSc, CSSc, BZY [51] and BCY [52].

The incorporation of protons may cause structural reorganisations of perovskites and as such the thermodynamics may similarly be linked to structural parameters of perovskites. Such a

correlation has already been suggested by Norby [59] in which the enthalpy becomes increasingly negative with decreasing values of the Goldschmidt tolerance factor for ABO_3 perovskites (Equation 6.4) [109]. As such, it proposes that a larger deviation from the ideal perovskite will exhibit a more negative hydration enthalpy. In Figure 6.5a, the TG-DSC results of CSSc and CZSc are plotted and compared to other ABO_3 perovskites from the literature. While both materials are situated within the large degree of scattering, the enthalpies' dependence to the tolerance factor is too strong. As the structure of perovskites may not be well reflected in the value of the tolerance factor, the use of the fitness factor (ϕ) (Equation 6.5) by Teraoka et al. [110] could give a more accurate indication of the structural dependence. In Figure 6.5b the enthalpies of perovskites have been plotted against ϕ and here CSSc and CZSc are closer together, which thus reflects the crystal structures better as they both belong to the orthorhombic space group *Pbnm* (see section 3.1.1 and 3.2.1). However, it yields no improvement to the proposed correlation and may even suggest that the structure of the perovskite is not one of the dominant properties for hydration enthalpies. An improved correlation could involve a combination of the basicity and tolerance/fitness factors as they both seem to influence the enthalpy change of hydration.

$$t = \frac{r_A + r_B}{\sqrt{2}(r_B + r_O)} \qquad \textbf{Equation 6.4}$$

$$\phi = \frac{\sqrt{2}r_A}{(r_B + r_O)} \qquad \textbf{Equation 6.5}$$

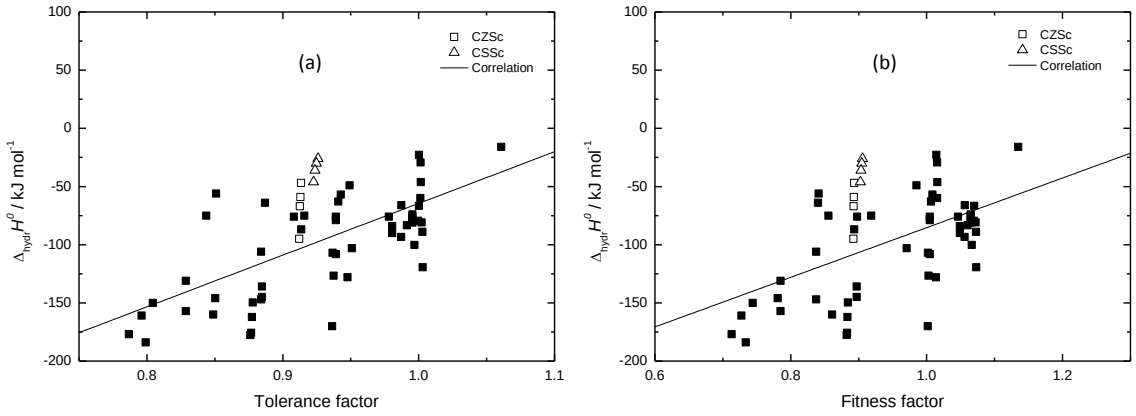

Figure 6.5: Hydration enthalpy plotted against (a) the tolerance factor and (b) the fitness factor in ABO_3 perovskites. Results found by TG-DSC on CZSc and CSSc have been compared to available literature data.

Hydration enthalpy correlations based on structure and basicity both give an indication of the stability of the protons and consequently the strength of the OH bond. Thus, the frequencies or wavenumbers of the vibrational stretching modes of OH (ν_{OH}) may provide a link to the hydration enthalpy, as it gives a clear indication of the OH bond strength [111]. Table 6.5 displays the hydration enthalpies and entropies of some perovskites along with their respective vibrational wavenumbers. It may first be highlighted that the ν_{OH} values do not reflect the given trend in $\Delta_{hydr}H^0$ of the acceptor doped perovskites. This may be a result of the larger deviations in the structure of $CaZrO_3$ compared to $(Ba,Sr)ZrO_3$, in which there are several proton positions limiting the hydration due to different site energies. As such, it suggests that other factors than ν_{OH} are at play for the enthalpy of hydration. On the other hand, the hydration entropies exhibit an apparent correlation to ν_{OH} as illustrated in Figure 6.6, which could be explained by the definition of $\Delta_{hydr}S^0$. The standard entropy change of hydration consists of two terms; the vibrational and configurational entropy changes associated with the incorporation of protons. However, in ideal defect chemistry using the mass action law, this entropy change can be considered to only be a product of the vibrational entropy changes associated with the formation of protons [11]. As such, the differences in hydration entropies in perovskites could simply be due to the differences in the vibrational modes of the protons in the structure as demonstrated in the trend shown (Figure 6.6). In other words, a higher vibrational wavenumber indicates a more negative hydration entropy.

Table 6.5: Evaluated thermodynamics of hydration and vibrational wavenumbers of the OH stretching modes. All ν_{OH} are taken Omata et al. [69] where IR measurements were carried out on 5 % Ga-doped $AZrO_3$ perovskites.

Material	$\Delta_{hydr}H^0$ / kJ mol^{-1}	$\Delta_{hydr}S^0$ / J K^{-1} mol^{-1}	Reference	ν_{OH} / cm^{-1}
$BaZr_{0.95}Y_{0.05}O_{3-\delta}$	-80	-93	[51]	3131
$CaZr_{0.95}Sc_{0.05}O_{3-\delta}$	-47	-122	This work	3451
$SrZr_{0.95}Yb_{0.05}O_{3-\delta}$	-147	-160	[112]	3486
	-106	-127	[72]	

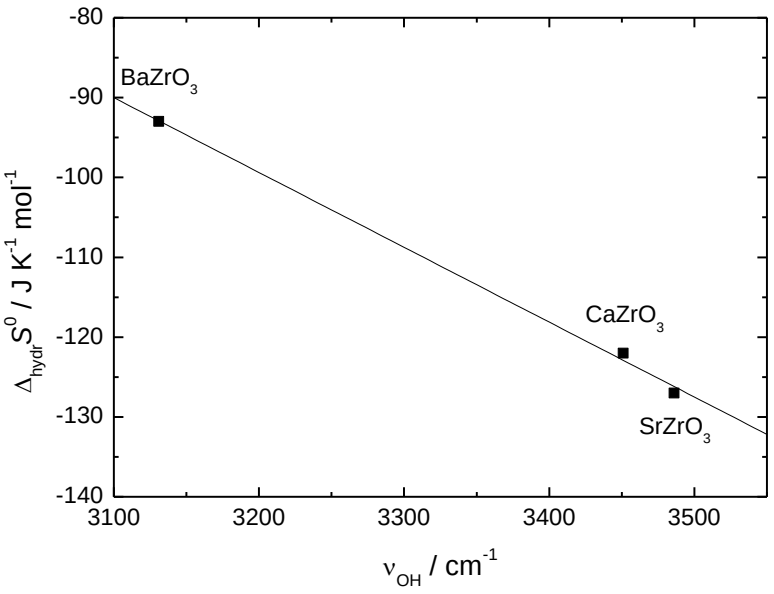

Figure 6.6: Standard molar hydration entropies plotted as a function of ν_{OH} (vibrational wavenumber) for 5 % acceptor doped $AZrO_3$ perovskites. Further details are given in Table 6.5.

Other trends with respect to ν_{OH} are exhibited in $SrZr_{1-x}Sc_xO_{3-\delta}$, where the bonding strength (and ν_{OH}) increased with increasing levels of Sc substitution (Figure 3.9). Such a trend suggests an increasingly negative hydration entropy in correspondence to the already demonstrated connection between $\Delta_{hydr}S^0$ and ν_{OH}. This is analogous to the trends for CSSc and CZSc determined by TG-DSC (Figure 5.7 and Figure 5.15). It should also be noted that such an increase adds to the basicity of the perovskite, which has been demonstrated to decrease its hydration enthalpy (Figure 5.6 and Figure 5.14). In other words, both the parameters of the hydration thermodynamics become increasingly negative as a result of different phenomena. However, these phenomena are related to one another, which may explain the correlation observed between $\Delta_{hydr}H^0$ and $\Delta_{hydr}S^0$ in CZSc, CSSc, BZY [51] and BCY [52]. Materials will therefore exhibit small differences in the proton concentrations with different levels of acceptors as illustrated for CZSc in Figure 6.3.

6.5. Future work

Through the work done in this thesis, CSSc was demonstrated to exhibit inherent space charge layers giving rise to different p_{H_2O} dependencies in the bulk and grain boundaries. Thus an extension of this study would include an investigation of undoped $CaSnO_3$ as the increased Schottky barrier height should induce larger space charge effects and as such provide further insight to the nature of grain boundaries. TEM should also be carried out in order to verify that no secondary phases are present in CSSc.

1-2 mol % ZnO was shown to be an effective sintering aid for 10 % Sc-doped $CaSnO_3$. However, no underlying understanding of the effect was determined. This could be elucidated by varying the level of ZnO and investigating the change in microstructure and sintering behaviour.

Evaluation of hydration thermodynamics by the use of TG-DSC has been demonstrated through calculations on Sc-doped samples of $CaSnO_3$ and $CaZrO_3$ to be both valuable and efficient. A natural continuation of this work would be to study the hydration thermodynamic trends by TG-DSC for other acceptor doped perovskite series such as BZY or BCY, which have been studied extensively in the literature using indirect techniques. Due to the complete solid solubility of these two perovskites, $Ba(Zr_{1-x}Ce_x)Y_{0.1}O_{3-\delta}$ could similarly be investigated. TG-DSC may additionally be used to elucidate thermodynamic trends in other types of oxides such as pyrochlores.

The proposed correlation between the hydration entropy and the vibrational wavenumber of the OH modes (ν_{OH}) should also be investigated for CZSc and CSSc by the use of IR spectroscopy.

7. Conclusions

Based on the experimental results of Sc-doped $CaSnO_3$, it can be concluded that the material is dominated by oxygen vacancies under a wide range of conditions. The electrical characterisation indicated that these vacancies may be hydrated to form protons at sufficiently low temperatures of 300-400 °C for $CaSn_{0.9}Sc_{0.1}O_{3-\delta}$. Modelling of the dependencies of $CaSn_{0.9}Sc_{0.1}O_{3-\delta}$ resulted in a hydration enthalpy and entropy of -41 ± 5 kJ mol^{-1} and -104 ± 7 J K^{-1} mol^{-1}, respectively, which was consistent with results from TG-DSC.

For 5 and 10 % Sc-doped $CaSnO_3$, impedance spectroscopy revealed that oxide ions were the majority charge carrier in the bulk, while protons dominated in the grain boundaries. These differences were suggested to arise due to the presence of inherent space charge layers depleting the oxygen vacancies in the grain boundaries. These effects were more pronounced for $CaSn_{0.95}Sc_{0.05}O_{3-\delta}$ due to a higher Schottky barrier height.

TG-DSC was used to evaluate the hydration thermodynamics of $CaSn_{1-x}Sc_xO_{3-\delta}$ and $CaZr_{1-x}Sc_xO_{3-\delta}$ where x varied from 0.05 to 0.2. The experiments indicated an increasingly negative hydration enthalpy and entropy with increasing levels of Sc substitution for both materials. The parameters were in agreement with the values from literature and the ones calculated using conductivity measurements and TG. The values were also demonstrated to be consistent with respect to temperature (500-900 °C) and p_{H_2O} (0.1-1 atm). It can therefore be concluded that TG-DSC is a valuable technique for determining hydration thermodynamics.

The hydration enthalpies determined by TG-DSC exhibited a correlation to the basicity of the oxide, while the hydration entropies were suggested to be correlated to the vibrational wavenumber of the OH stretching mode (ν_{OH}). As basicity and ν_{OH} are additionally interrelated properties, it suggests a correlation between the enthalpy and entropy of hydration, as was demonstrated for both materials studied.

8. References

[1] EIA, *International Energy Outlook 2010*, United States Department of Energy, 2010, U.S. Government Printing Office: Washington D. C.

[2] Stambouli, A.B. and E. Traversa, *Solid oxide fuel cells (SOFCs): a review of an environmentally clean and efficient source of energy.* Renewable and Sustainable Energy Reviews, 2002. **6**(5): p. 433-455.

[3] Hoffert, M.I., *Farewell to Fossil Fuels?* Science, 2010. **329**(5997): p. 1292-1294.

[4] REN21, *Renewables 2007 - Global status report*, 2008.

[5] Iwahara, H., H. Uchida, and S. Tanaka, *High temperature type proton conductor based on $SrCeO_3$ and its application to solid electrolyte fuel cells.* Solid State Ionics, 1983. **9-10**(Part 2): p. 1021-1025.

[6] Norby, T., M. Widerøe, R. Glöckner, and Y. Larring, *Hydrogen in oxides.* Dalton Transactions, 2004(19): p. 3012-3018.

[7] Kjølseth, C., L.-Y. Wang, R. Haugsrud, and T. Norby, *Determination of the enthalpy of hydration of oxygen vacancies in Y-doped $BaZrO_3$ and $BaCeO_3$ by TG-DSC.* Solid State Ionics, 2010. **181**(39-40): p. 1740-1745.

[8] Ricote, S., N. Bonanos, H.J. Wang, and R. Haugsrud, *Conductivity, transport number measurements and hydration thermodynamics of $BaCe_{0.2}Zr_{0.7}Y_{(0.1-x)}Ni_xO_{3-d}$.* Solid State Ionics, 2011. **185**(1): p. 11-17.

[9] Fjeld, H., R. Haugsrud, A.E. Gunnæs, and T. Norby, *Proton and oxide ion conductivity in grain boundaries and grain interior of Ca-doped $Er_2Ti_2O_7$ with Si-impurities.* Solid State Ionics, 2008. **179**(33-34): p. 1849-1853.

[10] Fjeld, H., *Ionic transport in atomic and nanodimensional structures in oxides*, 2010, University of Oslo.

[11] Kofstad, P. and T. Norby, *Defects and transport in crystalline solids - Compendium for the advanced level course: Defect Chemistry and Reactions KJM5120*, 2010: University of Oslo.

[12] Norby, T., *Electrical Measurements. Compendium for the advanced level course: Experimental methods KJM-MENA4010 Module 2*, 2009: University of Oslo.

[13] Guo, X. and R. Waser, *Electrical properties of the grain boundaries of oxygen ion conductors: Acceptor-doped zirconia and ceria.* Progress in Materials Science, 2006. **51**(2): p. 151-210.

[14] Kröger, F.A. and H.J. Vink, *Relations between concentrations of imperfections in crystalline solids.* Solid State Physics, 1956. **3**: p. 307.

[15] Varela, J.A., J.A. Cerri, E.R. Leite, E. Longo, M. Shamsuzzoha, and R.C. Bradt, *Microstructural evolution during sintering of CoO doped SnO_2 ceramics.* Ceramics International, 1999. **25**(3): p. 253-256.

[16] Park, W.-J., W. Jo, D.-Y. Kim, and J.-H. Lee, *Enhanced densification of pure SnO_2 by spark plasma sintering.* Journal of Materials Science, 2005. **40**(14): p. 3825-3827.

[17] Liu, J. and W. Ning, *Influence of ZnO addition on the sintering properties of SnO_2 electrodes.* Journal of Materials Science, 2009. **44**(10): p. 2520-2524.

[18] Margionte, M.A.L., A.Z. Simões, C.S. Riccardi, F.M. Filho, A. Ries, L. Perazolli, and J.A. Varela, *WO_3 and ZnO-doped SnO_2 ceramics as insulating material.* Ceramics International, 2006. **32**(6): p. 713-718.

[19] Magrasó, A., R. Haugsrud, M. Segarra, and T. Norby, *Defects and transport in Gd-doped $BaPrO_3$.* Journal of Electroceramics, 2009. **23**(1): p. 80-88.

[20] Haile, S.M., G. Staneff, and K.H. Ryu, *Non-stoichiometry, grain boundary transport and chemical stability of proton conducting perovskites.* Journal of Materials Science, 2001. **36**(5): p. 1149-1160.

[21] Haile, S.M., D.L. West, and J. Campbell, *The role of microstructure and processing on the proton conducting properties of gadolinium-doped barium cerate.* Journal of Materials Research, 1998. **13**(6): p. 1576-1595.

[22] Kim, S. and J. Maier, *On the Conductivity Mechanism of Nanocrystalline Ceria.* Journal of The Electrochemical Society, 2002. **149**(10): p. J73-J83.

[23] Guo, X., W. Sigle, J. Fleig, and J. Maier, *Role of space charge in the grain boundary blocking effect in doped zirconia.* Solid State Ionics, 2002. **154-155**: p. 555-561.

[24] Guo, X., W. Sigle, and J. Maier, *Blocking Grain Boundaries in Yttria-Doped and Undoped Ceria Ceramics of High Purity.* Journal of the American Ceramic Society, 2003. **86**(1): p. 77-87.

[25] Fjeld, H., D.M. Kepaptsoglou, R. Haugsrud, and T. Norby, *Charge carriers in grain boundaries of 0.5% Sr-doped $LaNbO_4$.* Solid State Ionics, 2010. **181**(3-4): p. 104-109.

[26] Kjølseth, C., H. Fjeld, Ø. Prytz, P.I. Dahl, C. Estournès, R. Haugsrud, and T. Norby, *Space-charge theory applied to the grain boundary impedance of proton conducting $BaZr_{0.9}Y_{0.1}O_{3-d}$.* Solid State Ionics, 2010. **181**(5-7): p. 268-275.

[27] Iguchi, F., N. Sata, and H. Yugami, *Proton transport properties at the grain boundary of barium zirconate based proton conductors for intermediate temperature operating SOFC.* Journal of Materials Chemistry, 2010. **20**(30): p. 6265-6270.

[28] Glazer, A., *The classification of tilted octahedra in perovskites.* Acta Crystallographica Section B, 1972. **28**(11): p. 3384-3392.

[29] Mitchell, R.H., *Perovskites: modern and ancient*2002, Thunder Bay, Ont.: Almaz Press. VII, 318 s.

[30] Zhang, W., J. Tang, and J. Ye, *Structural, photocatalytic, and photophysical properties of perovskite $MSnO_3$ (M = Ca, Sr, and Ba) photocatalysts.* Journal of Materials Research, 2007. **22**(7): p. 1859-1871.

[31] Singh, M.K., J.W. Hong, N.K. Karan, H.M. Jang, R.S. Katiyar, S.A.T. Redfern, and J.F. Scott, *New cryogenic phase transitions in $SrSnO_3$.* Journal of Physics: Condensed Matter, 2010. **22**(9): p. 095901.

[32] Tateno, S., K. Hirose, N. Sata, and Y. Ohishi, *Structural distortion of $CaSnO_3$ perovskite under pressure and the quenchable post-perovskite phase as a low-pressure analogue to $MgSiO_3$.* Physics of the Earth and Planetary Interiors, 2010. **181**(1-2): p. 54-59.

[33] Shannon, R.D., *Revised effective ionic radii and systematic studies of interatomic distances in halides and chalcogenides.* Acta Crystallographica Section A, 1976. **32**(5): p. 751-767.

[34] Bévillon, É., A. Chesnaud, Y. Wang, G. Dezenneau, and G. Geneste, *Theoretical and experimental study of the structural, dynamical and dielectric properties of perovskite $BaSnO_3$.* Journal of Physics: Condensed Matter, 2008. **20**(14): p. 145217.

[35] Hadjarab, B., A. Bouguelia, and M. Trari, *Optical and transport properties of lanthanum-doped stannate $BaSnO_3$.* Journal of Physics D: Applied Physics, 2007. **40**(19): p. 5833.

[36] Köferstein, R. and F. Yakuphanoglu, *Semiconducting properties of Ge-doped $BaSnO_3$ ceramic.* Journal of Alloys and Compounds, 2010. **506**(2): p. 678-682.

[37] Kumar, A., R.N.P. Choudhary, B.P. Singh, and A.K. Thakur, *Effect of strontium concentration on electrical conduction properties of Sr-modified $BaSnO_3$.* Ceramics International, 2006. **32**(1): p. 73-83.

[38] Azad, A.M., L.L. Shyan, and M.A. Alim, *Immittance response of $CaSnO_3$ prepared by self-heat-sustained reaction.* Journal of Materials Science, 1999. **34**(6): p. 1175-1187.

[39] Parkash, O., D. Kumar, K.K. Srivastav, and R.K. Dwivedi, *Electrical conduction behaviour of cobalt substituted $BaSnO_3$.* Journal of Materials Science, 2001. **36**(24): p. 5805-5810.

[40] Wang, Y., *Synthesis and characterisation of acceptor-doped $BaSnO_3$ compounds as proton conductors. PhD Thesis.*, 2009, Ecole Centrale Paris.

[41] Hou, Z.F., *Ab initio calculations of elastic modulus and electronic structures of cubic $CaZrO_3$.* Physica B: Condensed Matter, 2008. **403**(17): p. 2624-2628.

[42] Ross, N.L. and T.D. Chaplin, *Compressibility of $CaZrO_3$ perovskite: Comparison with Ca-oxide perovskites.* Journal of Solid State Chemistry, 2003. **172**(1): p. 123-126.

[43] Islam, M.S., R.A. Davies, and J.D. Gale, *Hop, skip or jump? Proton transport in the $CaZrO_3$ perovskite oxide.* Chemical Communications, 2001(7): p. 661-662.

[44] Smith, J.B., *Protonledningsevne i indium- og ytterbiumdopede jordalkaliezirkonater. MSc. Thesis*, 1998, University of Oslo.

[45] Bao, J., H. Ohno, N. Kurita, Y. Okuyama, and N. Fukatsu, *Proton conduction in Al-doped $CaZrO_3$.* Electrochimica Acta, 2010. **56**(3): p. 1062-1068.

[46] Kurita, N., N. Fukatsu, K. Ito, and T. Ohashi, *Protonic Conduction Domain of Indium-Doped Calcium Zirconate.* Journal of The Electrochemical Society, 1995. **142**(5): p. 1552-1559.

[47] Kurita, N., Y.-P. Xiong, Y. Imai, and N. Fukatsu, *Measurements of the electronic conductivities of In-doped $CaZrO_3$ by a DC polarization technique.* Ionics. **16**(9): p. 787-795.

[48] Yajima, T., H. Kazeoka, T. Yogo, and H. Iwahara, *Proton conduction in sintered oxides based on $CaZrO_3$.* Solid State Ionics, 1991. **47**(3-4): p. 271-275.

[49] Bjørheim, T.S., A. Kuwabara, I. Ahmed, R. Haugsrud, S. Stølen, and T. Norby, *A combined conductivity and DFT study of protons in $PbZrO_3$ and alkaline earth zirconate perovskites.* Solid State Ionics, 2010. **181**(3-4): p. 130-137.

[50] Davies, R.A., M.S. Islam, and J.D. Gale, *Dopant and proton incorporation in perovskite-type zirconates.* Solid State Ionics, 1999. **126**(3-4): p. 323-335.

[51] Kreuer, K.D., S. Adams, W. Münch, A. Fuchs, U. Klock, and J. Maier, *Proton conducting alkaline earth zirconates and titanates for high drain electrochemical applications.* Solid State Ionics, 2001. **145**(1-4): p. 295-306.

[52] Kreuer, K.D., W. Münch, M. Ise, T. He, A. Fuchs, U. Traub, and J. Maier, *Defect interactions in proton conducting Perovskite-type oxides.* Berichte der Bunsen-Gesellschaft, 1997. **101**(9): p. 1344-1350.

[53] Glöckner, R., M.S. Islam, and T. Norby, *Protons and other defects in $BaCeO_3$: a computational study.* Solid State Ionics, 1999. **122**(1-4): p. 145-156.

[54] Islam, M.S., R.A. Davies, and J.D. Gale, *Proton Migration and Defect Interactions in the $CaZrO_3$ Orthorhombic Perovskite: A Quantum Mechanical Study.* Chemistry of Materials, 2001. **13**(6): p. 2049-2055.

[55] Islam, M.S., P.R. Slater, J.R. Tolchard, and T. Dinges, *Doping and defect association in $AZrO_3$ (A = Ca, Ba) and $LaMO_3$ (M = Sc, Ga) perovskite-type ionic conductors.* Dalton Transactions, 2004(19): p. 3061-3066.

[56] Davies, R.A., M.S. Islam, A.V. Chadwick, and G.E. Rush, *Cation dopant sites in the $CaZrO_3$ proton conductor: a combined EXAFS and computer simulation study.* Solid State Ionics, 2000. **130**(1-2): p. 115-122.

[57] Islam, M.S., R.A. Davies, C.A.J. Fisher, and A.V. Chadwick, *Defects and protons in the $CaZrO_3$ perovskite and $Ba_2In_2O_5$ brownmillerite: computer modelling and EXAFS studies.* Solid State Ionics, 2001. **145**(1-4): p. 333-338.

[58] Norby, T., *Proton Conduction in Solids: Bulk and Interfaces.* MRS Bulletin, 2009. **34**: p. 923-928.

[59] Norby, T., *Proton Conductivity in Perovskite Oxides in "Perovskite Oxide for Solid Oxide Fuel Cells"*, 2009. p. 217-241.

[60] Schober, T. and H.G. Bohn, *Water vapor solubility and electrochemical characterization of the high temperature proton conductor $BaZr_{0.9}Y_{0.1}O_{2.95}$.* Solid State Ionics, 2000. **127**(3-4): p. 351-360.

[61] Ricote, S., N. Bonanos, and G. Caboche, *Water vapour solubility and conductivity study of the proton conductor $BaCe_{(0.9 - x)}Zr_xY_{0.1}O_{(3 -d)}$.* Solid State Ionics, 2009. **180**(14-16): p. 990-997.

[62] Yamazaki, Y., P. Babilo, and S.M. Haile, *Defect Chemistry of Yttrium-Doped Barium Zirconate: A Thermodynamic Analysis of Water Uptake.* Chemistry of Materials, 2008. **20**(20): p. 6352-6357.

[63] Stokes, S.J. and M.S. Islam, *Defect chemistry and proton-dopant association in $BaZrO_3$ and $BaPrO_3$.* Journal of Materials Chemistry, 2010. **20**(30): p. 6258-6264.

[64] Furøy, K.A., R. Haugsrud, M. Hänsel, A. Magrasó, and T. Norby, *Role of protons in the electrical conductivity of acceptor-doped $BaPrO_3$, $BaTbO_3$, and $BaThO_3$.* Solid State Ionics, 2007. **178**(7-10): p. 461-467.

[65] Larring, Y. and T. Norby, *Protons in rare earth oxides.* Solid State Ionics, 1995. **77**: p. 147-151.

[66] Kreuer, K.D., *Proton-conducting oxides.* Annu. Rev. Mater. Res., 2003. **33**: p. 333-359.

[67] Kreuer, K.D., *On the development of proton conducting materials for technological applications.* Solid State Ionics, 1997. **97**(1-4): p. 1-15.

[68] Omata, T., Y. Noguchi, and S. Otsuka-Yao-Matsuo, *Infrared study of high temperature proton conducting $Sr(Zr_{0.95}M_{0.05}III)O_{3-d}$; formation of $MIIIO_6$-cluster depends on dopant species.* Solid State Ionics, 2005. **176**(39-40): p. 2941-2944.

[69] Omata, T., M. Takagi, and S. Otsuka-Yao-Matsuo, *O-H stretching vibrations of proton conducting alkaline-earth zirconates.* Solid State Ionics, 2004. **168**(1-2): p. 99-109.

[70] Münch, W., K.D. Kreuer, S. Adams, G. Seifert, and J. Maier, *The Relation between Crystal Structure and the Formation and Mobility of Protonic Charge Carriers in Perovskite-type Oxides: A Case Study of Y-doped $BaCeO_3$ and $SrCeO_3$* Phase Transitions, 1999. **68**: p. 567–586.

[71] Krug, F., T. Schober, and T. Springer, *In situ measurements of the water uptake in Yb doped $SrCeO_3$.* Solid State Ionics, 1995. **81**(1-2): p. 111-118.

[72] Krug, F. and T. Schober, *The High-Temperature Proton Conductor Strontium Zirconate: Thermogravimetry of Water Uptake.* Journal of the American Ceramic Society, 1997. **80**(3): p. 794-796.

[73] Iguchi, F., N. Sata, T. Tsurui, and H. Yugami, *Microstructures and grain boundary conductivity of $BaZr_{1-x}Y_xO_3$ (x = 0.05, 0.10, 0.15) ceramics.* Solid State Ionics, 2007. **178**(7-10): p. 691-695.

[74] Park, H.J., C. Kwak, K.H. Lee, S.M. Lee, and E.S. Lee, *Interfacial protonic conduction in ceramics.* Journal of the European Ceramic Society, 2009. **29**(12): p. 2429-2437.

[75] Baik, H.D., *Proton conduction in Y_2O_3-doped $SrZrO_3$.* Journal of the Korean Ceramic Society, 2002. **39**: p. 635.

[76] Potter, A.R. and R.T. Baker, *Impedance studies on Pt|$SrCe_{0.95}Yb_{0.05}O_3$|Pt under dried and humidified air, argon and hydrogen.* Solid State Ionics, 2006. **177**(19-25): p. 1917-1924.

[77] Ryu, K.H. and S.M. Haile, *Chemical stability and proton conductivity of doped $BaCeO_3$-$BaZrO_3$ solid solutions.* Solid State Ionics, 1999. **125**(1-4): p. 355-367.

[78] Cervera, R.B., Y. Oyama, S. Miyoshi, K. Kobayashi, T. Yagi, and S. Yamaguchi, *Structural study and proton transport of bulk nanograined Y-doped $BaZrO_3$ oxide protonics materials.* Solid State Ionics, 2008. **179**(7-8): p. 236-242.

[79] Groß, B., C. Beck, F. Meyer, T. Krajewski, R. Hempelmann, and H. Altgeld, *$BaZr_{0.85}Me_{0.15}O_{2.925}$ (Me=Y, In and Ga): crystal growth, high-resolution transmission electron microscopy, high-temperature X-ray diffraction and neutron scattering experiments.* Solid State Ionics, 2001. **145**(1-4): p. 325-331.

[80] Avila-Paredes, H.J., K. Choi, C.-T. Chen, and S. Kim, *Dopant-concentration dependence of grain-boundary conductivity in ceria: A space-charge analysis.* Journal of Materials Chemistry, 2009. **19**(27): p. 4837-4842.

[81] Babilo, P., T. Uda, and S.M. Haile, *Processing of yttrium-doped barium zirconate for high proton conductivity.* Journal of Materials Research, 2007. **22**(5): p. 1322-1330.

[82] Sánchez-Bautista, C., A.J. Dos santos-García, J. Peña-Martínez, and J. Canales-Vázquez, *The grain boundary effect on dysprosium doped ceria.* Solid State Ionics. **181**(37-38): p. 1665-1673.

[83] Babilo, P. and S.M. Haile, *Enhanced Sintering of Yttrium-Doped Barium Zirconate by Addition of ZnO.* Journal of the American Ceramic Society, 2005. **88**(9): p. 2362-2368.

[84] Park, J.-S., J.-H. Lee, H.-W. Lee, and B.-K. Kim, *Low temperature sintering of $BaZrO_3$-based proton conductors for intermediate temperature solid oxide fuel cells.* Solid State Ionics, 2010. **181**(3-4): p. 163-167.

[85] Wang, H., R. Peng, X. Wu, J. Hu, and C. Xia, *Sintering Behavior and Conductivity Study of Yttrium-Doped $BaCeO_3$–$BaZrO_3$ Solid Solutions Using ZnO Additives.* Journal of the American Ceramic Society, 2009. **92**(11): p. 2623-2629.

[86] Maître, A., D. Beyssen, and R. Podor, *Effect of ZrO_2 additions on sintering of SnO_2-based ceramics.* Journal of the European Ceramic Society, 2004. **24**(10-11): p. 3111-3118.

[87] Aguilar-Martínez, J.A., M.B. Hernández, A.B. Glot, and M.I. Pech-Canul, *Microstructure and electrical properties in SnO_2 ceramics with sequential addition of Co, Sb and Ca.* Journal of Physics D: Applied Physics, 2007. **40**(22): p. 7097.

[88] Azad, A.-M., L.L.W. Shyan, and P.T. Yen, *Synthesis, processing and microstructural characterization of $CaSnO_3$ and $SrSnO_3$ ceramics.* Journal of Alloys and Compounds, 1999. **282**(1-2): p. 109-124.

[89] Bjørheim, T.S., *DFT-modellering og transportstudier av protoner i blybaserte perovskitter, MSc Thesis*, 2008, University of Oslo.

[90] NorECs. *Probostat™*. 2011 [cited 2011 February]; Available from: http://www.norecs.com/index.php?page=141.

[91] Norby, T. and P. Kofstad, *Electrical Conductivity and Defect Structure of Y_2O_3 as a Function of Water Vapor Pressure.* Journal of the American Ceramic Society, 1984. **67**(12): p. 786-792.

[92] Novocontrol, *Alpha-A Dielectric, Conductivity, Impedance and Gain Phase Modular Measurement System - Technical Specification Alpha-A Mainframe ZGS, ZG4 and ZG2 Test Interfaces*, 2010.

[93] Holt, A. and P. Kofstad, *Electrical conductivity and defect structure of Mg-doped Cr_2O_3.* Solid State Ionics, 1997. **100**(3-4): p. 201-209.

[94] Kjølseth, C., *Thermodynamics and transport of protons in functional oxides. PhD Thesis.*, 2009, University of Oslo.

[95] Kaiserberger, *Netzsch Water Vapour Furnace and Humidity Generators - Manual*, 2008.

[96] NetZsch-GmbH, *Calibration Kit: 6.223.5-91.2.*

[97] Netzsch, *derived from measurements carried out by Netszch with a DSC 200 previously calibrated for temperature with Hg, In, Bi, Zn and CsCl.*

[98] Gray, A.P., Proceedings of the Fourth ICTA, 1974. **3**: p. 991.

[99] Widmann, G. and R. Riesen, *Thermoanalyse*, 1984, Hüthig Verlag.

[100] Eysel, W. and K.-H. Breuer, Thermochemica Acta, 1982. **52**: p. 317.

[101] Netzsch, *Proteus - Thermal Analysis **V 4.8.5***. 2008.

[102] Tyholdt, F., *Elektrisk ledningsevne og defektstruktur i Sr-substituert $LaPO_4$, MSc. Thesis*, 1999, University of Oslo.

[103] Boukamp, B.A., Equivalent Circuit for Windows, University of Twente, 2003.

[104] Fleig, J. and J. Maier, *Finite-Element Calculations on the Impedance of Electroceramics with Highly Resistive Grain Boundaries: I, Laterally Inhomogeneous Grain Boundaries.* Journal of the American Ceramic Society, 1999. **82**(12): p. 3485-3493.

[105] Bohn, H.G. and T. Schober, *Electrical conductivity of the high-temperature proton conductor $BaZr_{0.9}Y_{0.1}O_{2.95}$.* Journal of the American Ceramic Society, 2000. **83**(4): p. 768-772.

[106] Kreuer, K.D., *Aspects of the formation and mobility of protonic charge carriers and the stability of perovskite-type oxides.* Solid State Ionics, 1999. **125**: p. 285-302.

[107] Huheey, J.E., *Inorganic chemistry: principles of structure and reactivity*, 1983, Harper & Row: New York.

[108] Allred, A.L., *Electronegativity values from thermochemical data.* Journal of Inorganic and Nuclear Chemistry, 1961. **17**(3-4): p. 215-221.

[109] Goldschmidt, V.M., T. Barth, G. Lunde, and W. Zachariasen, *Geochemical distribution law of the elements. VII. Summary of the chemistry of crystals.* Skrifter Norske Videnskaps-Akad. Oslo, Mat.-Naturvit. Kl., 1926. **No. 2**: p. 117.

[110] Teraoka, Y., M.-D. Wei, and S. Kagawa, *Double perovskites containing hexavalent molybdenum and tungsten: synthesis, structural investigation and proposal of a fitness factor to discriminate the crystal symmetry.* Journal of Materials Chemistry, 1998. **8**(11): p. 2323-2325.

[111] Stølen, S., T. Grande, and N.L. Allan, *Chemical thermodynamics of materials: macroscopic and microscopic aspects*2004, Chichester: Wiley. XII, 395 s.

[112] Hempelmann, R., J. Eschenbaum, M. Altmayer, B. Groß, D. Grambole, F. Herrmann, D. Nagengast, J. Krauser, and A. Weidinger, *Pressure/composition isotherms of proton conducting $SrYb_{0.05}Zr_{0.95}O_{2.975}/H_2O$ by means of nuclear resonance reaction analysis.* Berichte der Bunsengesellschaft für physikalische Chemie, 1997. **101**(7): p. 985-993.

9. Appendix

9.1. Defect model

This appendix outlines the defect equilibria used in order to model the mass uptake from TG and p_{H_2O} dependencies of bulk and grain boundary conductivities of CSSc5 and CSZn1. For both samples, the following electroneutrality condition is assumed:

$$\left[\mathrm{Acc}'\right] = 2[\mathrm{v}_\mathrm{O}^{\bullet\bullet}] + [\mathrm{OH}_\mathrm{O}^{\bullet}] \qquad \textbf{Equation 9.1}$$

together with site restriction for perovskites:

$$\left[\mathrm{O}_\mathrm{O}^{\mathrm{X}}\right] + [\mathrm{v}_\mathrm{O}^{\bullet\bullet}] + [\mathrm{OH}_\mathrm{O}^{\bullet}] = 3 \qquad \textbf{Equation 9.2}$$

Using these expressions as well as the equilibrium constant expression for hydration (Equation 2.13), K_{hydr}, the proton concentration can be evaluated to give the following expression:

$$[\mathrm{OH}_\mathrm{O}^{\bullet}] = \frac{-3\mathrm{K}' \pm \sqrt{9\mathrm{K}'^2 - 4\mathrm{K}'^2[\mathrm{Acc}']^2 + 24\mathrm{K}'[\mathrm{Acc}'] + \mathrm{K}'^2[\mathrm{Acc}']^2 - 2\mathrm{K}'^2[\mathrm{Acc}']}}{4 - \mathrm{K}'} \qquad \textbf{Equation 9.3}$$

where $\mathrm{K}' = \mathrm{K}_{\mathrm{hydr}} p_{\mathrm{H_2O}}$. The concentration of oxygen vacancies are then evaluated by combination of Equation 9.1 and Equation 9.3.

For the conductivity modelling, the partial conductivity of each charge carrier *i* is given by:

$$\sigma_\mathrm{i} = \mathrm{z_i e c_i u_i} \qquad \textbf{Equation 9.4}$$

where the c_i is the concentration of charge carriers given in cm^{-3}. However, the concentration of charge carriers is often given in molar fraction, and as such the specific conductivity of both samples is given by:

$$\sigma_\mathrm{i} = \mathrm{z_i e c_i u_i F \rho_m} \qquad \textbf{Equation 9.5}$$

where F and ρ_m are the Faraday constant and molar density of both samples, respectively. The mobility of a charge carrier can be expressed through an activated jump mechanism:

$$u_i = \frac{u_{0,i}}{T} \exp\left(-\frac{\Delta H_{mob,i}}{RT}\right) \qquad \textbf{Equation 9.6}$$

For all conductivity models, only oxygen vacancies and protons are considered to contribute to the total electrical conductivity yielding the following expression:

$$\sigma_{tot} = \sigma_{v_O^{\bullet\bullet}} + \sigma_{OH_O^{\bullet}} \qquad \textbf{Equation 9.7}$$

With the given expressions, there are six and two unknown parameters for the conductivity and TG models, respectively. Furthermore, $[Acc^{/}]$ was kept constant for each fitting procedure.